

3-26-2015

Biaxial Anisotropic Material Development and Characterization using Rectangular to Square Waveguide

Alexander G. Knisely

Follow this and additional works at: <https://scholar.afit.edu/etd>

Recommended Citation

Knisely, Alexander G., "Biaxial Anisotropic Material Development and Characterization using Rectangular to Square Waveguide" (2015). *Theses and Dissertations*. 40.
<https://scholar.afit.edu/etd/40>

This Thesis is brought to you for free and open access by the Student Graduate Works at AFIT Scholar. It has been accepted for inclusion in Theses and Dissertations by an authorized administrator of AFIT Scholar. For more information, please contact AFIT.ENWL.Repository@us.af.mil.



**BIAXIAL ANISOTROPIC
MATERIAL DEVELOPMENT AND
CHARACTERIZATION USING
RECTANGULAR TO SQUARE WAVEGUIDE**

THESIS

Alexander G. Knisely
AFIT-ENG-MS-15-M-055

**DEPARTMENT OF THE AIR FORCE
AIR UNIVERSITY**

AIR FORCE INSTITUTE OF TECHNOLOGY

Wright-Patterson Air Force Base, Ohio

DISTRIBUTION STATEMENT A
APPROVED FOR PUBLIC RELEASE; DISTRIBUTION UNLIMITED.

The views expressed in this document are those of the author and do not reflect the official policy or position of the United States Air Force, the United States Department of Defense or the United States Government. This material is declared a work of the U.S. Government and is not subject to copyright protection in the United States.

AFIT-ENG-MS-15-M-055

BIAXIAL ANISOTROPIC
MATERIAL DEVELOPMENT AND CHARACTERIZATION USING
RECTANGULAR TO SQUARE WAVEGUIDE

THESIS

Presented to the Faculty
Department of Electrical and Computer Engineering
Graduate School of Engineering and Management
Air Force Institute of Technology
Air University
Air Education and Training Command
in Partial Fulfillment of the Requirements for the
Degree of Master of Science in Electrical Engineering

Alexander G. Knisely, B.S.E.E.

March 2015

DISTRIBUTION STATEMENT A
APPROVED FOR PUBLIC RELEASE; DISTRIBUTION UNLIMITED.

BIAXIAL ANISOTROPIC
MATERIAL DEVELOPMENT AND CHARACTERIZATION USING
RECTANGULAR TO SQUARE WAVEGUIDE
THESIS

Alexander G. Knisely, B.S.E.E.

Committee Membership:

Dr. Michael J. Havrilla
Chair

Dr. Peter J. Collins
Member

Maj Milo W. Hyde, PhD
Member

Abstract

The advent of 3-D printing provides a new way to develop complex electromagnetic media. Complex media poses measurement challenges and require new techniques to characterize sample constitutive parameters. A biaxial anisotropic sample is designed using crystallographic symmetry and tensor elements are predicted using equivalent capacitive and inductive lumped elements. Samples are measured using the Waveguide Rectangular to Waveguide Square (WRWS) cubic sample measurement system. The WRWS system supports the analysis of a cubic biaxial anisotropic sample by measuring the sample in different measurement orientations. The orientation S-parameter data is used to extract tensor element permittivities and permeabilities using an analytic, closed-form technique. Research performed in this document demonstrates a sample synthesis methodology, a measurement representative computational electromagnetic (CEM) prediction of WRWS sample measurements and tests results of an electrically biaxial sample. An uncertainty analysis is also conducted on the experimental data to evaluate potential error sources. The lumped element and CEM predictions agree with the test results. Supplemental discussion also provides a comparison between test data and a free-space simulated results as well as simulated example of an electrically biaxial sample loaded with alumina. These two examples demonstrate the utility of a crystallographic sample design.

To my family.

Acknowledgements

I would like to thank Dr. Michael J. Havrilla, Dr. Peter J. Collins and Dr. Milo W. Hyde IV. Each of you provided the physical insight, mathematical rigor and uniqueness, which I utilized in this work and will continue to practice in my future endeavors. Also, special thanks to Dr. Jeffery W. Allen for providing test samples, and Dr. Andrew E. Bogle for providing another perspective.

Alexander G. Knisely

Table of Contents

	Page
Abstract	iv
Acknowledgements	vi
List of Figures	ix
List of Tables	xiii
I. Introduction	1
1.1 Problem Statement	1
1.2 Scope and Research Goals	1
1.3 Limitations and Challenges	3
1.4 Resource Requirements	4
1.5 Thesis Organization	4
II. Background	6
2.1 Overview of Material Measurement Techniques	6
2.2 Anisotropic Materials	11
2.3 Biaxial Anisotropic Material Selection and Research Usage	12
2.4 TEM waves at an Oblique Incidence on a Biaxial Anisotropic Slab	13
Field Analysis	14
Evaluation of the Parallel Polarization	20
Evaluation of the Perpendicular Polarization	23
2.5 Demonstration of Biaxial Anisotropic Slab Performance	25
2.6 Summary	28
III. Measurement Methodology	29
3.1 Waveguide Rectangular to Waveguide Square Development	29
3.2 Evaluation of Rectangular Waveguide and WRWS	34
3.3 Inverse Problem: Biaxial Parameter Extraction	37
3.4 Summary	43
IV. Sample Development	46
4.1 Biaxial Sample Development	46
4.2 Lumped Element Prediction of Biaxial Anisotropic Constitutive Parameters	50
Sample Analysis Methodology	51

	Page
Sample Synthesis Methodology	54
4.3 Computational Electromagnetic Prediction of Biaxial Anisotropic Constitutive Parameters	56
Simulation calibration and sample measurement	59
TRL Calibration Material Parameter Extraction	64
4.4 Summary	65
V. Results	66
5.1 The WRWS system	66
5.2 Calibration and Measurement	67
5.3 CST Model WRWS Model Simulation	70
5.4 Measurement Uncertainty Analysis	75
5.5 Observations and Discussion	82
5.6 Electrically Biaxial Anisotropic Samples using different materials	83
5.7 Summary	84
VI. Conclusion	85
6.1 Future Work	85
Bibliography	87

List of Figures

Figure	Page
1. Drawing of Waveguide Rectangular to Waveguide Square (WRWS) System	2
2. Rectangular Waveguide Anisotropic Sample Measurement	9
3. Evolution of WRWS system	10
4. Demonstrating Collin's Sample Design is Biaxial Anisotropic	12
5. 2-D Biaxial Slab problem	13
6. Left: 3-D MATLAB® Plot of Electric Field Response from a Biaxial Anisotropic Slab with constitutive tensors (2.71). Right Top: Transmitted Elliptical Polarization, Right Bottom: Reflected Elliptical Polarization.	26
7. Top: Biaxial Slab with constitutive tensors (2.71) with Normal Incidence Electric Field at Slant polarization. Left: Parallel polarization only, Right Perpendicular polarization only.	27
8. TE_{10} modes propagating in a Rectangular Waveguide and WRWS Transition guide	34
9. Comparison of Magnitude S-parameter Data: Top-Transmission, Bottom-Reflection	35
10. Comparison of Modes Propagated versus Frequency: Top: Rectangular Waveguide, Bottom: Square Waveguide	36
11. Waveguide arrangement	36
12. Sample filled section of waveguide	38
13. Unit Cell Cubic Sample	40
14. Closed form measurement with sample resonances at $\frac{n\lambda}{2}$	42

Figure	Page
15. Comparison of RWG and WRWS with Free-space filled sample holder: Left: S_{11} , Right: S_{21}	43
16. Isotropic UV cured RWG (Top) and WRWS (Bottom) polymer samples and sample holders	44
17. Isotropic UV cured RWG and WRWS polymer sample comparison	45
18. Demonstrates Curies Principle and show the symmetry that exists in each structure.	47
19. Equivalent Lumped Element Prediction Technique: Left: Permittivity, Right: Permeability	51
20. Sample and Sample Holder	55
21. CST models of Rectangular Waveguide and WRWS system (Left), Teflon Samples installed (Right)	57
22. CST WRWS Teflon Sample De-embedded	58
23. Graphical Depiction of TRL calibration	60
24. Sample Holder with dimensions	63
25. Rectangular Waveguide Teflon Sample TRL Calibrated Solution	64
26. WRWS setup and view of square aperture	66
27. WRWS Cubic Sample Holder and Line Standard	67
28. WRWS showing waveguide transition on either side of the sample holder, line standard is placed left of sample holder	68
29. Measurement Setup with Test port cables and Network Analyzer	69
30. Sample installed in Sample Holder Orientation 1 (Left), Partially installed in Orientation 2 (Right)	70
31. CST Model of WRWS with a green cube denoting sample region	71

Figure	Page
32. CST WRWS Model in mesh view	72
33. Measured Permittivity from Electrically Biaxial Anisotropic Cube with Air Occlusions arranged in a 9 by 6 array	74
34. CST Simulated Permittivity from Electrically Biaxial Anisotropic Cube with Air Occlusions arranged in a 9 by 6 array	74
35. Monte Carlo Uncertainty Analysis Flow Chart: Gold indicates random test variables, Green- Test Data Inputs, Orange- Outputs, Blue- Code. Bi-directional arrows associated with the calibration code indicate a specific uncertainty is obtained given a particular transmission or reflection coefficient.	75
36. VNA Uncertainty vs Reflection (Top) and Transmission (Bottom) generated for the Agilent Technologies® E8362B VNA from the Keysight Technologies® VNA uncertainty calculator.	76
37. Cubic sample (blue) with colored gaps regions. The colored regions show how gaps are accounted in the Monte Carlo Simulation	77
38. Error Bars Generated from 1000 trial Monte Carlo on Experimental Data, Odd orientations (Top), Even orientations (Bottom)	79
39. Comparison of Simulation Data with Experimental Uncertainty Data Odd orientations (Top), Even orientations (Bottom)	80
40. Comparison of Vertical arrangement Lumped Element Data and Simulation Data with Experimental Uncertainty Data Odd orientations (Top), Even orientations (Bottom)	81
41. Overlay of sample measurement orientations with TE_{10} mode profile showing potential non-uniform interrogation of sample	82
42. TEM Free Space CST Measure of an infinite array of cubes arranged in a slab	83

Figure	Page
43. Plane Wave Excitation Model on an infinite array of cubes	84
44. Electrically Biaxial Alumina Inclusion Loaded Sample simulated in CST Microwave Studio	84

List of Tables

Table	Page
1. Vertical Lumped Element Prediction	56
2. Horizontal Lumped Element Prediction	56
3. CST Simulation Performance Figures	73

BIAXIAL ANISOTROPIC
MATERIAL DEVELOPMENT AND CHARACTERIZATION USING
RECTANGULAR TO SQUARE WAVEGUIDE

I. Introduction

1.1 Problem Statement

Advances in 3 dimensional (3-D) printing offer a new and unique microwave material development capability. Sub-wavelength features can be easily printed and implemented into microwave system designs. These sub-wavelength features can support a wide variety of material performance characteristics. New electromagnetic material performance characteristics pose challenges, such as: how to correctly measure a material and how to design a material with specific performance characteristics? The complexity of these challenges vary in difficulty depending on the measurement technique used and the material's constitutive parameters.

1.2 Scope and Research Goals

Electromagnetic materials can include characteristics ranging in Linearity, Homogeneity, Isotropy and Reciprocity. Evaluating materials based on isotropy versus measurement complexity, isotropic materials are the simplest to evaluate followed by bi-isotropic, anisotropic and bi-anisotropic. Each category requires additional unique measurements to successfully evaluate the constitutive material parameters. Unique measurement information come from measurement system degrees of freedom including: evaluating the sample in different orientations, or interrogating the sample with

different field polarizations.

A new waveguide material measurement system is developed in this research effort to evaluate a single sample about different orientations. The waveguide method is selected because a Thru-Reflect-Line (TRL) calibration can be utilized and measurements can be made at the fundamental TE_{10} mode, which supports closed form solutions to obtain material permittivity and permeability constitutive parameters. The Waveguide Rectangular to Waveguide Square (WRWS) system in Figure 1 has waveguide transitions from the X-band (8.2-12.4 GHz) rectangular waveguide profile ($0.9'' \times 0.4''$) to a square profile ($0.9'' \times 0.9''$). This square profile is aligned to the cubic sample holder which allows for cubic samples to be measured and indexed about its six sides and provides measurement diversity in the sample's different orientations. The WRWS system is employed to evaluate cubic biaxial anisotropic samples to exercise its anisotropic measurement capabilities, because biaxial anisotropic samples are the most measurement diverse case for the WRWS system, and demand the most measurements.

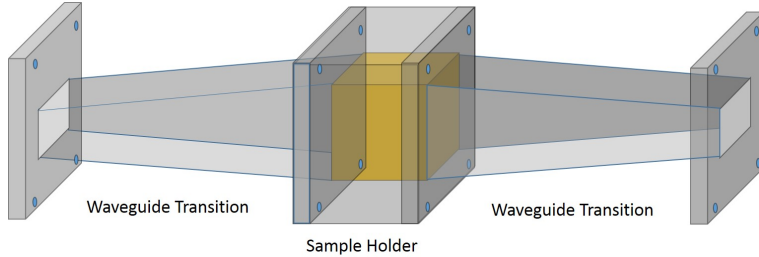


Figure 1. Drawing of Waveguide Rectangular to Waveguide Square (WRWS) System

Cubic biaxial anisotropic samples are designed using crystallographic symmetry, constituted using a computer aided design (CAD) program and fabricated on an additive UV cured polymer 3-D printer. Samples are then tested in the WRWS system and constitutive parameter data is extracted. Two prediction methods are devised to provide sample design and verification of constitutive parameter data. The

first method is a capacitive and inductive lumped element equivalent circuit design model, and the second method is a computation electromagnetic (CEM) solver model developed in CST Microwave Studio® .

The goal of this research is to demonstrate the WRWS system as a closed form method for measuring engineered biaxial anisotropic materials and demonstrate a crystallographic design methodology. Success is measured by comparing the experimentally extracted constitutive parameter data against the two prediction methods. Additionally, a TRL calibration technique is used to accommodate systematic errors and an uncertainty analysis is conducted to evaluate the effects of random error sources in the WRWS system.

1.3 Limitations and Challenges

Biaxial anisotropic measurement and material design are the focus of this research because it constrains measurement diversity in evaluating a sample about different orientations. Biaxial anisotropic materials consist of materials which have permittivity $\overset{\leftrightarrow}{\epsilon}$ and permeability $\overset{\leftrightarrow}{\mu}$ represented by

$$\overset{\leftrightarrow}{\epsilon} = \begin{bmatrix} \epsilon_{xx} & 0 & 0 \\ 0 & \epsilon_{yy} & 0 \\ 0 & 0 & \epsilon_{zz} \end{bmatrix}, \quad \overset{\leftrightarrow}{\mu} = \begin{bmatrix} \mu_{xx} & 0 & 0 \\ 0 & \mu_{yy} & 0 \\ 0 & 0 & \mu_{zz} \end{bmatrix}. \quad (1.1)$$

which posses tensor elements that are orthogonal and unique about the sample's x, y and z axes (assuming alignment along the optic axis).

The challenges in biaxial anisotropic research are in devising an accurate material characterization method and designing a material which exhibits biaxial anisotropic performance. Because the WRWS system accommodates a 0.9" edge length cubic sample, the sample is electrically thick at X-band which poses $\frac{\lambda}{2}$ resonance issues.

These resonances occur at frequencies in which the S_{11} measurement approaches zero, resulting in singularities in the closed form solutions for permittivity and permeability. A methodology for avoiding the resonance issue is to implement a root search method and assume particular permittivity or permeability values. Knowing a sample's relative permeability, and guessing a relative permittivity allows for a root search to be performed on the S_{21} data and yields resonance free permittivity results. The same root search process can be performed obtaining a sample's permeability, if the permittivity is known and a guess is made on a samples permeability. The root search process avoids using both sets of S-parameter data and yields valid resonance free results. Because dielectric materials are readily available and easier to manipulate than magnetic samples, electrically biaxial anisotropic samples having permeability μ_0 are only considered in this research. Other material designs are discussed in the future work section.

1.4 Resource Requirements

The Air Force Institute of Technology (AFIT) material measurements laboratory possesses Vector Network Analyzers, microwave measurement support tooling, the WRWS measurement system, and CST Microwave Studio® licenses to support the CEM analysis. Additionally, AFIT partnership with Air Force Research Laboratory (AFRL), Sensors Directorate, Electromagnetics Research Branch has yielded the ability to fabricate material samples using their ultraviolet (UV) cured ink-jet type 3-D polymer printer.

1.5 Thesis Organization

This document describes the research and development of the WRWS anisotropic material measurement capability and an electrically biaxial anisotropic material.

Chapter 2 provides background information on waveguide material measurement capabilities and shows how the evolution and performance trade-offs in waveguide material measurement techniques lead to the WRWS design. A theoretical model of a biaxial anisotropic slab is developed to demonstrate the unique performance characteristics of a biaxial anisotropic material and discuss how the material is evaluated in the WRWS system. Chapter 3 provides an analysis of a rectangular waveguide filled with biaxial anisotropic material. A closed-form Nicolson-Ross-Wier type formulation is also derived for the WRWS system. A comparison between the rectangular waveguide profile, and the square sample holder profile is also performed to demonstrate the operational modes, and to show the appropriate measurement frequencies. Chapter 4 addresses a crystallographic sample design, fabrication, constitutive parameter prediction techniques and the implementation of a TRL calibration. Chapter 5 demonstrates the experimental measurement capabilities, evaluating the sources of measurement errors in an uncertainty analysis and compares the measured data to the predicted data. Chapter 6 provides a conclusion, remarks and suggestions for future work.

II. Background

Research into waveguide material measurement theory and anisotropic sample design is conducted to understand the historical progression of anisotropic material measurement and development research. Waveguide material measurement techniques, crystallographic sample design and electromagnetic material development are studied and the gained knowledge is applied toward the development of the WRWS anisotropic measurement capability and biaxial anisotropic sample characterization. Additionally, a 2 dimensional (2-D) free-space analysis of an infinite biaxial slab is performed to understand the transmitted and reflected field effects from a slab of biaxial anisotropic material. The results of the 2-D analysis demonstrate potential applications for a biaxial anisotropic material and show how the constitutive parameters are extracted in particular measurement scenarios.

2.1 Overview of Material Measurement Techniques

Waveguide material measurement techniques became prevalent with the works of Nicolson, Ross and Weir, (NRW)[1],[2]. Their research demonstrate a fundamental approach to material characterization. Material characterization requires that a forward problem be developed, which describes the fields, boundary conditions and the media regions involved in the measurement system. This forward problem yields constraint equations, and identifies how the measurable quantities, namely, Transmission (T) and Reflection (Γ) coefficients, are related to permittivity and permeability. The reflection and transmission coefficients are measured directly as S-parameters using a Vector Network Analyzer, where T is equivalent to S_{21} and Γ is S_{11} . The forward

problem relationship can be described as

$$\left. \begin{array}{l} S_{11} = S_{11}(\epsilon, \mu) \\ S_{21} = S_{21}(\epsilon, \mu) \end{array} \right\} \text{Foward Problem.} \quad (2.1)$$

An inverse solution is then constructed where permittivity and permeability are solved in terms of S_{11} and S_{21} :

$$\left. \begin{array}{l} \epsilon = \epsilon(S_{11}, S_{21}) \\ \mu = \mu(S_{11}, S_{21}) \end{array} \right\} \text{Inverse Solution.} \quad (2.2)$$

This inverse solution is used to convert experimental data inputs such as material thickness, incident angle, polarization, S_{21} , and S_{11} into permittivity and permeability values.

The NRW methodology however, is not without its challenges. The chief NRW problem is sample thickness. Blankney [3] illustrated that sample thickness can support a standing wave when wavelengths are related to sample thickness by integer multiples of $d = \frac{\lambda}{2}$ (assuming the sample is low loss). These standing waves create resonances in a material sample, which distort extracted relative permittivity and permeability values. A solution to this problem is to keep samples thin, i.e.: $d < \frac{\lambda}{2}$.

An alternative solution allows thick samples to be measured, but requires a-priori knowledge about either the samples permittivity or permeability. Baker-Jarvis [4] demonstrated the extraction of a material's relative permittivity given its relative permeability. Material parameter extraction is performed using either Transmission or Reflection data. Using either the Transmission or Reflection data avoids the resonance issues that manifest when both the transmission and reflection data are required to extract the permittivity and permeability. The single data source extraction is performed using a 1 dimensional (1-D) root search where the experimental S-parameter

value is compared to a theoretical S-parameter value based on an initial guess of the permittivity. Subsequent iterations are made based on the difference in the experimental and theoretical S-parameters values, until a permittivity accuracy threshold is achieved.

All of the aforementioned work focused on solving measurement problems in isotropic materials. The construct of a Forward Problem development and Inverse Solution extraction can be applied to any material characterization problem, as long as the measurement technique and type of Material Under Test (MUT) is accurately posed. The forward problem complexity increases as the type of MUT changes from isotropic through bi-anisotropic. As a result, the number of unique measurements needed to solve the inverse solution also increases. Various measurement techniques are limited by the number of unique measurements that can be performed on a given sample by a given field applicator. Using traditional rectangular waveguide material measurement techniques and the appropriate mathematical material parameter extraction development, poses challenges in anisotropic material characterization, namely multiple samples are required to provide enough measurement information as seen in Figure 2. Each sample needs to be a different measurement orientation of the parent material, so that it properly fits into the rectangular waveguide. A problem with multiple samples is that it induces measurement error, because each sample is subject to its own independent error sources. Having multiple samples makes it difficult to conclusively say that the results of three independent samples are truly representative of the parent anisotropic material.

Uslenghi [5] demonstrated a potential waveguide measurement capability using TE_{10} and TE_{20} modes for measuring biaxial anisotropic materials. The measurement procedure suggests using multiple sample orientations to provide sufficient measurement diversity to obtain all of the constitutive tensor elements. However, because of

Traditional Measurement Technique

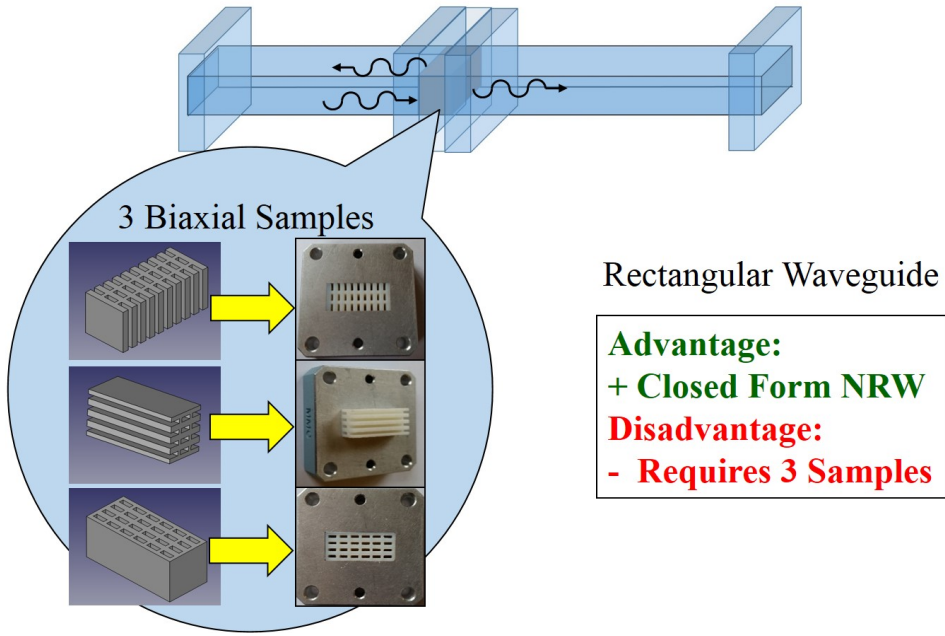


Figure 2. Rectangular Waveguide Anisotropic Sample Measurement

the rectangular waveguide design, and the desire to keep samples thin, at least two different samples of the same material would be required to accommodate a complete measurement.

Crowgey [6] was able to overcome the multiple sample requirement by utilizing a cubic sample and sample holder. The cubic sample could be indexed about its six sides, while maintaining a uniform fit in the sample holder. The cubic sample holder mounted to a rectangular waveguide, as a square reduced aperture. The reduced aperture posed two problems. The first being higher order modal excitation from the abrupt reduction in the waveguide sample holder. This required a modal analysis to perform material parameter extraction, which is more complex than a closed form NRW analysis. The second problem is that the narrow aperture significantly reduces transmitted signal strength. If the sample exhibits enough loss, the reduced aperture will reduce the transmission measurement, which can prevent a successful material

parameter extraction due to poor signal to noise ratio.

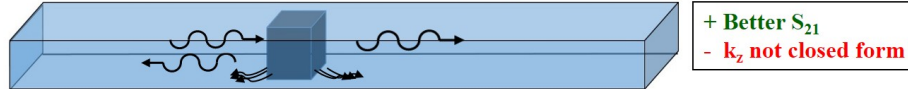
Tang [7] posed an alternative method, where a cubic sample was placed in the center of the rectangular waveguide without the reduced aperture, thereby enhancing transmission performance. The material parameter extraction development however, is significantly more complicated, because the constraint equations which describe the sample-waveguide scenario, are not closed form and require an iterative numerical analysis to determine field behavior. Additionally, higher order modes are still excited because the sample does not uniformly fill the cross-sectional dimensions of the waveguide.

Evolution of the WRWS Design

Reduced Aperture Technique [Crowgey]



Open Aperture Technique [Tang]



Waveguide Rectangular to Waveguide Square (WRWS) Technique

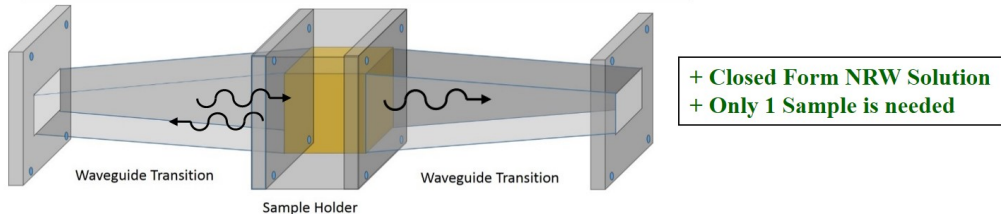


Figure 3. Evolution of WRWS system

Incorporating the closed form NRW approach and measuring the different orientations of a single cubic sample, a new measurement apparatus was developed and published [8] as part of this thesis effort as shown in Figure 3. The Waveguide Rectangular to Waveguide Square (WRWS) system, has a cubic sample holder and gradual waveguide transitions that accommodate standard X-band rectangular waveguide

and the cubic sample holder. These gradual transitions ensure that only the fundamental TE_{10} mode is excited and supports closed form, analytic solutions for biaxial anisotropic material parameter extraction. The WRWS system is addressed in the remaining chapters and utilized for making biaxial anisotropic material measurements.

2.2 Anisotropic Materials

Early developments in engineered microwave anisotropic materials are discussed in Collin's work [9]. Collin provides several theoretical developments that are used in anisotropic material design. He posed that isotropic materials of different permittivities and permeabilities could be used in combinations to synthesize different anisotropic effects. A requirement was also identified, which says that the material arrangements must be electrically small with respect to the intended operating frequency. Specifically, inclusions or the combination of two materials need to be “less than about $\frac{3}{10}\lambda$ ” [9] to adhere to macroscopic electromagnetics. Collin also demonstrates two geometries which produce anisotropic behavior: A Uniaxial Anisotropic material made by alternating slabs of two different materials; and a Bi-axial Anisotropic material made by periodic, uniformly spaced three dimensional rectangular inclusions inside a host material. This three dimensional rectangular structure serves as the initial basis for the biaxial material design evaluated in the WRWS system.

More recently, research by Dmitriev [10] provides guidance on anisotropic material design by crystallographic symmetry, as opposed to an iterative, trial and error design methodology. Dmitriev shows that arrangements of different electric and magnetic geometries with specific symmetries can be used to design different kinds of anisotropy. Dmitriev utilizes Curie's and Neumann's Principles to mathematically predict material tensor structure. Crystallographic sample design as shown in Figure 4 is a

ground up approach to anisotropic sample development because it utilizes combinations of different geometric symmetries to design specific anisotropic performance characteristics.

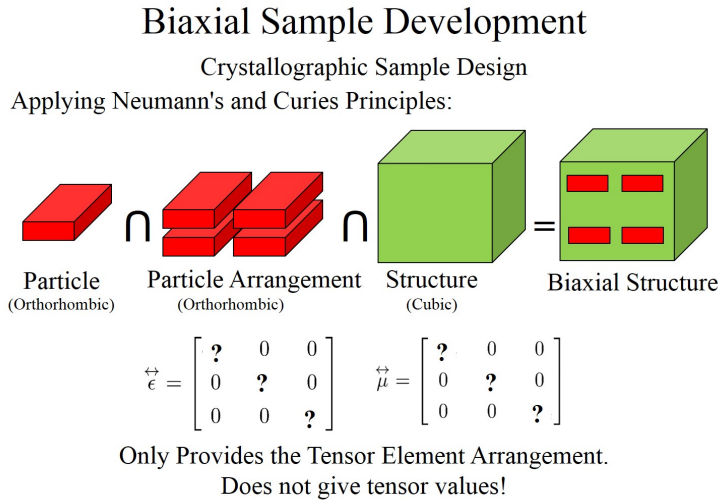


Figure 4. Demonstrating Collin's Sample Design is Biaxial Anisotropic

2.3 Biaxial Anisotropic Material Selection and Research Usage

Biaxial anisotropic materials are selected to fully exercise the measurement capabilities of the WRWS system, because of their unique permittivities and permeabilities in the x, y and z directions. The WRWS system can provide six unique measurements of a cubic sample. Interrogation of a biaxial anisotropic sample with the WRWS system allows for six unambiguous measurements of the fully biaxial anisotropic constitutive tensors in a sample. Additionally, the development of a biaxial anisotropic material demonstrate an additional degree of freedom over uniaxial materials, and potentially offer a new material to be utilized in various microwave systems, such as radomes, antennas, or absorbers/coatings. Understanding how these materials operate is critical to devising appropriate applications, and making accurate measurements.

2.4 TEM waves at an Oblique Incidence on a Biaxial Anisotropic Slab

The purpose of this analysis is to demonstrate the electromagnetic performance of a biaxial anisotropic material and to identify how best to measure the material. The goal is to obtain the transmission and reflection coefficients of a biaxial slab because these values can be measured and readily adapted to support material performance visualization simulations.

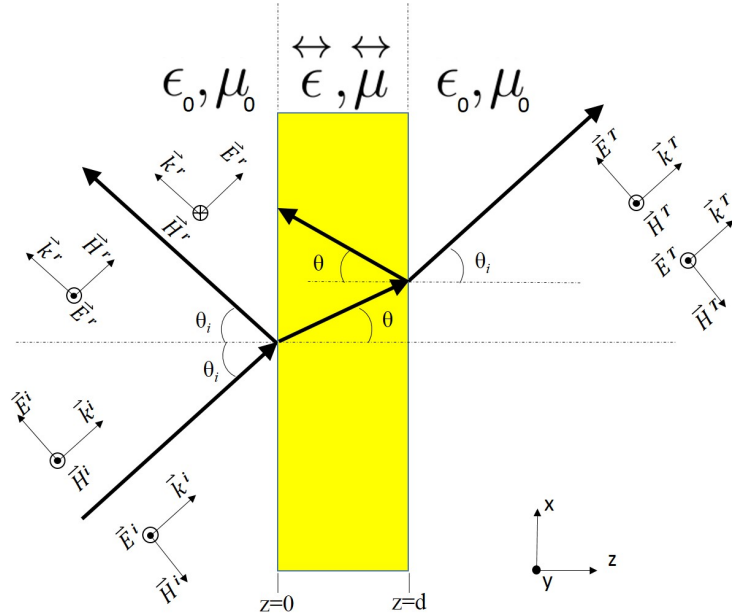


Figure 5. 2-D Biaxial Slab problem

Assume a slab of material exists that is infinite in extent in the x - y plane and has finite thickness in the z direction. Either side of this slab is immersed in free-space, while the slab itself is made of a homogeneous biaxial anisotropic material aligned with the optic axis (i.e. the z -axis). The entire region is source free, and is only excited by plane waves obliquely incident upon the slab with wave vector \vec{k} lying in the x - z plane. These plane waves possess electric fields that are either parallel or perpendicular to the x - z plane. This problem is represented by the picture shown in Figure 5.

Field Analysis.

The reflection and transmission coefficients of a biaxial slab under oblique incidence plane-wave illumination are found via field expansion and boundary condition enforcement. Since the field regions on either side of the slab are assumed to be free-space, only the detailed analysis of the biaxial region is provided. The free-space regions are obtained via the appropriate specialization of the biaxial results. Maxwell's equations for a source free biaxial region are

$$\nabla \times \vec{E} = -j\omega \overset{\leftrightarrow}{\mu} \cdot \vec{H}, \quad \nabla \times \vec{H} = j\omega \overset{\leftrightarrow}{\epsilon} \cdot \vec{E} \quad (2.3)$$

where the permittivity $\overset{\leftrightarrow}{\epsilon}$ and permeability $\overset{\leftrightarrow}{\mu}$ tensors are described as

$$\overset{\leftrightarrow}{\epsilon} = \begin{bmatrix} \epsilon_{xx} & 0 & 0 \\ 0 & \epsilon_{yy} & 0 \\ 0 & 0 & \epsilon_{zz} \end{bmatrix}, \quad \overset{\leftrightarrow}{\mu} = \begin{bmatrix} \mu_{xx} & 0 & 0 \\ 0 & \mu_{yy} & 0 \\ 0 & 0 & \mu_{zz} \end{bmatrix} \quad (2.4)$$

for a biaxial anisotropic material. Under this plane-wave assumption in which $\vec{E}(\vec{r}) = \vec{E}_0 e^{-j\vec{k} \cdot \vec{r}}$ and $\vec{H}(\vec{r}) = \vec{H}_0 e^{-j\vec{k} \cdot \vec{r}}$, Maxwell's equations may be written as

$$-jk \cdot \vec{E} = -j\omega \overset{\leftrightarrow}{\mu} \cdot \vec{H}, \quad -jk \cdot \vec{H} = j\omega \overset{\leftrightarrow}{\epsilon} \cdot \vec{E} \quad (2.5)$$

where

$$\overset{\leftrightarrow}{k} = \vec{k} \times \overset{\leftrightarrow}{I} = \begin{bmatrix} 0 & -k_z & k_y \\ k_z & 0 & -k_x \\ -k_y & k_x & 0 \end{bmatrix}. \quad (2.6)$$

Solving for \vec{H} in Faraday's Law of (2.5) leads to

$$\vec{H} = \frac{1}{\omega} \overset{\leftrightarrow}{\mu}^{-1} \cdot \overset{\leftrightarrow}{k} \cdot \vec{E} \quad (2.7)$$

and subsequent insertion into Ampere's Law yields the wave equation

$$[-\overset{\leftrightarrow}{\mu} \cdot \overset{\leftrightarrow}{k} \cdot \overset{\leftrightarrow}{\mu}^{-1} \cdot \overset{\leftrightarrow}{k} - \omega^2 \overset{\leftrightarrow}{\mu} \cdot \overset{\leftrightarrow}{\epsilon}] \cdot \vec{E} = 0 \quad (2.8)$$

or $\overset{\leftrightarrow}{W} \cdot \vec{E} = 0$ since $e^{-j\vec{k} \cdot \vec{r}} \neq 0$. Equation (2.8) is an algebraic matrix equation for wave number k_z and has a non-trivial solution only if the determinate of $\overset{\leftrightarrow}{W}$ equals zero. The roots of the characteristic polynomial (i.e. the roots of $\det \overset{\leftrightarrow}{W} = 0$) represents the allowed eigen values (i.e. propagation constants k_z). Insertion of these eigen values into (2.8) lead to the corresponding eigen vectors (i.e. the electric field structure). Simple matrix operations show that $\overset{\leftrightarrow}{W}$ takes on the form

$$\overset{\leftrightarrow}{W} = \begin{bmatrix} \frac{k_z^2 \mu_x}{\mu_y} - \epsilon_x \mu_x w^2 & 0 & -\frac{k_x k_z \mu_x}{\mu_y} \\ 0 & \frac{k_z^2 \mu_y}{\mu_z} - \epsilon_y \mu_y w^2 + \frac{k_z^2 \mu_y}{\mu_x} & 0 \\ -\frac{k_x k_z \mu_z}{\mu_y} & 0 & \frac{k_x^2 \mu_z}{\mu_y} - \epsilon_z \mu_z w^2 \end{bmatrix}. \quad (2.9)$$

Taking the determinate of $\overset{\leftrightarrow}{W}$, and setting it equal to zero leads to the following allowed eigen values

$$\begin{aligned} k_z &= \pm \sqrt{\omega^2 \epsilon_x \mu_y - \frac{\epsilon_x}{\epsilon_z} k_x^2} \\ k_z &= \pm \sqrt{\omega^2 \epsilon_y \mu_x - \frac{\mu_x}{\mu_z} k_x^2} \end{aligned} \quad (2.10)$$

These four solutions for k_z give physical insight into how the fields propagate in biaxial anisotropic media. The solutions $\pm k_z^\parallel = \pm \sqrt{\omega^2 \epsilon_x \mu_y - \frac{\epsilon_x}{\epsilon_z} k_x^2}$ represent the forward and reverse propagating waves that are in a parallel polarization state, while $\pm k_z^\perp = \pm \sqrt{\omega^2 \epsilon_y \mu_x - \frac{\mu_x}{\mu_z} k_x^2}$ represent forward and reverse propagating waves in the

perpendicular polarization state for a biaxial anisotropic material as is shown in Figure 5. Note, the free-space region characteristics are obtained from these biaxial results by letting $\epsilon_{xx} = \epsilon_{yy} = \epsilon_{zz} = \epsilon_0$ and $\mu_{xx} = \mu_{yy} = \mu_{zz} = \mu_0$. Thus in free-space, $k_z = \pm\sqrt{\omega^2\epsilon_0\mu_0 - k_x^2}$, (with k_x determined from the boundary conditions).

Evaluating the parallel polarization case using $\pm k_z^\parallel$ yields

$$\begin{bmatrix} -\frac{\epsilon_x k_x^2 \mu_x}{\epsilon_z \mu_y} & 0 & \mp \frac{k_x \mu_x k_z^\parallel}{\mu_y} \\ 0 & \frac{k_x^2 \mu_y}{\mu_z} - \epsilon_y \mu_y \omega^2 - \frac{\mu_y}{\mu_x} k_z^{2\parallel} & 0 \\ \mp \frac{k_x \mu_z k_z^\parallel}{\mu_y} & 0 & \frac{\mu_z k_x^2}{\mu_y} - \epsilon_z \mu_z \omega^2 \end{bmatrix} \cdot \begin{bmatrix} E_{0x} \\ E_{0y} \\ E_{0z} \end{bmatrix} = 0. \quad (2.11)$$

Exchanging rows 2 and 3 and then columns 2 and 3 results in

$$\begin{bmatrix} -\frac{\epsilon_x k_x^2 \mu_x}{\epsilon_z \mu_y} & \mp \frac{k_x \mu_x k_z^\parallel}{\mu_y} & 0 \\ \mp \frac{k_x \mu_z k_z^\parallel}{\mu_y} & \frac{\mu_z k_x^2}{\mu_y} - \epsilon_z \mu_z \omega^2 & 0 \\ 0 & 0 & \frac{k_x^2 \mu_y}{\mu_z} - \epsilon_y \mu_y \omega^2 - \frac{\mu_y}{\mu_x} k_z^{2\parallel} \end{bmatrix} \cdot \begin{bmatrix} E_{0x} \\ E_{0z} \\ E_{0y} \end{bmatrix} = 0. \quad (2.12)$$

Multiplying row 1 by $\pm \frac{\mu_y}{\mu_x} k_z^\parallel$ and row 2 by $\frac{\mu_y \epsilon_x}{\mu_x \epsilon_z} k_x$ yields

$$\begin{bmatrix} \mp \frac{\epsilon_x}{\epsilon_z} k_x^2 k_z^\parallel & -k_x k_z^{2\parallel} & 0 \\ \mp \frac{\epsilon_x}{\epsilon_z} k_x^2 k_z^\parallel & -k_x k_z^{2\parallel} & 0 \\ 0 & 0 & \frac{k_x^2 \mu_y}{\mu_z} - \epsilon_y \mu_y \omega^2 - \frac{\mu_y}{\mu_x} k_z^{2\parallel} \end{bmatrix} \cdot \begin{bmatrix} E_{0x} \\ E_{0z} \\ E_{0y} \end{bmatrix} = 0. \quad (2.13)$$

Separating the elements that are in the x-z plane

$$\begin{bmatrix} \mp \frac{\epsilon_x}{\epsilon_z} k_x^2 k_z^\parallel & -k_x k_z^{2\parallel} \\ \mp \frac{\epsilon_x}{\epsilon_z} k_x^2 k_z^\parallel & -k_x k_z^{2\parallel} \end{bmatrix} \cdot \begin{bmatrix} E_{0x} \\ E_{0z} \end{bmatrix} = 0 \quad (2.14)$$

and the part that is in the y direction

$$\begin{bmatrix} \frac{k_x^2 \mu_y}{\mu_z} - \epsilon_y \mu_y \omega^2 - \frac{\mu_y}{\mu_x} k_z^{2\parallel} \\ E_{0y} \end{bmatrix} = 0, \quad (2.15)$$

indicates that the parallel polarization only supports parallel polarization fields, because $E_{0z} = \mp \frac{\epsilon_x k_x}{\epsilon_z k_z^\parallel} E_{0x}$ and $E_{0y} = 0$. E_y must equal zero because the eigen vector equaling zero yields a trivial solution. Therefore the fields supported in the parallel polarization are $\vec{E} = (\hat{x} \mp \hat{z} \frac{\epsilon_x k_x}{\epsilon_z k_z^\parallel}) E_{0x} e^{-jk_x x \mp jk_z^\parallel z}$. Evaluating the perpendicular polarization case using $\pm k_z^\perp$ yields

$$\begin{bmatrix} \frac{k_z^{2\perp} \mu_x}{\mu_y} - \epsilon_x \mu_x w^2 & 0 & \mp \frac{k_x k_z^\perp \mu_x}{\mu_y} \\ 0 & 0 & 0 \\ \mp \frac{k_x k_z^\perp \mu_x}{\mu_y} & 0 & \frac{k_x^2 \mu_z}{\mu_y} - \epsilon_z \mu_z w^2 \end{bmatrix} \cdot \begin{bmatrix} E_{0x} \\ E_{0y} \\ E_{0z} \end{bmatrix} = 0. \quad (2.16)$$

Exchanging rows 2 and 3 and then columns 2 and 3 yields

$$\begin{bmatrix} \frac{k_z^{2\perp} \mu_x}{\mu_y} - \epsilon_x \mu_x w^2 & \mp \frac{k_x k_z^\perp \mu_x}{\mu_y} & 0 \\ \mp \frac{k_x k_z^\perp \mu_z}{\mu_y} & \frac{k_x^2 \mu_z}{\mu_y} - \epsilon_z \mu_z w^2 & 0 \\ 0 & 0 & 0 \end{bmatrix} \cdot \begin{bmatrix} E_{0x} \\ E_{0z} \\ E_{0y} \end{bmatrix} = 0. \quad (2.17)$$

Multiplying row 1 by $\pm \frac{\mu_y}{\mu_x} k_z^\perp$ and row 2 by $\frac{\mu_y}{\mu_z} k_x$ yields

$$\begin{bmatrix} \mp \frac{\mu_x}{\mu_z} k_x^2 k_z^\perp & -k_x k_z^{2\perp} & 0 \\ \pm k_x^2 k_z^\perp & -k_x^3 + k_x \epsilon_z \mu_y \omega^2 & 0 \\ 0 & 0 & 0 \end{bmatrix} \cdot \begin{bmatrix} E_{0x} \\ E_{0z} \\ E_{0y} \end{bmatrix} = 0. \quad (2.18)$$

Substituting $k_z^{2\perp}$ in for the element(1,2) and multiplying row 1 by $\frac{\mu_z}{\mu_x}$ yields

$$\begin{bmatrix} \mp k_x^2 k_z^\perp & -k_x \epsilon_y \mu_z \omega^2 + k_x^3 & 0 \\ \pm k_x^2 k_z^\perp & k_x \epsilon_z \mu_y \omega^2 - k_x^3 & 0 \\ 0 & 0 & 0 \end{bmatrix} \cdot \begin{bmatrix} E_{0x} \\ E_{0z} \\ E_{0y} \end{bmatrix} = 0. \quad (2.19)$$

Adding row 1 to row 2 yields

$$\begin{bmatrix} \mp k_x^2 k_z^\perp & -k_x \frac{\epsilon_x \mu_y \mu_z}{\mu_x} \omega^2 + k_x^3 & 0 \\ 0 & k_x \omega^2 (\epsilon_z \mu_y - \epsilon_y \mu_z) & 0 \\ 0 & 0 & 0 \end{bmatrix} \cdot \begin{bmatrix} E_{0x} \\ E_{0z} \\ E_{0y} \end{bmatrix} = 0. \quad (2.20)$$

Separating the parallel and perpendicular components yields

$$\begin{bmatrix} \mp k_x^2 k_z^\perp & -k_x \frac{\epsilon_x \mu_y \mu_z}{\mu_x} \omega^2 + k_x^3 \\ 0 & k_x \omega^2 (\epsilon_z \mu_y - \epsilon_y \mu_z) \end{bmatrix} \cdot \begin{bmatrix} E_{0x} \\ E_{0z} \end{bmatrix} = 0 \quad (2.21)$$

and

$$\begin{bmatrix} 0 \end{bmatrix} \cdot \begin{bmatrix} E_{0y} \end{bmatrix} = 0. \quad (2.22)$$

The evaluation shows that perpendicular polarization only supports perpendicular polarization fields because $E_y \neq 0$ and E_x and E_z must equal zero. Therefore the fields supported in the perpendicular polarization are $\vec{E} = \pm \hat{y} E_{0y} e^{-jk_x x \mp jk_z^\perp z}$.

The magnetic field equations for each polarization are then obtained by inserting each polarization of the electric field into (2.7). Inserting the parallel polarization yields

$$\begin{bmatrix} 0 & \mp \frac{k_z^\parallel}{\mu_x \omega} & 0 \\ \pm \frac{k_z^\parallel}{\mu_y \omega} & 0 & -\frac{k_x}{\mu_y \omega} \\ 0 & \frac{k_x}{\mu_z \omega} & 0 \end{bmatrix} \cdot \begin{bmatrix} E_{0x} \\ 0 \\ \mp \frac{\epsilon_x k_x}{\epsilon_z k_z^\parallel} E_{0x} \end{bmatrix} = \begin{bmatrix} H_{0x} \\ H_{0y} \\ H_{0z} \end{bmatrix} \quad (2.23)$$

which results in a y directed magnetic field,

$$\vec{H} = \hat{y} \left(\pm \frac{k_z^\parallel}{\mu_y \omega} \pm \frac{k_x}{\mu_y \omega} \frac{\epsilon_x k_x}{\epsilon_z k_z^\parallel} \right) E_{0x} e^{-jk_x x \mp jk_z^\parallel z} \quad (2.24)$$

and simplifies to

$$\vec{H} = \pm \hat{y} \left(\frac{\omega \epsilon_y}{k_z^\parallel} \right) E_{0x} e^{-jk_x x \mp jk_z^\parallel z}. \quad (2.25)$$

The wave impedance is defined as the ratio of the tangential electric field over the tangential magnetic field for a single traveling wave, which yields $\eta_2^\parallel = \frac{k_z^\parallel}{\omega \epsilon_y}$. Inserting the perpendicular polarization yields

$$\begin{bmatrix} 0 & \mp \frac{k_z^\perp}{\mu_x \omega} & 0 \\ \pm \frac{k_z^\perp}{\mu_y \omega} & 0 & -\frac{k_x}{\mu_y \omega} \\ 0 & \frac{k_x}{\mu_z \omega} & 0 \end{bmatrix} \cdot \begin{bmatrix} 0 \\ \pm E_{0y} \\ 0 \end{bmatrix} = \begin{bmatrix} H_{0x} \\ H_{0y} \\ H_{0z} \end{bmatrix} \quad (2.26)$$

which results in a x and z directed magnetic field,

$$\vec{H} = \left(\mp \frac{k_z^\perp}{\mu_x \omega} \hat{x} + \frac{k_x}{\mu_z \omega} \hat{z} \right) E_{0y} e^{-jk_x x \mp jk_z^\perp z} \quad (2.27)$$

and simplifies to

$$\vec{H} = \mp \frac{k_z^\perp}{\mu_x \omega} \left(\hat{x} \mp \frac{\mu_x}{\mu_z} \frac{k_x}{k_z^\perp} \hat{z} \right) E_{0y} e^{-jk_x x \mp jk_z^\perp z}. \quad (2.28)$$

The wave impedance for the perpendicular case is $\eta_2^\perp = \frac{\omega \mu_x}{k_z^\perp}$. Having the fields, impedances and propagation constants for each polarization provides the required information to enforce boundary conditions and solve for the transmission and reflection coefficients.

Mathematically describing the incident, transmitted and reflected waves featured by the scenario in Figure 5 yields the follow equations for both the parallel and perpendicular polarizations. Each polarization is separated and evaluated as its own

problem and has its own transmission T^\perp , T^\parallel and reflection Γ^\perp , Γ^\parallel coefficients. These terms relate the transmitted and reflected fields to the incident field. By adding both the perpendicular and parallel polarization fields together the total fields can be obtained for the transmitted and reflected responses associated with a given incident field. This summation of fields on either side of the biaxial media provides the net effects of a plane wave incident on a biaxial slab.

Evaluation of the Parallel Polarization.

The parallel wave case is evaluated first and has the following fields in the regions defined by Figure 5:

Fields Region 1 (Free-space Region):

$$\vec{E}^{i\parallel} = (\hat{x} - \hat{z} \frac{k_x}{k_z}) E_{0x} e^{-jk_x x - jk_z z} \quad (2.29)$$

$$\begin{aligned} \vec{H}^{i\parallel} &= \hat{y} \frac{E_{0x}}{\eta_1} e^{-jk_x x - jk_z z} \\ \vec{E}^{r\parallel} &= (\hat{x} + \hat{z} \frac{k_x}{k_z}) \Gamma^\parallel E_{0x} e^{-jk_x x + jk_z z} \\ \vec{H}^{r\parallel} &= -\hat{y} \Gamma^\parallel \frac{E_{0x}}{\eta_1} e^{-jk_x x + jk_z z} \end{aligned} \quad (2.30)$$

Fields Region 2 (Biaxial Anisotropic Slab):

$$\vec{E}^{t\parallel} = (\hat{x} - \hat{z} \frac{\epsilon_x k_x}{\epsilon_z k_z^\parallel}) t^\parallel E_{0x} e^{-jk_x x - jk_z^\parallel z} \quad (2.31)$$

$$\begin{aligned} \vec{H}^{t\parallel} &= \hat{y} t^\parallel \frac{E_{0x}}{\eta_2^\parallel} e^{-jk_x x - jk_z^\parallel z} \\ \vec{E}^{r1\parallel} &= (\hat{x} + \hat{z} \frac{\epsilon_x k_x}{\epsilon_z k_z^\parallel}) \Gamma_1^\parallel E_{0x} e^{-jk_x x + jk_z^\parallel z} \end{aligned} \quad (2.32)$$

$$\vec{H}^{r1\parallel} = -\hat{y}\Gamma_1^{\parallel} \frac{E_{0x}}{\eta_2^{\parallel}} e^{-jk_x x + jk_z^{\parallel} z}.$$

Fields Region 3 (Free-space Region):

$$\vec{E}^{T\parallel} = (\hat{x} - \hat{z} \frac{k_x}{k_z}) T^{\parallel} E_{0x} e^{-jk_x x - jk_z(z-d)} \quad (2.33)$$

$$\vec{H}^{T\parallel} = \hat{y} T^{\parallel} \frac{E_{0x}}{\eta_1} e^{-jk_x x - jk_z(z-d)}$$

Enforcing the continuity of tangential \vec{E} and \vec{H} at each of the region interfaces requires that $k_x = k_0 \sin \theta_i$ be equivalent on either side of the interface by Snell's Law.

Interface 1 ($z=0$):

$$1 + \Gamma^{\parallel} = t^{\parallel} + \Gamma_1^{\parallel} \quad (2.34)$$

$$\frac{1}{\eta_1} (1 - \Gamma^{\parallel}) = \frac{1}{\eta_2^{\parallel}} (t^{\parallel} - \Gamma_1^{\parallel}) \quad (2.35)$$

Interface 2 ($z=d$):

$$t^{\parallel} e^{-jk_z^{\parallel} z} + \Gamma_1^{\parallel} e^{jk_z^{\parallel} z} = T^{\parallel} \quad (2.36)$$

$$\frac{\eta_1}{\eta_2^{\parallel}} \left(t^{\parallel} e^{-jk_z^{\parallel} z} - \Gamma_1^{\parallel} e^{jk_z^{\parallel} z} \right) = T^{\parallel} \quad (2.37)$$

Solving for the reflection coefficient Γ_1^{\parallel} , (2.37) is set equal to (2.36):

$$\frac{\eta_1}{\eta_2^{\parallel}} \left(t^{\parallel} e^{-jk_z^{\parallel} z} - \Gamma_1^{\parallel} e^{jk_z^{\parallel} z} \right) = t^{\parallel} e^{-jk_z^{\parallel} z} + \Gamma_1^{\parallel} e^{jk_z^{\parallel} z}. \quad (2.38)$$

Substituting

$$P = e^{-jk_z^{\parallel} z} \quad (2.39)$$

into (2.38) and simplifying:

$$\eta_1 t^{\parallel} P - \eta_1 \Gamma_1^{\parallel} P^{-1} = \eta_2^{\parallel} t^{\parallel} P + \eta_2^{\parallel} \Gamma_1^{\parallel} P^{-1} \quad (2.40)$$

$$\eta_1 t^{\parallel} P^2 - \eta_1 \Gamma_1^{\parallel} = \eta_2^{\parallel} t^{\parallel} P^2 + \eta_2 \Gamma_1^{\parallel} \quad (2.41)$$

$$\eta_1 t^{\parallel} P^2 - \eta_2^{\parallel} t^{\parallel} P^2 = \eta_1 \Gamma_1^{\parallel} + \eta_2^{\parallel} \Gamma_1^{\parallel} \quad (2.42)$$

$$-t^{\parallel} P^2 \frac{(\eta_2^{\parallel} - \eta_1)}{(\eta_2^{\parallel} + \eta_1)} = \Gamma_1^{\parallel} \quad (2.43)$$

yields

$$-t^{\parallel} P^2 R = \Gamma_1^{\parallel}, \quad (2.44)$$

where

$$R = \frac{\eta_2^{\parallel} - \eta_1}{\eta_2^{\parallel} + \eta_1}. \quad (2.45)$$

Equating (2.34) and (2.35) from the $z = 0$ interface and substituting in Γ_1^{\parallel} from (2.44),

$$\frac{\eta_2^{\parallel}(1 - \Gamma^{\parallel})}{\eta_1(1 + \Gamma^{\parallel})} = \frac{t^{\parallel}(1 + P^2 R)}{t^{\parallel}(1 - P^2 R)} \quad (2.46)$$

and simplifying:

$$\eta_2^{\parallel}(1 - \Gamma^{\parallel})(1 - P^2 R) = \eta_1(1 + \Gamma^{\parallel})(1 + P^2 R) \quad (2.47)$$

$$\eta_2^{\parallel}(1 - P^2 R) - \eta_2^{\parallel}\Gamma^{\parallel}(1 - P^2 R) = \eta_1(1 + P^2 R) + \eta_1\Gamma^{\parallel}(1 + P^2 R) \quad (2.48)$$

$$(\eta_2^{\parallel} - \eta_1) - P^2 R(\eta_2^{\parallel} + \eta_1) = \Gamma^{\parallel} (\eta_1 + \eta_2^{\parallel}) - \Gamma^{\parallel} P^2 R (\eta_2^{\parallel} - \eta_1) \quad (2.49)$$

$$R - P^2 R = \Gamma^{\parallel} - \Gamma^{\parallel} P^2 R^2 \quad (2.50)$$

yields:

$$\frac{R(1 - P^2)}{1 - P^2 R^2} = \Gamma^{\parallel}. \quad (2.51)$$

Taking (2.51) and (2.44) and inserting it into (2.34), and simplifying yields

$$\frac{1 + R}{1 - P^2 R^2} = t^{\parallel} \quad (2.52)$$

Inserting (2.52) and (2.51) into (2.36);

$$\frac{1+R}{1-P^2R^2}P - \frac{1+R}{1-P^2R^2}P^2RP^{-1} = T^{\parallel} \quad (2.53)$$

and simplifying

$$\frac{1+R}{1-P^2R^2}P - \frac{1+R}{1-P^2R^2}PR = T^{\parallel} \quad (2.54)$$

$$\frac{P+PR}{1-P^2R^2} - \frac{PR+PR^2}{1-P^2R^2} = T^{\parallel} \quad (2.55)$$

yields:

$$\frac{P(1-R^2)}{1-P^2R^2} = T^{\parallel}. \quad (2.56)$$

The equations (2.51) and (2.56) are identical to the formulation devised in the NRW methodology [1], [2] and provide a way to measure a biaxial anisotropic material in free-space using the substitutions for P and R above.

Evaluation of the Perpendicular Polarization.

Repeating the same process for the perpendicular field case. The fields in each region are identified:

Fields Region 1 (Free-space Region):

$$\vec{E}^{i\perp} = \hat{y}E_{0y}e^{-jk_xx-jk_zz} \quad (2.57)$$

$$\vec{H}^{i\perp} = -\left(\hat{x} - \frac{k_x}{k_z}\hat{z}\right)\frac{E_{0y}}{\eta_1}e^{-jk_xx-jk_zz} \quad (2.58)$$

$$\vec{E}^{r\perp} = \hat{y}\Gamma^{\perp}E_{0y}e^{-jk_xx+jk_zz} \quad (2.59)$$

$$\vec{H}^{r\perp} = \left(\hat{x} + \frac{k_x}{k_z}\hat{z}\right)\Gamma^{\perp}\frac{E_{0y}}{\eta_1}e^{-jk_xx+jk_zz} \quad (2.60)$$

Fields Region 2 (Biaxial Anisotropic Slab):

$$\vec{E}^{t\perp} = \hat{y} t^\perp E_{0y} e^{-jk_x x - jk_z^\perp z} \quad (2.61)$$

$$\vec{H}^{t\perp} = - \left(\hat{x} - \frac{\mu_x}{\mu_z} \frac{k_x}{k_z^\perp} \hat{z} \right) t^\perp \frac{E_{0y}}{\eta_2^\perp} e^{-jk_x x - jk_z^\perp z} \quad (2.62)$$

$$\vec{E}^{1r\perp} = \hat{y} \Gamma_1^\perp E_{0y} e^{-jk_x x + jk_z^\perp z} \quad (2.63)$$

$$\vec{H}^{1r\perp} = \left(\hat{x} + \frac{\mu_x}{\mu_z} \frac{k_x}{k_z^\perp} \hat{z} \right) \Gamma_1^\perp \frac{E_{0y}}{\eta_2^\perp} e^{-jk_x x + jk_z^\perp z} \quad (2.64)$$

Fields Region 3 (Free-space Region):

$$\vec{E}^{t\perp} = \hat{y} T^\perp E_{0y} e^{-jk_x x - jk_z(z-d)} \quad (2.65)$$

$$\vec{H}^{t\perp} = - \left(\hat{x} - \frac{k_x}{k_z} \hat{z} \right) T^\perp \frac{E_{0y}}{\eta_1} e^{-jk_x x - jk_z(z-d)} \quad (2.66)$$

Enforcing the continuity of tangential field boundary conditions at each interface for the perpendicular polarization yields

Interface at $z=0$:

$$1 + \Gamma^\perp = t^\perp + \Gamma_1^\perp \quad (2.67)$$

$$\frac{1}{\eta_1^\perp} (1 - \Gamma^\perp) = \frac{1}{\eta_2^\perp} (t^\perp - \Gamma_1^\perp) \quad (2.68)$$

Interface at $z=d$:

$$t^\perp e^{-jk_z^\perp z} + \Gamma_1^\perp e^{jk_z^\perp z} = T^\perp \quad (2.69)$$

$$\frac{\eta_1}{\eta_2^\perp} \left(t^\perp e^{-jk_z^\perp z} - \Gamma_1^\perp e^{jk_z^\perp z} \right) = T^\perp \quad (2.70)$$

The equations that result by enforcing boundary conditions in the perpendicular case are identical to the equation that are tangential at the interfaces of the parallel case.

Identifying that $P = e^{-jk_z^\perp z}$, $R = \frac{\eta_2^\perp - \eta_1}{\eta_2^\perp + \eta_1}$ and simplifying yields equations for Γ^\perp and

T^\perp , which are identical to (2.51) and (2.56).

Having these forms for both Γ^{\parallel} , Γ^\perp and T^{\parallel} , T^\perp and their corresponding forms of R^{\parallel} , R^\perp and P^{\parallel} , P^\perp for each polarization keeps consistent with legacy material measurement developments and shows a potential methodology for how a sample could be measured. The transmission and reflection equations for the parallel and perpendicular polarization forms developed in the forward formulation are then employed in the inverse solution. The inverse solution is used for material sample measurements. Calibrated sample transmission and reflection coefficient data are collected and used as inputs to the inverse solution to provide permittivity and permeability tensor elements.

2.5 Demonstration of Biaxial Anisotropic Slab Performance

Demonstrating the effects of a biaxial slab on transmitted and reflected electric fields, MATLAB[®] code is developed which solves for the transmission and reflection coefficients for each polarization given a particular incident angle and permittivity/permeability tensor elements. The coefficients are then applied to their corresponding electric field polarizations in both free-space regions 1 and 3. The electric fields are then added together to provide the net polarization created by both parallel and perpendicular polarized fields. The incident, transmitted and reflected fields are plotted, demonstrating the polarization effects by the biaxial slab. Figure 6 demonstrates a slant 45 degree polarization electric field incident on a 0.9 inch thick simulated biaxial anisotropic slab at an oblique incidence of 45 degrees that has the

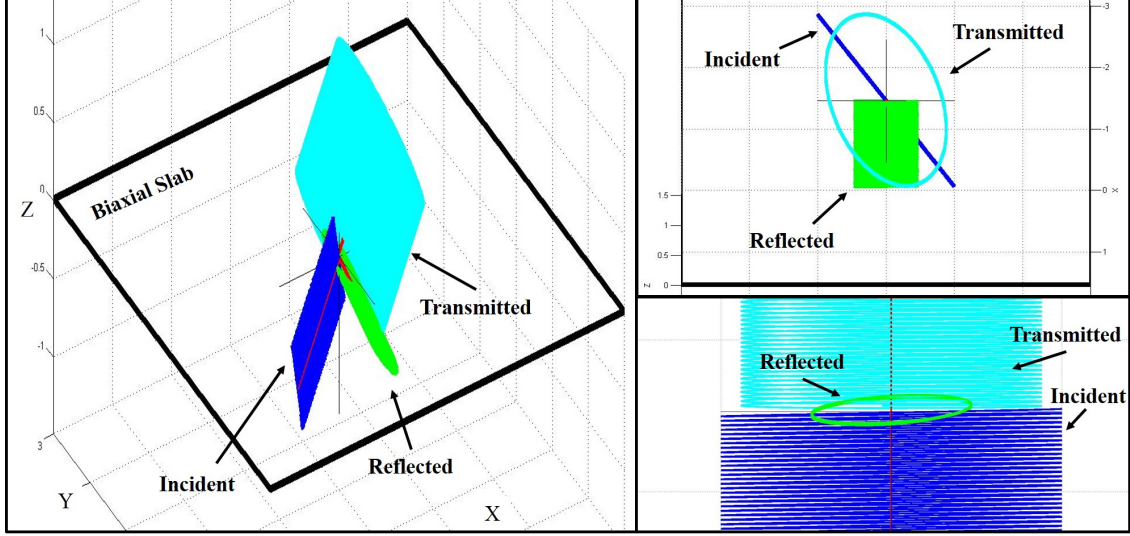


Figure 6. Left: 3-D MATLAB® Plot of Electric Field Response from a Biaxial Anisotropic Slab with constitutive tensors (2.71). Right Top: Transmitted Elliptical Polarization, Right Bottom: Reflected Elliptical Polarization.

following permittivity and permeability tensor elements:

$$\overset{\leftrightarrow}{\epsilon} = \begin{bmatrix} 2 & 0 & 0 \\ 0 & 3 & 0 \\ 0 & 0 & 4 \end{bmatrix}, \quad \overset{\leftrightarrow}{\mu} = \begin{bmatrix} 1 & 0 & 0 \\ 0 & 2 & 0 \\ 0 & 0 & 3 \end{bmatrix}. \quad (2.71)$$

The reflected and transmitted fields resulting from the slant polarized incident field have elliptical polarizations. The elliptical polarization is caused by the superposition of the parallel and perpendicular field. Each polarization travels through the slab at a different velocity governed by the propagation constants k_z^{\parallel} and k_z^{\perp} . A biaxial anisotropic material's ability to change the polarization of a wave has many potential applications, ranging from communications, electromagnetic interference and compatibility, to antenna and radome design. Control over a material's constitutive parameters provides new ways to design and gain system performance. However, constitutive parameter control demands understanding how to measure a material's tensor properties.

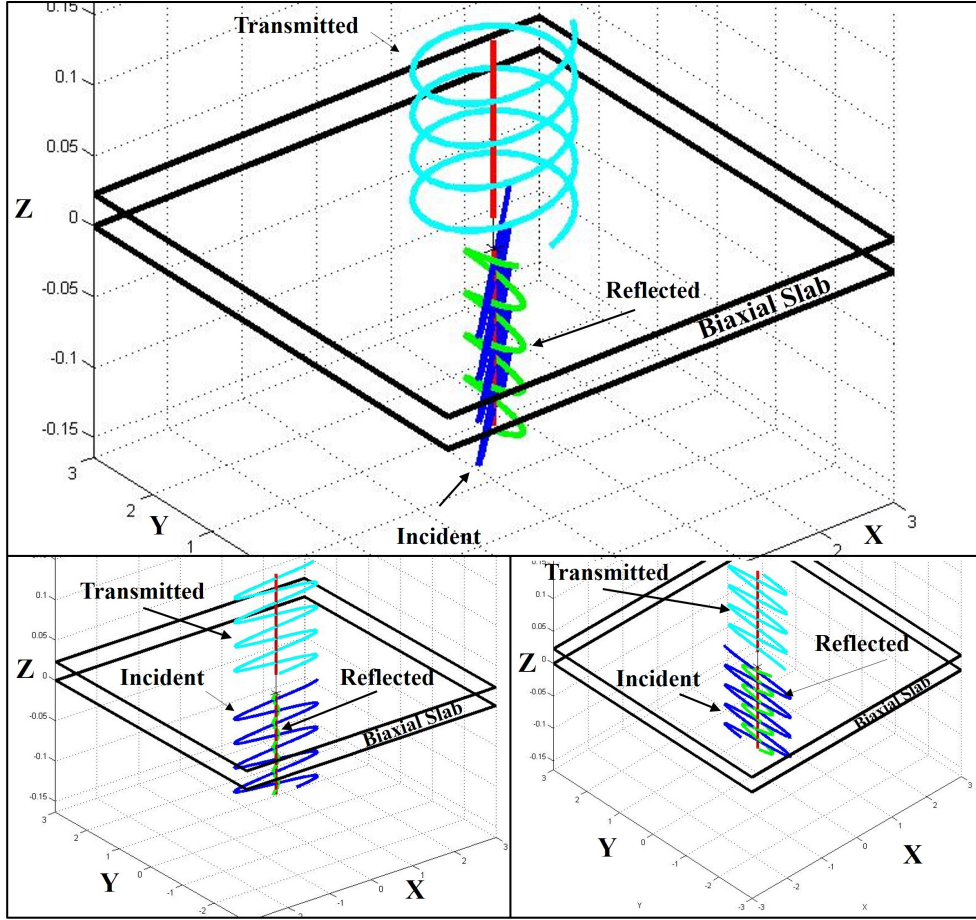


Figure 7. Top: Biaxial Slab with constitutive tensors (2.71) with Normal Incidence Electric Field at Slant polarization. Left: Parallel polarization only, Right Perpendicular polarization only.

Exploring the biaxial slab problem further in Figure 7 and noting that the tensor elements are aligned along the optic axes, it is shown that interrogating the material at normal incidence using either a perpendicular or parallel polarization produces only a perpendicular or parallel transmitted and reflected responses as shown in Figure 7. Obtaining the transmission and reflection coefficients in either of these polarizations normal to the sample provides either k_z^{\parallel} or k_z^{\perp} with $k_x = 0$. Measuring along the tensor element axes simplifies sample measurement by reducing system complexity and measures only individual polarizations. These two measurement orientations support obtaining the transverse (ϵ_{xx} or μ_{xx}, ϵ_{yy} or μ_{yy}) components, but do not provide the

longitudinal component (ϵ_{zz} or μ_{zz}). Measuring the longitudinal component would require either an oblique incidence measurement (which increase measurement system complexity to capture both polarizations) or indexing the sample to an orientation where the longitudinal axis becomes the transverse axis and measuring it at normal incidence.

2.6 Summary

The free-space analysis demonstrates the performance characteristics of a biaxial material, which could be utilized in microwave systems to change the polarization of incident waves with both vertical and horizontal polarizations. All permittivity and permeability elements can be obtained by interrogating a sample at normal incidence with respect to each tensor element. Evaluating the performance characteristics of a biaxial anisotropic sample, evaluating a sample development technique and reviewing waveguide measurement methods provides insight toward the development of a biaxial anisotropic waveguide material measurement method.

III. Measurement Methodology

Characterization of a biaxial anisotropic material using waveguide techniques requires a measurement apparatus that allows the sample to be indexed into different orientations. The Waveguide Rectangular to Waveguide Square (WRWS) measurement system supports the interrogation of a cubic sample by indexing it about its six sides. The WRWS waveguide transitions are designed such that the gradual transitions from a rectangular profile to square profile supports a TE_{10} mode of operation. This gives the WRWS method two advantages over the previously mentioned measurement techniques. The first advantage is the gradual transition supports a closed form, analytic solution for extracting the constitutive parameters ($\overset{\leftrightarrow}{\epsilon}, \overset{\leftrightarrow}{\mu}$). The second advantage is the ability to utilize only 1 cubic sample and index it about its different sides.

3.1 Waveguide Rectangular to Waveguide Square Development

The theoretical development for the WRWS system is a guided wave problem. Unlike the TEM oblique incidence example in Chapter 2, the WRWS system has additional boundary conditions which change the propagation constants and field structure. It is shown that the WRWS system supports only the fundamental TE_{10} mode at X-band and the resulting equations from the forward problem development take a form similar to the TEM wave problem. A conference paper [8] was presented and published in conjunction with the development of this thesis. The conference paper contains a short synopsis of the WRWS development and experimentation. This section provides the same information presented in greater detail, to explicitly demonstrate all parts of the WRWS theoretical development.

The TEM free-space development, demonstrated that constraint equations and

field relationships need to be identified to suit the forward problem development. Extending the field analysis process, a source-free rectangular waveguide is assumed completely filled with a biaxial anisotropic material and is infinite in extent. Evaluating the source-free form of Maxwell's Equations

$$\nabla \times \vec{E} = -j\omega \hat{\mu} \cdot \vec{H}, \quad \nabla \times \vec{H} = j\omega \hat{\epsilon} \cdot \vec{E} \quad (3.1)$$

with the biaxial anisotropic tensors (2.4); it is determined that the curl equations are y-invariant ($\frac{\partial}{\partial y} = 0$), because only the fundamental TE_{10} mode is present in the WRWS waveguide due to the system operational frequency. This allows Maxwell's equations to be separated into two sets of modal equations: TE_z and TM_z . The TM_z modal equations will yield a trivial solution of zero and cannot exist in a y-invariant structured environment. This dictates that only the TE_z modal set :

$$\frac{\partial E_y}{\partial z} = j\omega \mu_x H_x, \quad \frac{\partial E_y}{\partial x} = -j\omega \mu_z H_z \quad (3.2)$$

and

$$\frac{\partial H_z}{\partial x} - \frac{\partial H_x}{\partial z} = -j\omega \epsilon_y E_y \quad (3.3)$$

will be present in the waveguide. Substituting the TE_z field relations (3.2) into (3.3) yields the TE_z wave equation

$$\frac{\mu_x}{\mu_z} \frac{\partial^2 E_y(x, z)}{\partial x^2} + \frac{\partial^2 E_y(x, z)}{\partial z^2} = -\omega^2 \mu_x \epsilon_y E_y(x, z). \quad (3.4)$$

The general solution for (3.4), which is a second order partial differential equation, can be found using the separation of variables technique, where:

$$E_y(x, z) = f(x)h(z). \quad (3.5)$$

The goal is to identify the eigenvalue equation, obtain the general solution to the differential equation and identify the electric and magnetic field components. These equations describe the field structure and operational characteristics of the biaxial anisotropic waveguide system.

Rearranging the TE_z equation and applying the separation of variables technique to the wave equation

$$\frac{\mu_x}{\mu_z} \frac{\partial^2 E_y}{\partial x^2} + \frac{\partial^2 E_y}{\partial z^2} = -\omega^2 \mu_x \epsilon_y E_y, \quad (3.6)$$

yields,

$$\frac{\mu_x}{\mu_z} \frac{1}{f(x)} \frac{\partial^2 f(x)}{\partial x^2} + \frac{1}{h(z)} \frac{\partial^2 h(z)}{\partial z^2} = -\omega^2 \mu_x \epsilon_y. \quad (3.7)$$

The following relations are identified:

$$\omega^2 \mu_x \epsilon_y = k_t^2, \quad \frac{1}{f(x)} \frac{d^2 f(x)}{dx^2} = -k_x^2, \quad \frac{1}{h(z)} \frac{d^2 h(z)}{dz^2} = -k_z^2; \quad (3.8)$$

which leads to the constraint equation:

$$\frac{\mu_x}{\mu_z} k_x^2 + k_z^2 = k_t^2. \quad (3.9)$$

The general solution to this problem is described as traveling waves in the longitudinal direction of the waveguide, and standing waves in the transverse directions of the waveguide as represented by:

$$E_y(x, z) = (A \cos(k_x x) + B \sin(k_x x))(E e^{-jk_z z} + F e^{jk_z z}), \quad (3.10)$$

where

$$k_z = \sqrt{k_t^2 - \frac{\mu_x}{\mu_z} k_x^2}, \quad k_t^2 = \omega^2 \epsilon_y \mu_x, \quad (3.11)$$

which is the constraint equation rearranged for k_z . Enforcement of the boundary

conditions based on the waveguide's geometry, as described in [11]:

$$E_y(x, z)|_{x=0,a} = (A \cos(k_x x) + B \sin(k_x x))(E e^{-jk_z z} + F e^{jk_z z}) = 0 \quad (3.12)$$

leads to $A = 0$ when $x = 0$ and $k_x = \frac{m\pi}{a}$ when $x = a$; where $m = 1, 2, 3 \dots \infty$, which indicate the TE_{m0} modes of operation. Note that $m \neq 0$, this is a trivial solution. Further reduction yields:

$$E_y(x, z) = (B \sin(k_x x))(E e^{-jk_z z} + F e^{jk_z z}), \quad (3.13)$$

and

$$E_y(x, z) = (\sin(k_x x))(B E e^{-jk_z z} + B F e^{jk_z z}). \quad (3.14)$$

The electric field general solution is constituted in terms of forward and reverse traveling waves:

$$E_y(x, z) = (\sin(k_x x))(A_{m0}^+ e^{-jk_z z} + A_{m0}^- e^{jk_z z}) \quad (3.15)$$

where A_{m0}^+ is the forward traveling wave amplitude and A_{m0}^- is the reverse traveling wave amplitude. Writing it more generally:

$$\vec{E}^\pm = A_{m0}^\pm \vec{e}_{m0} e^{\mp jk_z z}, \quad \text{where} \quad \vec{e}_{m0} = \hat{y} \sin(k_x x). \quad (3.16)$$

The transverse and longitudinal magnetic fields are then determined, once again, similar to [11]:

$$H_x = \frac{1}{j\omega\mu_x} \frac{\partial}{\partial z} (\sin(k_x x)(A_{m0}^+ e^{-jk_z z} + A_{m0}^- e^{jk_z z})), \quad (3.17)$$

which evaluates to

$$H_x = \frac{-k_z}{\omega\mu_x} (\sin(k_x x)(A_{m0}^+ e^{-jk_z z} + A_{m0}^- e^{jk_z z})). \quad (3.18)$$

The wave impedance is defined as the ratio of the tangential electric field over the tangential magnetic field for a single traveling wave, namely

$$Z_{TE} = \mp \frac{E_y^\pm}{H_x^\pm} = \frac{\omega\mu_x}{k_z} \quad (3.19)$$

Thus, H_x is written as

$$H_x = \frac{-1}{Z_{TE}} (\sin(k_x x)(A_{m0}^+ e^{-jk_z z} + A_{m0}^- e^{jk_z z})). \quad (3.20)$$

The longitudinal magnetic field:

$$H_z = \frac{1}{-j\omega\mu_z} \frac{\partial}{\partial x} (\sin(k_x x)(A_{m0}^+ e^{-jk_z z} + A_{m0}^- e^{jk_z z})), \quad (3.21)$$

reduces to

$$H_z = \frac{-k_x}{j\omega\mu_z} (\cos(k_x x)(A_{m0}^+ e^{-jk_z z} + A_{m0}^- e^{jk_z z})). \quad (3.22)$$

The result of the biaxial anisotropic filled waveguide development yield similar information as the TEM oblique incidence example and provides the wave impedance, the constraint equation and information on how the waves propagate in the media as well as the field structure. These components are used in the inverse solution development of a biaxial filled sample region in the WRWS system.

3.2 Evaluation of Rectangular Waveguide and WRWS

A comparison of the WRWS transition and rectangular waveguide S-parameter data was performed and presented in a conference paper [12] in conjunction with the thesis development. The content below is the same as [12]. Comparisons are performed to observe the propagation differences present between the two waveguides. Simulations of the waveguide profiles are made in CST Microwave Studio® and the S-parameters are collected. Both waveguides are Perfect Electrical Conductor (PEC) structures, use CST's waveguide port excitation and are filled with free-space. Figure 8 shows that both waveguide configurations operate in only the TE_{10} mode over the 8-13 GHz band and no additional higher order modes are propagated, which matches [11]'s depiction of the fundamental operational mode of rectangular waveguide. Comparing both waveguides, it is evident in Figure 9 that there is a significant

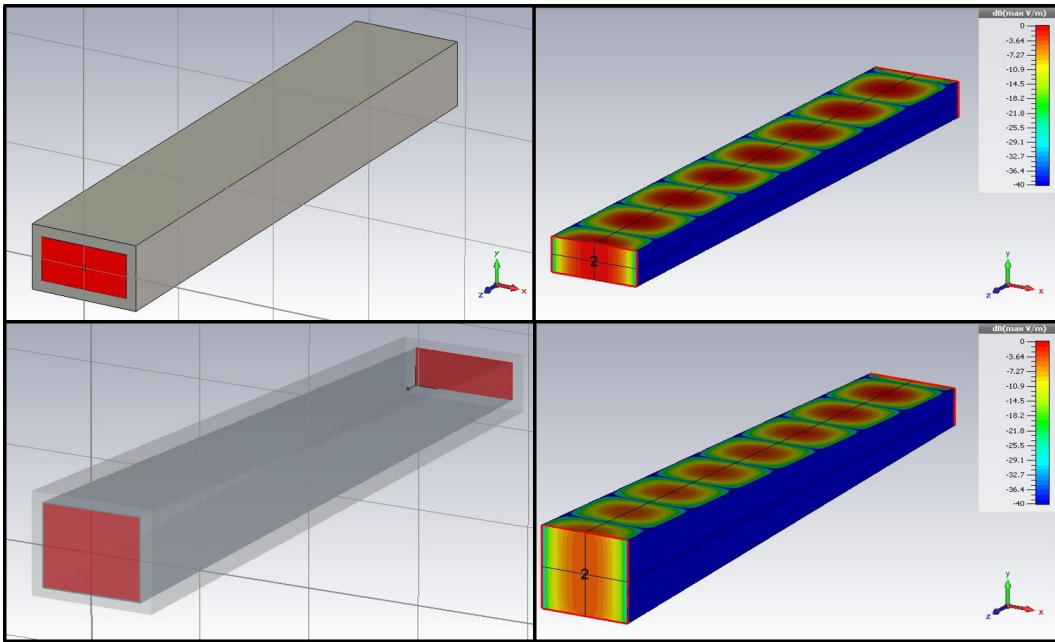


Figure 8. TE_{10} modes propagating in a Rectangular Waveguide and WRWS Transition guide

difference in transmission and reflection performance between both the rectangular waveguide and the WRWS structures. The WRWS transition exhibits more signifi-

cant reflections than the rectangular waveguide and the power transmitted through the WRWS transition has a greater sensitivity to the operational frequency. The

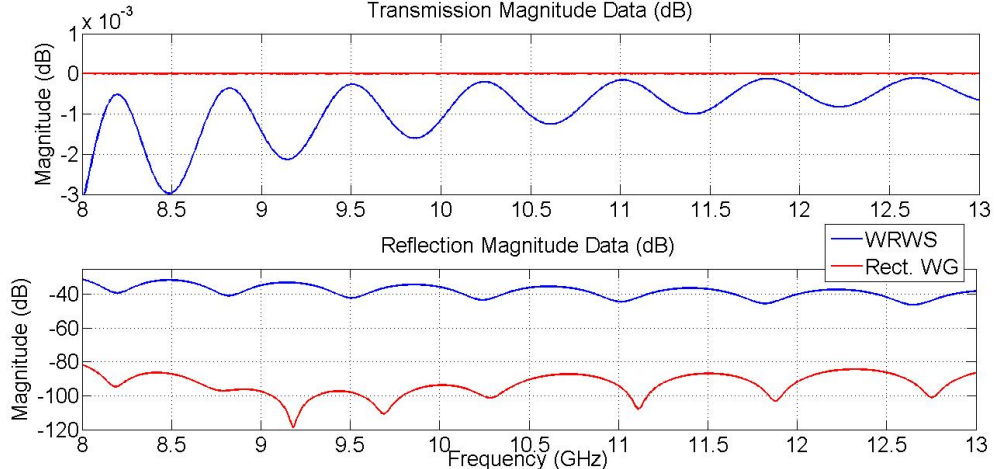


Figure 9. Comparison of Magnitude S-parameter Data: Top-Transmission, Bottom-Reflection

WRWS transition's taper produces a magnitude response that is equivalent to a series of waveguide apertures that have capacitive equivalent circuits [13]. The capacitance of the guide change in value as the aperture size changes over the length of the guide. This causes the “scalloping” in both the transmitted and reflected magnitude data in Figure 9. The differences in systematic responses between the two waveguides, show that the guiding structure contributes a systematic response to a material measurement. Removing this contribution, so it does not contaminate the material measurement, requires a calibration technique. A TRL calibration (discussed in Chapter 4) is employed in both simulation and measurement to account for the systematic responses of the WRWS and Rectangular Waveguide.

It is important to note that there are operational frequency limitations imposed by the geometry change from rectangular to square. A rectangular waveguide cut-off frequency at each mode is driven by the constraint equation and the material present in the waveguide. Assuming a free space filled waveguide the cut-off frequencies for each mode can be identified in [11] by

$$f_c = \frac{1}{2\pi\sqrt{\epsilon_0\mu_0}} \sqrt{\left(\frac{m\pi}{a}\right)^2 + \left(\frac{n\pi}{b}\right)^2} \quad (3.23)$$

where a and b are different dimensions and the modes are TE_{mn} . A rectangular waveguide has cut-off frequencies for the following modes as shown in the picture in Figure 10 (Top Drawing) while a square waveguide exhibits the modal cut-off

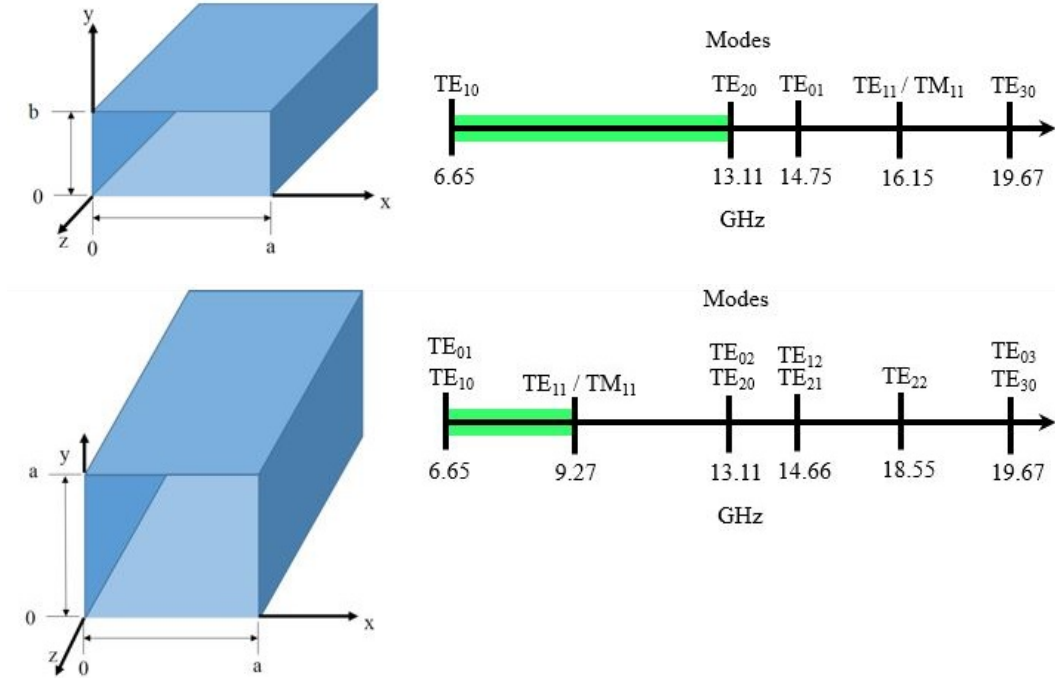


Figure 10. Comparison of Modes Propagated versus Frequency: Top: Rectangular Waveguide, Bottom: Square Waveguide

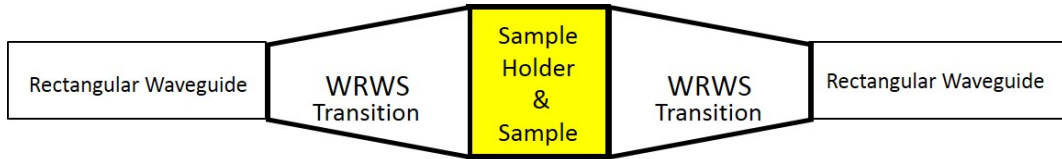


Figure 11. Waveguide arrangement

frequencies, shown in Figure 10 (Bottom Drawing). The square waveguide supports modal excitation and propagation above TE_{10} at lower frequencies than a rectangular waveguide. Having higher order modes at lower frequencies reduce the operational

bandwidth upon which materials can be characterized in closed form. Correcting the bandwidth reduction problem requires a gradual WRWS transition and a length of rectangular waveguide be installed on both sides of the WRWS setup as shown in Figure 11, to insure that the TE_{01} and TE_{11} modes are suppressed. This allows for material characterization to be performed using the WRWS over the full extent of X-band without exciting the higher order modes. The operational bandwidth can be extended higher in frequency if the TE_{20} is suppressed. A discussion of this observation is made in [14], and accomplished by exciting the waveguide with a symmetric feed. This symmetric feed configuration is determined by the type of coax to waveguide adapter used in the measurement set up.

3.3 Inverse Problem: Biaxial Parameter Extraction

This section provides the analysis of a y-invariant rectangular waveguide that has only a local section uniformly filled (thus only a TE_{10} mode is present) with a biaxial anisotropic material, as shown in Figure 12. This is different from the previous waveguide field analysis because there are now three regions and two interfaces (similar to the TEM analysis in Chapter 2). Once again, this development is also featured in the conference paper [8], which was developed in conjunction with the development of this thesis. These three regions have transmitted and reflected waves which are described below. Region 1 is described by the following transverse forward and reverse traveling waves:

$$\vec{E}_{t1} = a_1^+ \vec{e}_{m0} e^{-j\tilde{k}_z z} + a_1^- \vec{e}_{m0} e^{j\tilde{k}_z z}, \quad (3.24)$$

$$\vec{H}_{t1} = a_1^+ \tilde{\vec{h}}_{m0} e^{-j\tilde{k}_z z} - a_1^- \tilde{\vec{h}}_{m0} e^{j\tilde{k}_z z}. \quad (3.25)$$

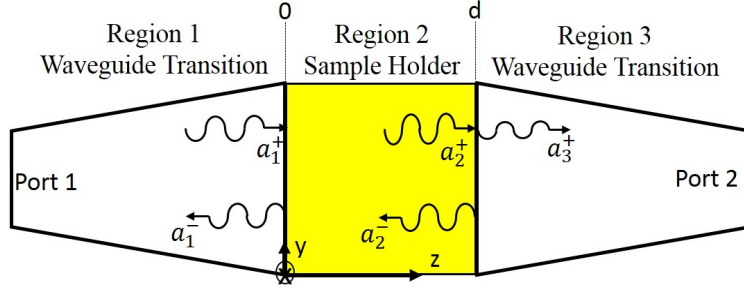


Figure 12. Sample filled section of waveguide

Region 2 by these forward and reverse traveling waves:

$$\vec{E}_{t2} = a_2^+ \vec{e}_{m0} e^{-jk_z z} + a_2^- \vec{e}_{m0} e^{jk_z z}, \quad (3.26)$$

$$\vec{H}_{t2} = a_2^+ \vec{h}_{m0} e^{-jk_z z} - a_2^- \vec{h}_{m0} e^{jk_z z}. \quad (3.27)$$

Region 3 has only the forward traveling wave:

$$\vec{E}_3 = a_3^+ \vec{e}_{m0} e^{-j\tilde{k}_z(z-d)}, \quad \vec{H}_3 = a_3^+ \tilde{\vec{h}}_{m0} e^{-j\tilde{k}_z(z-d)}. \quad (3.28)$$

The constraint equation for the free space regions is developed in [11] and is used in regions 1 and 3 of Figure 12 and has the constraint equation $\tilde{k}_z = \sqrt{k_0^2 - k_x^2}$, where $k_0 = \frac{\omega}{c}$, $k_x = \frac{m\pi}{a}$ and the wave impedance is $\tilde{Z}_{TE} = \frac{\omega\mu_0}{\tilde{k}_z} = Z_0$. By enforcing the continuity of tangential \vec{E} and \vec{H} in the WRWS system the expected relations for a biaxial anisotropic sample in a waveguide are obtained. These expected relations are familiar, because these are the closed form representations that allow for a NRW extraction process [1],[2]:

$$S_{11} = \Gamma = \frac{R(1 - P^2)}{1 - R^2P^2}, \quad S_{21} = T = \frac{P(1 - R^2)}{1 - R^2P^2} \quad (3.29)$$

Unlike the traditional NRW method, the eigenvalue relations are different because the sample is not isotropic. Therefore the biaxial anisotropic constraint equations (3.11) are used to define the R and P terms of the material parameter extraction equations (3.29). As shown in the conference paper [8] and also developed below, S-parameters are collected at each orientation of the sample and correspond to values R_n and P_n , where the subscript ‘n’ denotes the orientation of the sample as shown in Figure 13. The reflection at the interface between the waveguide transition and the sample is

$$R_n = \frac{Z_n - Z_0}{Z_n + Z_0} = \frac{\bar{Z}_n - 1}{\bar{Z}_n + 1}, \quad (3.30)$$

where

$$\bar{Z}_n = \frac{Z}{Z_0} = \frac{\omega\mu_x}{k_{zn}} \frac{k_{z0}}{\omega\mu_0} \quad (3.31)$$

and is rearranged to represent

$$\bar{Z}_n = \frac{1 + R_n}{1 - R_n}. \quad (3.32)$$

The transmission through the sample is described by

$$P_n = e^{-jk_{zn}d}, \quad (3.33)$$

and is rearranged to obtain

$$\frac{j \ln P_n}{d} = k_{zn}. \quad (3.34)$$

Once \bar{Z}_n and k_{zn} are obtained, the transverse permeability component can be determined from

$$\mu_{xn} = \frac{\bar{Z}_n k_{zn} \mu_0}{k_{z0}}. \quad (3.35)$$

Using the transverse permeability μ_{xn} , the transverse permittivity ϵ_{yn} can be solved

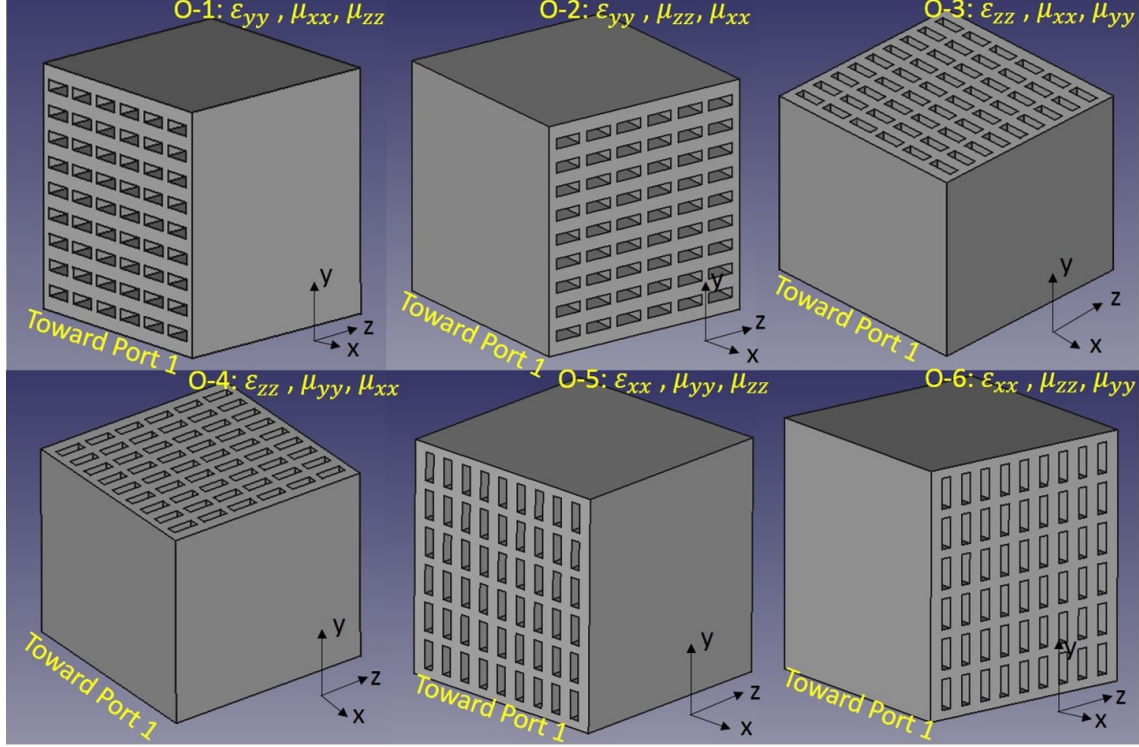


Figure 13. Unit Cell Cubic Sample

by rearranging (3.11) into the form

$$\epsilon_{yn} = \frac{k_{zn}^2 + \frac{\mu_{xn}}{\mu_z} k_x^2}{\omega^2 \mu_{xn}} \quad (3.36)$$

where μ_z is the permeability found from a separate transverse permeability measurement of the sample indexed in a different orientation.

Evaluating a cubic sample about the 6 orientations, as shown in Figure 13, will yield a pair of permittivity and permeability tensors in x, y and z. Permittivity in y is calculated from orientations 1 and 2; x from orientations 5 and 6; and z from orientations 3 and 4. Permeability in x is computed from orientations 2 and 6; y from orientations 4 and 5; and z from orientations 1 and 3 as shown in Figure 13.

Using the sample orientations of Figure 13 in conjunction with the equations (3.35) and (3.36) yields

$$\mu_1 = \frac{\bar{Z}_1 k_{z1} \mu_0}{k_{z0}}, \quad \epsilon_1 = \frac{k_{z1}^2 + \frac{\mu_1}{\mu_2} k_x^2}{\omega^2 \mu_1} \quad (3.37)$$

$$\mu_2 = \frac{\bar{Z}_2 k_{z2} \mu_0}{k_{z0}}, \quad \epsilon_2 = \frac{k_{z2}^2 + \frac{\mu_2}{\mu_1} k_x^2}{\omega^2 \mu_2} \quad (3.38)$$

$$\mu_3 = \frac{\bar{Z}_3 k_{z3} \mu_0}{k_{z0}}, \quad \epsilon_3 = \frac{k_{z3}^2 + \frac{\mu_3}{\mu_4} k_x^2}{\omega^2 \mu_3} \quad (3.39)$$

$$\mu_4 = \frac{\bar{Z}_4 k_{z4} \mu_0}{k_{z0}}, \quad \epsilon_4 = \frac{k_{z4}^2 + \frac{\mu_4}{\mu_3} k_x^2}{\omega^2 \mu_4} \quad (3.40)$$

$$\mu_5 = \frac{\bar{Z}_5 k_{z5} \mu_0}{k_{z0}}, \quad \epsilon_5 = \frac{k_{z5}^2 + \frac{\mu_5}{\mu_6} k_x^2}{\omega^2 \mu_5} \quad (3.41)$$

$$\mu_6 = \frac{\bar{Z}_6 k_{z6} \mu_0}{k_{z0}}, \quad \epsilon_6 = \frac{k_{z6}^2 + \frac{\mu_6}{\mu_5} k_x^2}{\omega^2 \mu_6} \quad (3.42)$$

Confirming the measurement capabilities of the WRWS system, permittivity comparisons are made between the Rectangular Waveguide measurements system and the WRWS system. Closed form NRW measurements of an isotropic cubic UV cured polymer sample show that resonances occur as seen in Figure 14. These resonances are due to the sample being electrically thick. The resonances occur at n integer multiples of $\frac{\lambda}{2}$ at a given sample thickness d within the material sample. Resonant frequency values can be calculated by establishing that a resonance is set up when $k_{zn} = \frac{\pi n}{d}$ and solving for ω . Converting from radial frequency to linear frequency:

$$f = \frac{\sqrt{\frac{(\frac{\pi n}{d})^2 + (\frac{\mu_x}{\mu_z} \frac{\pi}{a})^2}{\mu_0 \epsilon_0 \epsilon_y \mu_x}}}{2\pi}. \quad (3.43)$$

At 8.66 and 12.24 GHz resonances are calculated to occur within the sample, and is validated by the plot in Figure 14. A 1-D root search extraction code is developed using [4]. The root search code allows sample permittivities to be extracted from indi-

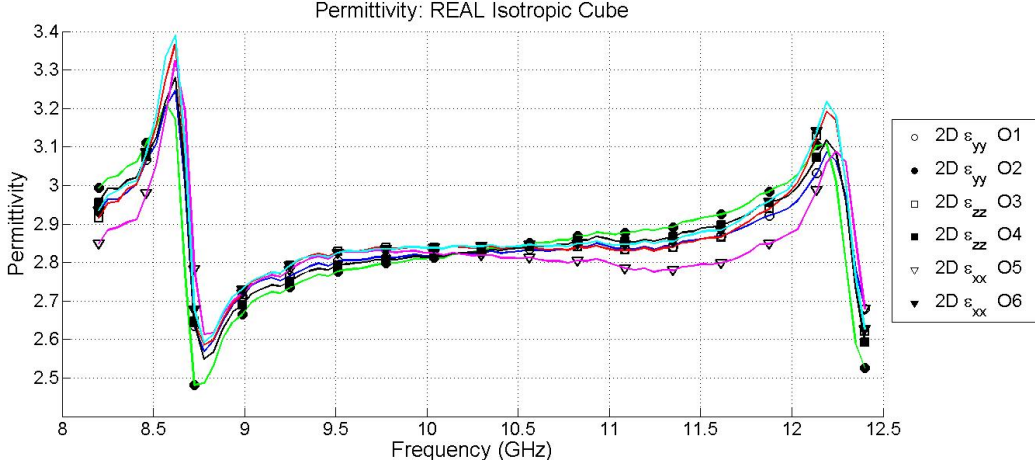


Figure 14. Closed form measurement with sample resonances at $\frac{n\lambda}{2}$

vidual S-parameters, and avoid the resonance issue, assuming that the permeability is known ($\mu = \mu_0$ in this case). A performance comparison measurement is made between the rectangular waveguide (RWG) measurement technique and the WRWS system. The RWG and WRWS sample holders are measured empty, to measure the air occupying the volume. This measurement eliminates the potential variability of the sample and has a expected relative permittivity of $\epsilon_r = 1$. The comparison shows excellent agreement between the RWG and WRWS measurement systems as seen in Figure 15. Based on the recommendations in [4] and observing the stability of the extracted root search results in Figure 15, the S_{21} data is used as the primary S-parameter data source for the 1-D root search material parameter extraction. A rectangular sample of UV cured polymer and a cube sample of UV cured polymer, shown in Figure 16 are developed to support the measurements. It is shown that the UV cured polymer materials measures at $\epsilon_r \approx 2.8655 - 0.04j$ at mid-band, as seen in Figure 17, and used as the permittivity value for the UV cured polymer in all prediction models.

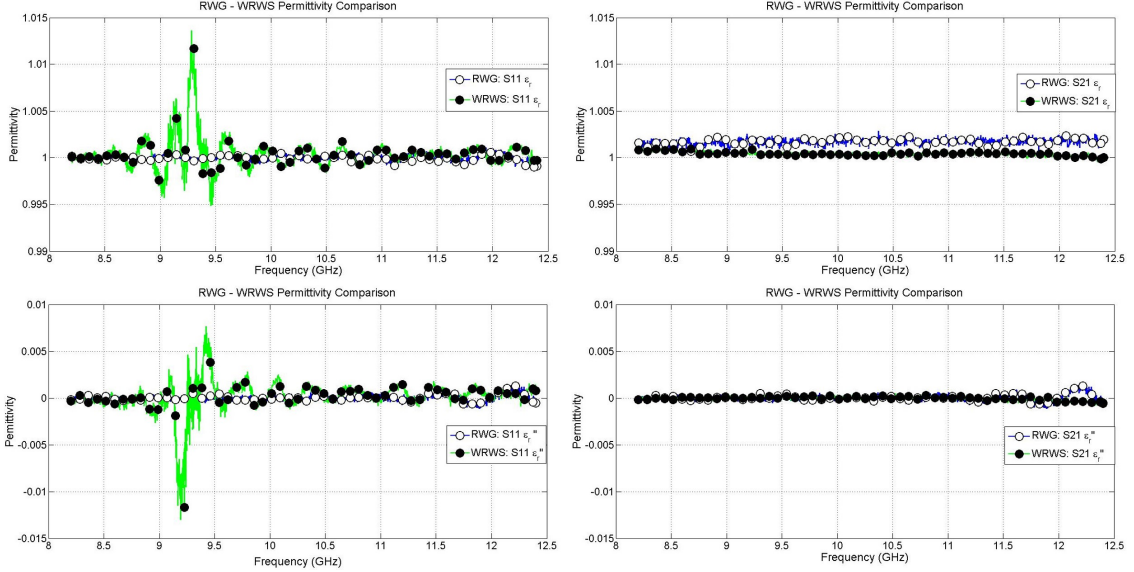


Figure 15. Comparison of RWG and WRWS with Free-space filled sample holder: Left: S_{11} , Right: S_{21}

3.4 Summary

The measurement comparisons between isotropic sample shows that the developed closed form biaxial anisotropic NRW-type formulation for material parameter extraction yields identical results to the legacy RWG method. Additionally, it is also shown that higher order modes are not excited by the WRWS transitions. Successful isotropic testing of the WRWS measurement methodology provides confidence in anisotropic sample development, prediction and testing.

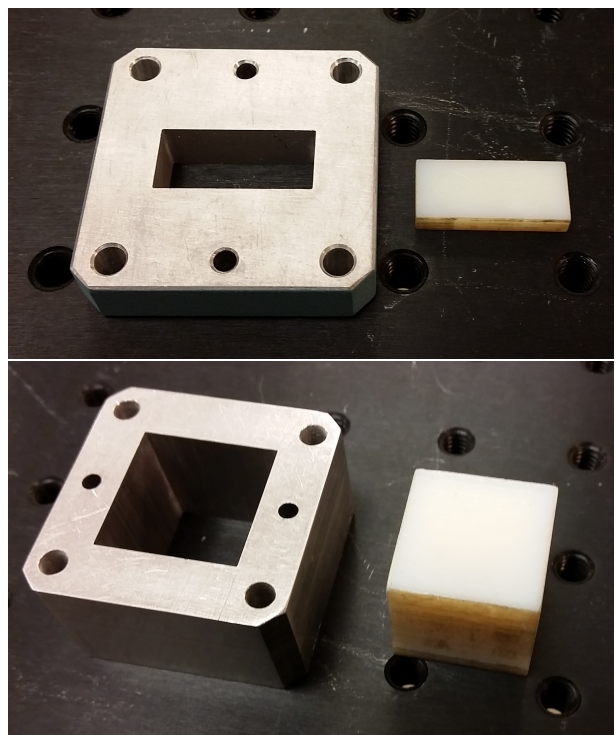


Figure 16. Isotropic UV cured RWG (Top) and WRWS (Bottom) polymer samples and sample holders

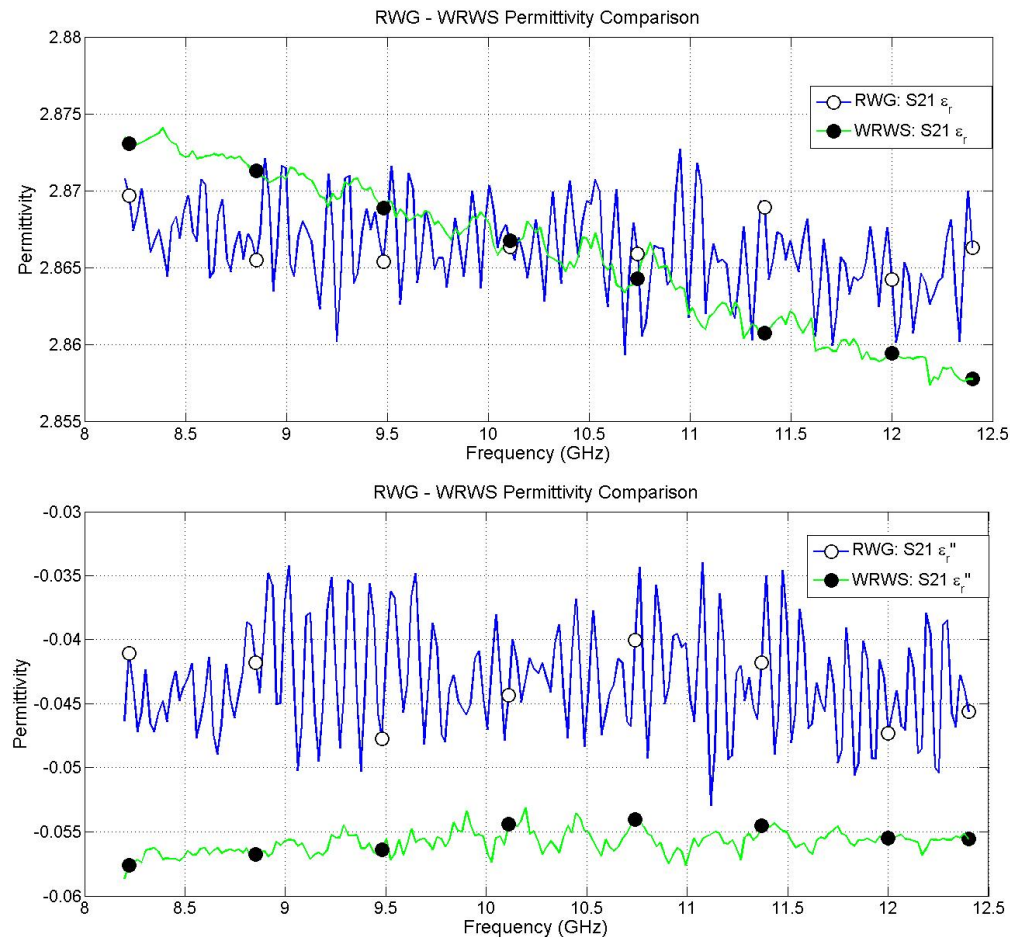


Figure 17. Isotropic UV cured RWG and WRWS polymer sample comparison

IV. Sample Development

Testing the WRWS system's anisotropic measurement abilities requires that a sample be constructed which possesses biaxial anisotropic constitutive parameters. A sample geometry is designed using crystallographic symmetry and manufactured using a UV cured 3-D polymer printer. Two prediction capabilities are devised to support the sample design: A lumped element equivalent circuit approach and a CEM Frequency Domain model in CST Microwave Studio®.

4.1 Biaxial Sample Development

Dmitriev [10] shows that different electromagnetic performance capabilities can be designed using crystallographic symmetry. 3-D geometric shapes exhibit various forms of rotational and axial symmetry. Curie's and Neumann's Principles [10] provide the mathematical development for combining shapes and symmetries. New, more complex shapes can be made from combinations of different primitive crystals.

The WRWS system accommodates cubic samples, which imposes the requirement that the parent structure must be a cube. Review of Collin's paper [9] shows a potential arrangement for rectangular inclusions yielding biaxial performance. These rectangular inclusions are orthorhombic unit cells. Arranging orthorhombic crystals inside a cubic structure suggests that the arrangement be orthorhombic as well, maximizing the utilization of cubic volume. Showing the mathematical development for Collin's design, Dmitriev's crystal groups and the International Tables for Crystallography [15],[16] notation provide the crystallographic design and demonstrates that the resulting geometry yields an electromagnetic biaxial anisotropic sample design, as seen in Figure 18. Curie's principle

$$\overleftrightarrow{\epsilon} = [\text{inclusion symmetry}] \cap [\text{arrangement symmetry}] \cap [\text{cube symmetry}] \quad (4.44)$$

Biaxial Sample Development

Crystallographic Sample Design

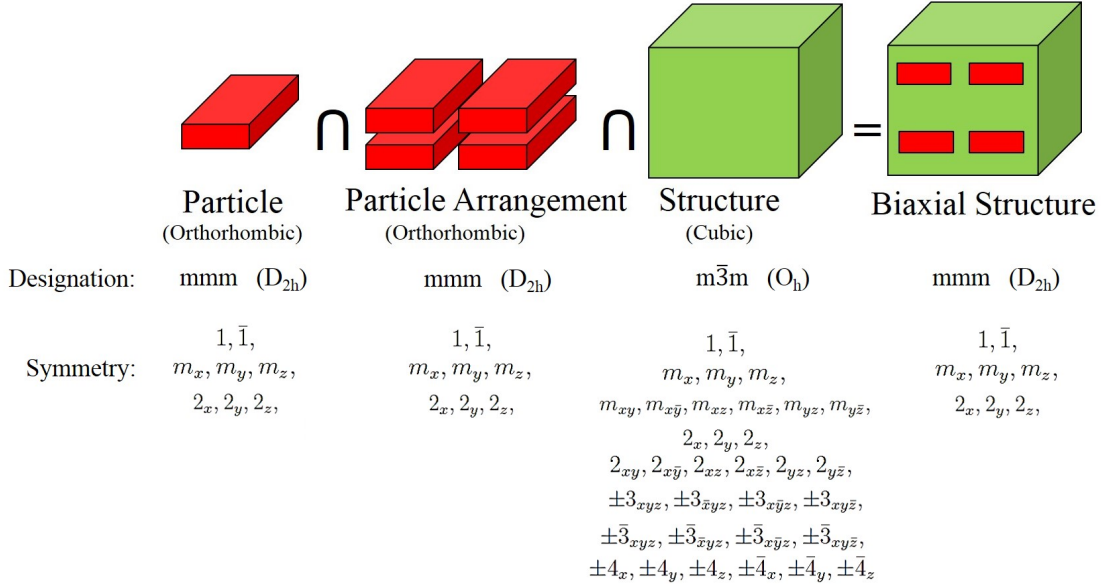


Figure 18. Demonstrates Curie's Principle and show the symmetry that exists in each structure.

shows that the resulting structure has inversion symmetry ($1, \bar{1}$), mirror symmetry and two-fold rotational symmetry in the x, y and z axes: (m_x, m_y, m_z) and ($2_x, 2_y, 2_z$), respectively. Since the resulting symmetry describes an orthorhombic structure (International Crystallographic notation: mmm), the orthorhombic generating functions [10]:

$$m_x = \begin{bmatrix} -1 & 0 & 0 \\ 0 & 1 & 0 \\ 0 & 0 & 1 \end{bmatrix} \quad m_y = \begin{bmatrix} 1 & 0 & 0 \\ 0 & -1 & 0 \\ 0 & 0 & 1 \end{bmatrix} \quad m_z = \begin{bmatrix} 1 & 0 & 0 \\ 0 & 1 & 0 \\ 0 & 0 & -1 \end{bmatrix} \quad (4.45)$$

are used to demonstrate the geometry's biaxial anisotropy. Dielectric biaxial anisotropy

is demonstrated by applying Neumann's principle,

$$\overset{\leftrightarrow}{\epsilon} = \overset{\leftrightarrow}{T} \cdot \overset{\leftrightarrow}{\epsilon} \cdot \overset{\leftrightarrow}{T}^T \quad (4.46)$$

to the full permittivity tensor $\overset{\leftrightarrow}{\epsilon}$. Simplifying calculations and easing comparison of the tensor elements, Neumann's principle is re-arranged to

$$\overset{\leftrightarrow}{T} \cdot \overset{\leftrightarrow}{\epsilon} = \overset{\leftrightarrow}{\epsilon} \cdot \overset{\leftrightarrow}{T}. \quad (4.47)$$

Since dielectric materials are only utilized in a physical sample, only the permittivity tensor is evaluated. Applying the m_x generating function to the full permittivity tensor

$$\begin{bmatrix} -1 & 0 & 0 \\ 0 & 1 & 0 \\ 0 & 0 & 1 \end{bmatrix} \cdot \begin{bmatrix} \epsilon_{xx} & \epsilon_{xy} & \epsilon_{xz} \\ \epsilon_{yx} & \epsilon_{yy} & \epsilon_{yz} \\ \epsilon_{zx} & \epsilon_{zy} & \epsilon_{zz} \end{bmatrix} = \begin{bmatrix} \epsilon_{xx} & \epsilon_{xy} & \epsilon_{xz} \\ \epsilon_{yx} & \epsilon_{yy} & \epsilon_{yz} \\ \epsilon_{zx} & \epsilon_{zy} & \epsilon_{zz} \end{bmatrix} \cdot \begin{bmatrix} -1 & 0 & 0 \\ 0 & 1 & 0 \\ 0 & 0 & 1 \end{bmatrix} \quad (4.48)$$

where

$$\begin{bmatrix} -\epsilon_{xx} & -\epsilon_{xy} & -\epsilon_{xz} \\ \epsilon_{yx} & \epsilon_{yy} & \epsilon_{yz} \\ \epsilon_{zx} & \epsilon_{zy} & \epsilon_{zz} \end{bmatrix} = \begin{bmatrix} -\epsilon_{xx} & \epsilon_{xy} & \epsilon_{xz} \\ -\epsilon_{yx} & \epsilon_{yy} & \epsilon_{yz} \\ -\epsilon_{zx} & \epsilon_{zy} & \epsilon_{zz} \end{bmatrix}. \quad (4.49)$$

Equating the left and right hand sides of (4.49) leads to the result

$$\overset{\leftrightarrow}{\epsilon} = \begin{bmatrix} \epsilon_{xx} & 0 & 0 \\ 0 & \epsilon_{yy} & \epsilon_{yz} \\ 0 & \epsilon_{zy} & \epsilon_{zz} \end{bmatrix}. \quad (4.50)$$

Applying m_y to the solution (4.50):

$$\begin{bmatrix} 1 & 0 & 0 \\ 0 & -1 & 0 \\ 0 & 0 & 1 \end{bmatrix} \cdot \begin{bmatrix} \epsilon_{xx} & 0 & 0 \\ 0 & \epsilon_{yy} & \epsilon_{yz} \\ 0 & \epsilon_{zy} & \epsilon_{zz} \end{bmatrix} = \begin{bmatrix} \epsilon_{xx} & 0 & 0 \\ 0 & \epsilon_{yy} & \epsilon_{yz} \\ 0 & \epsilon_{zy} & \epsilon_{zz} \end{bmatrix} \cdot \begin{bmatrix} 1 & 0 & 0 \\ 0 & -1 & 0 \\ 0 & 0 & 1 \end{bmatrix} \quad (4.51)$$

where

$$\begin{bmatrix} \epsilon_{xx} & 0 & 0 \\ 0 & -\epsilon_{yy} & -\epsilon_{yz} \\ 0 & \epsilon_{zy} & \epsilon_{zz} \end{bmatrix} = \begin{bmatrix} \epsilon_{xx} & 0 & 0 \\ 0 & -\epsilon_{yy} & \epsilon_{yz} \\ 0 & -\epsilon_{zy} & \epsilon_{zz} \end{bmatrix}. \quad (4.52)$$

Equating the left and right hand sides of (4.52) leads to the result

$$\overset{\leftrightarrow}{\epsilon} = \begin{bmatrix} \epsilon_{xx} & 0 & 0 \\ 0 & \epsilon_{yy} & 0 \\ 0 & 0 & \epsilon_{zz} \end{bmatrix}. \quad (4.53)$$

Applying the remaining generating function m_z :

$$\begin{bmatrix} 1 & 0 & 0 \\ 0 & 1 & 0 \\ 0 & 0 & -1 \end{bmatrix} \cdot \begin{bmatrix} \epsilon_{xx} & 0 & 0 \\ 0 & \epsilon_{yy} & 0 \\ 0 & 0 & \epsilon_{zz} \end{bmatrix} = \begin{bmatrix} \epsilon_{xx} & 0 & 0 \\ 0 & \epsilon_{yy} & 0 \\ 0 & 0 & \epsilon_{zz} \end{bmatrix} \cdot \begin{bmatrix} 1 & 0 & 0 \\ 0 & 1 & 0 \\ 0 & 0 & -1 \end{bmatrix} \quad (4.54)$$

where

$$\begin{bmatrix} \epsilon_{xx} & 0 & 0 \\ 0 & \epsilon_{yy} & 0 \\ 0 & 0 & -\epsilon_{zz} \end{bmatrix} = \begin{bmatrix} \epsilon_{xx} & 0 & 0 \\ 0 & \epsilon_{yy} & 0 \\ 0 & 0 & -\epsilon_{zz} \end{bmatrix}. \quad (4.55)$$

Equating the left and right hand sides of (4.55) does not reveal any additional information regarding the tensor structure. The resulting permittivity tensor (4.53) demonstrates that the biaxial structure featured in Figure 18 has three unique di-

agonal elements, assuming tensor alignment along the optic axis. Crystallographic symmetry provides structural guidance on how to design a biaxial anisotropic sample, but does not provide information for specific tensor element values or exact sample dimensions.

4.2 Lumped Element Prediction of Biaxial Anisotropic Constitutive Parameters

Prediction of biaxial anisotropic constitutive parameters is important to the design and synthesis of a testable material. Additionally, prediction methods provide comparison data, which can be compared to measured experimental results. A lumped element equivalent circuit prediction method is used to provide estimations on biaxial anisotropic tensor values. Biaxial sample design factors include the number of cells (inclusions or occlusions), cell dimensions and the materials used. Electric Capacitance [17] and Magnetic Inductance [18] equations,

$$C = \frac{\epsilon_r \epsilon_0 S}{d}, \quad L = \frac{d}{\mu_r \mu_0 S}, \quad (4.56)$$

where S is the surface area and d is the gap distance for the representative equivalent circuit component, serve as models and describe each piece of a sample, as seen in Figure 19. The lumped element model relates the sample's structural dimensions and materials to a circuit equivalent network which provides an approximation of the sample's permittivity or permeability. Depending on how the sample is discretized into circuit components and which sample measurement orientation is evaluated, different sample constitutive tensor element values are obtained.

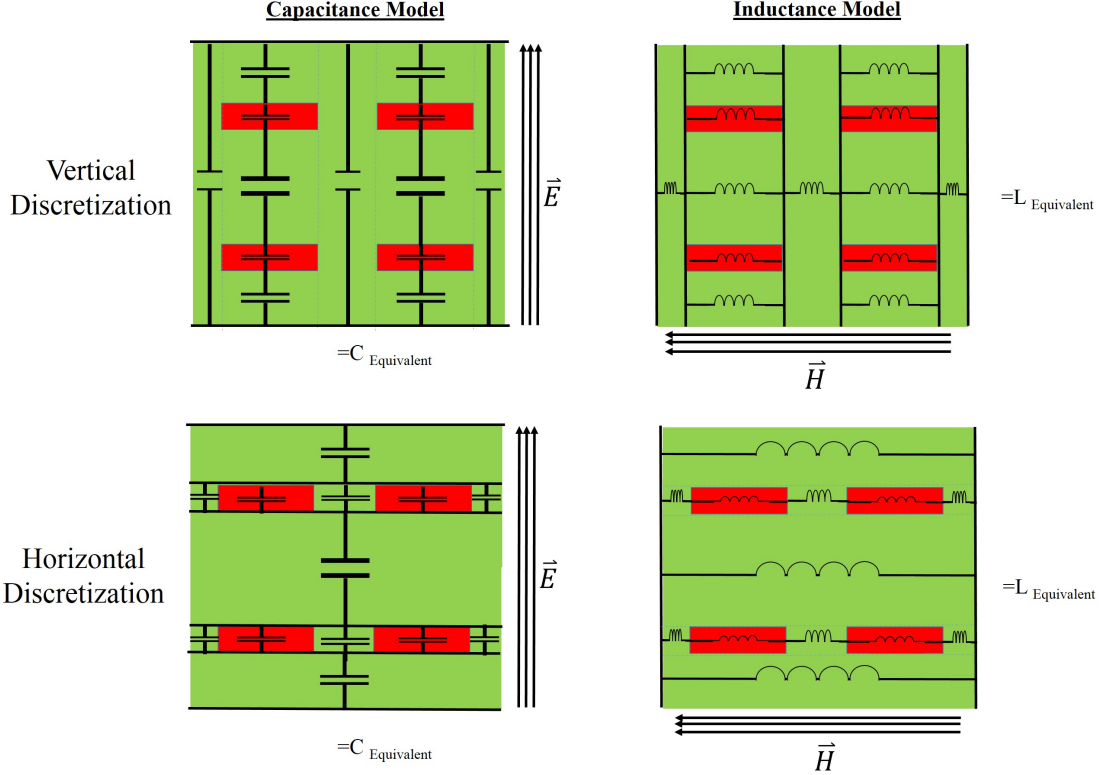


Figure 19. Equivalent Lumped Element Prediction Technique: Left: Permittivity, Right: Permeability

Sample Analysis Methodology.

A representative cube sample is decomposed into capacitive and inductive pieces to predict its relative permittivity and permeability, shown in Figure 19. Using Figure 13 as a guide, equivalent circuit models are made for each orientation. Each sample orientation yields two unique equivalent circuit arrangements, as shown in Figure 19. The horizontal and vertical equivalent circuits yield different results from each other because of how the series and parallel circuits are arranged. The horizontal capacitor circuit arrangement and vertical inductor circuit arrangement yield a higher permittivity and permeability values than the vertical capacitor and horizontal inductor arrangements. [17] provides discussion and a comparison on horizontal and vertical sample capacitive discretization, and demonstrates horizontal equivalent

circuit permittivities are larger than the vertical. The difference between the two discretization schemes is related to the volume fraction of the inclusions to the host material. Volume fractions which are very large or very small, will yield identical values for both horizontal or vertical discretization, because the sample will consist almost entirely of either the host material or the inclusion material. Certain sample orientations do not possess both equivalent circuit discretization models because the inclusion orientation prevents discretization into physically analogous capacitor or inductor networks.

The equations below describe the permittivity and permeability of a cubic sample with rectangular inclusions or occlusions. Variables in these equations are: x = number of cell columns, y = number of cell rows, l, w, h = sample edge length, h_c = cell height, w_c = cell width, l_c = cell length. Material definitions are: ϵ_m permittivity of the sample structure, ϵ_a permittivity of the cell inclusion/occlusion, μ_m permeability of the sample structure, μ_a permeability of the cell inclusion/occlusion. The analysis equations provide predictions on a given geometry made from known materials.

Vertical Orientation 1 and 2 permittivity:

$$\epsilon_{v1,v2} = \frac{h \left(\frac{\epsilon_m l (w - w_c x)}{l_c} + \frac{\epsilon_a \epsilon_m l_c w_c x \epsilon_0}{\epsilon_a h - \epsilon_a h_c y + \epsilon_m h_c y} \right)}{l w} \quad (4.57)$$

Horizontal Orientation 1 and 2 permittivity:

$$\epsilon_{h1,h2} = \frac{h}{l w \left(\frac{h - h_c y}{\epsilon_m l_c l} + \frac{h_c y}{l_c (\epsilon_m w + \epsilon_a w_c x - \epsilon_m w_c x)} \right)} \quad (4.58)$$

Vertical Orientation 3 and 4 permittivity:

$$\epsilon_{v3,v4} = \frac{h (\epsilon_m w^2 - \epsilon_m w_c x w + \epsilon_m w_c x h + \epsilon_a h_c w_c x y - \epsilon_m h_c w_c x y)}{l_c l w} \quad (4.59)$$

Horizontal Orientation 3 and 4 permittivity: Does not exist.

Vertical Orientation 5 and 6 permittivity:

$$\epsilon_{v5,v6} = \frac{h \left(\frac{\epsilon_m l (h - h_c y)}{l_c} + \frac{\epsilon_a \epsilon_m h_c l_c y}{\epsilon_a w - \epsilon_a w_c x + \epsilon_m w_c x} \right)}{l w} \quad (4.60)$$

Horizontal Orientation 5 and 6 permittivity:

$$\epsilon_{h5,h6} = \frac{h}{l w \left(\frac{w - w_c x}{\epsilon_m l_c l} + \frac{w_c x}{l_c (\epsilon_m h + \epsilon_a h_c y - \epsilon_m h_c y)} \right)} \quad (4.61)$$

Vertical Orientation 1 and 3 permeability:

$$\mu_{v1,v3} = \frac{1}{l \left(\frac{w - w_c x}{\mu_m l^2} + \frac{w_c x}{l (\mu_m h + \mu_a h_c y - \mu_m h_c y)} \right)} \quad (4.62)$$

Horizontal Orientation 1 and 3 permeability:

$$\mu_{h1,h3} = \frac{\mu_m (h - h_c y) + \frac{\mu_a \mu_m h_c l y}{\mu_a w - \mu_a w_c x + \mu_m w_c x}}{l} \quad (4.63)$$

Vertical Orientation 2 and 6 permeability: Does not exist.

Horizontal Orientation 2 and 6 permeability:

$$\mu_{h2,h6} = \frac{\mu_m (h - h_c y) + \frac{\mu_m h_c y (w - w_c x)}{l} + \frac{\mu_a h_c w_c x y}{l}}{l} \quad (4.64)$$

Vertical Orientation 4 and 5 permeability:

$$\mu_{v4,v5} = \frac{1}{l \left(\frac{h - h_c y}{\mu_m l^2} + \frac{h_c y}{l(\mu_m w + \mu_a w_c x - \mu_m w_c x)} \right)} \quad (4.65)$$

Horizontal Orientation 4 and 5 permeability:

$$\mu_{h4,h5} = \frac{\mu_m (w - w_c x) + \frac{\mu_a \mu_m w_c x l}{\mu_a h - \mu_a h_c y + \mu_m h_c y}}{l} \quad (4.66)$$

Sample Synthesis Methodology.

Aiding the design of a test sample, cubic biaxial anisotropic sample synthesis equations are developed from the vertical transverse (ϵ_x, ϵ_y) permittivity analysis equations (4.57) and (4.60). Synthesis equations allow a user to specify materials, the transverse permittivity values, sample edge length (because the sample is a cube and inclusions/occlusion are equivalent to the edge length), and the number of sample cell rows and columns. An analysis equation (4.59) for the longitudinal value ϵ_z is also employed in the synthesis code to indicate the longitudinal permittivity given the user inputs. The synthesis equations:

$$w_c = -\frac{l (\epsilon_m - \epsilon_{yy}) (\epsilon_a l - \epsilon_a h_c y + \epsilon_m h_c y)}{\epsilon_m h_c x y (\epsilon_a - \epsilon_m)} \quad (4.67)$$

and

$$h_c = -\frac{l (\epsilon_m - \epsilon_{xx}) (\epsilon_a l - \epsilon_a w_c x + \epsilon_m w_c x)}{\epsilon_m w_c x y (\epsilon_a - \epsilon_m)} \quad (4.68)$$

outputs describe the cell (inclusion/occlusion) dimensions. The output dimensions of the synthesis equations are then used to construct the sample in a CAD utility. The resulting CAD file is then printed on a UV cured polymer 3-D printer.

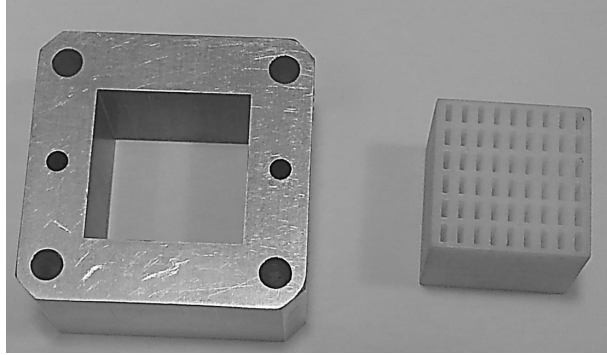


Figure 20. Sample and Sample Holder

MATLAB® code is written to utilize both the analysis and synthesis equations. The synthesis code is used to generate a cubic sample with air occlusions because the 3-D printer can only print one material. The goal is to have the sample's relative permittivity values spread as far apart as possible to maximize biaxial anisotropic performance. Tensor element values are, however, constrained by the sample's parent materials, air $\epsilon_r = 1$ and the UV cured polymer $\epsilon_r \approx 2.86$, which establish a lower and upper bound to the permittivity. Sample design factors include: maintaining macroscopic EM averaging, sample robustness and ease of printing. Each of these factors create trade-space in the sample design. Multiple occlusions of small dimension should be used to maintain macroscopic EM, while fewer inclusions with larger cell dimensions provide for a more structurally robust sample, and is more easily printed. Accommodating these design factors and maximizing the spread in biaxial permittivity leads to the sample design featured in Figure 13, verified using the lumped element analysis code, printed on a UV cured 3-D polymer printer and

Table 1. Vertical Lumped Element Prediction

Orientation	Relative Permittivity
O1- ϵ_{yy} =	1.97
O2- ϵ_{yy} =	1.97
O3- ϵ_{zz} =	2.32
O4- ϵ_{zz} =	2.32
O5- ϵ_{xx} =	2.21
O6- ϵ_{xx} =	2.21

Table 2. Horizontal Lumped Element Prediction

Orientation	Relative Permittivity
O1- ϵ_{yy} =	2.10
O2- ϵ_{yy} =	2.10
O3- ϵ_{zz} =	–
O4- ϵ_{zz} =	–
O5- ϵ_{xx} =	2.28
O6- ϵ_{xx} =	2.28

is shown along side the WRWS cubic sample holder in Figure 20. The dimensions of the sample are 22.86 mm edge length with 54 uniformly spaced rectangular occlusions measuring 1 mm by 2.79 mm by 22.86 mm. The vertical and horizontal lumped element permittivity predictions for the sample in Figure 20 are shown in Table 1 and Table 2. Because the vertical lumped element prediction has more solutions, it is used for comparisons with the measured data and simulations.

4.3 Computational Electromagnetic Prediction of Biaxial Anisotropic Constitutive Parameters

A second, more rigorous approach to predicting material parameters is simulating the sample measurement. A CAD model of the WRWS measurement system and sample are constructed in CST Microwave Studio® and S-parameter data is generated using the General Purpose Frequency Domain Solver. The S-parameter data is then used in a MATLAB® based 1-D root search material parameter extraction

code to calculate permittivity values. The work presented here is also presented in a conference paper [12], in conjunction with the development of this thesis.

Initially, it was assumed that CST Microwave Studio® performed a calibrated de-embed on the material measurements. The material sample S-parameter data was de-embedded from the model using CST’s waveguide port “Distance to ref. plane” function [19]. However, it was observed, in simulations of known isotropic samples, extracted WRWS permittivity data exhibited significant non-physical frequency dispersion and did not agree with expected results. A diagnostic comparison was performed to evaluate the differences between a rectangular waveguide and WRWS material parameter extraction model in CST. A 4.13 mm thick sample of an isotropic Teflon® $\epsilon_r = 2.1 - j0.0004$ was simulated as seen in Figure 21 and results were com-

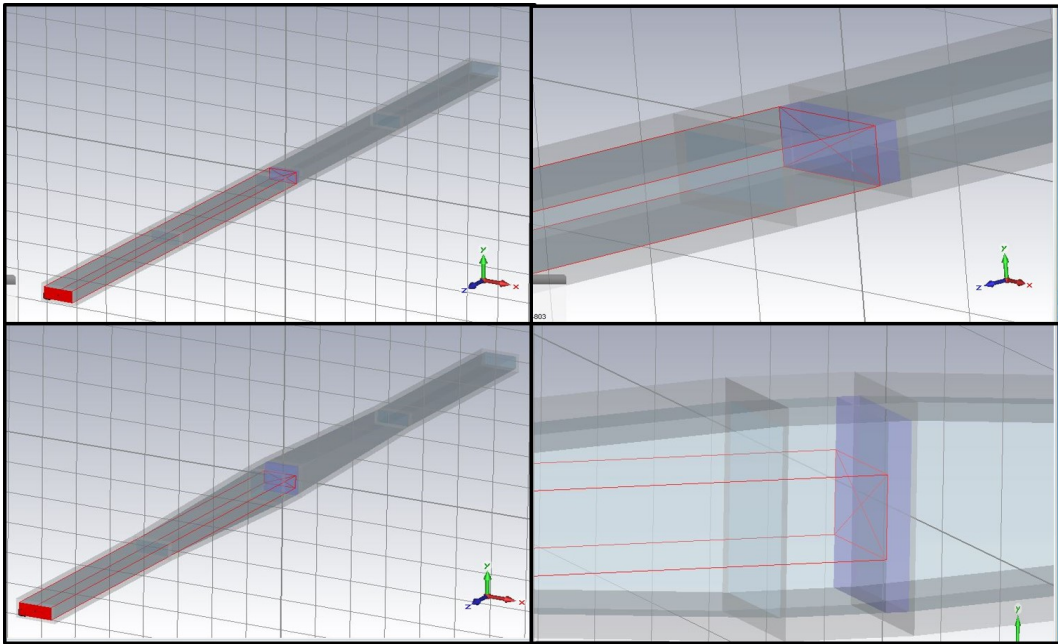


Figure 21. CST models of Rectangular Waveguide and WRWS system (Left), Teflon Samples installed (Right)

pared as seen in Figure 22. Both models utilize CST’s waveguide port “Distance to ref. plane” function to de-embed the S-parameters used to obtain the extracted permittivities. It is observed in Figure 22 that the results do not match the permittivity

of Teflon®, and the WRWS results exhibit significant ripple due to the reflections caused by the WRWS's tapered transitions, as observed in Figure 9. Additionally, the extracted rectangular waveguide permittivity data is not exactly the permittivity value of Teflon®. Based on the results, it is observed that systematic errors associated with the waveguide transitions distort the extracted WRWS permittivity results, similar to how the results would be effected in a poorly calibrated material sample measurement.

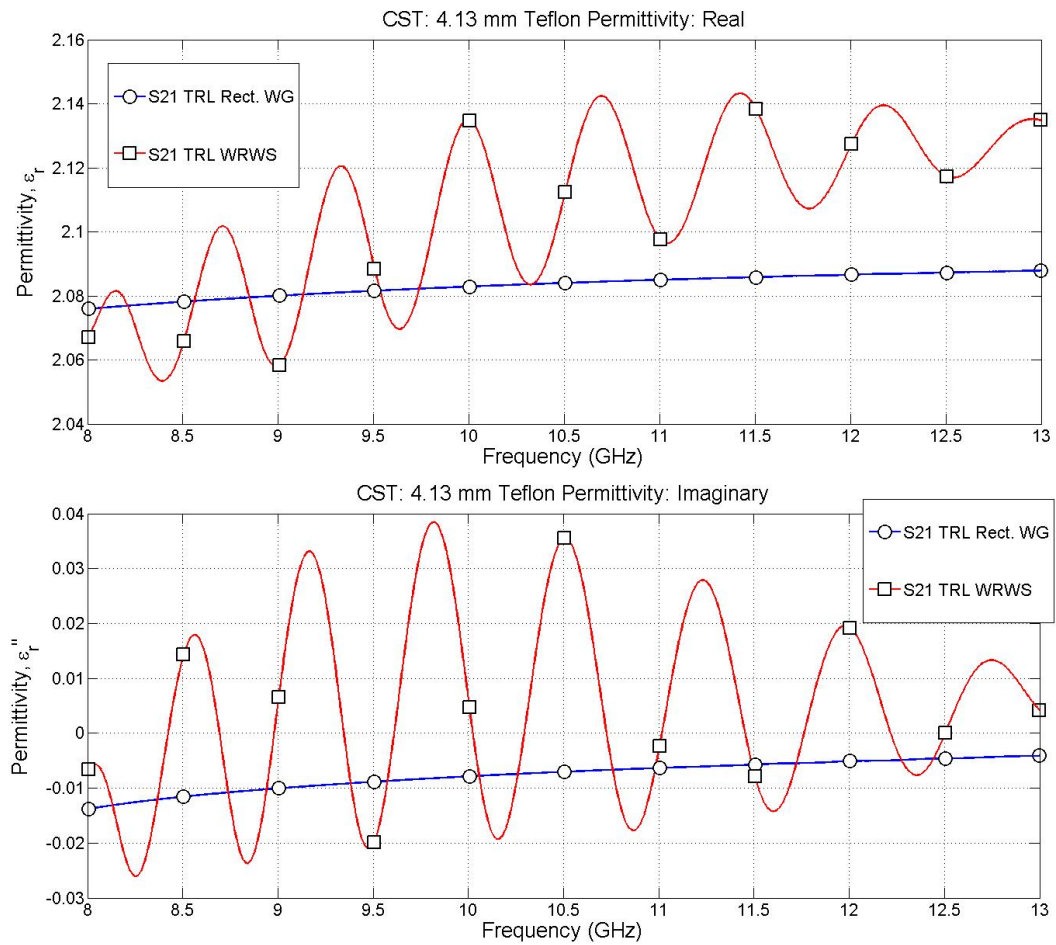


Figure 22. CST WRWS Teflon Sample De-embedded

Simulation calibration and sample measurement.

Material measurement/simulation performance can be degraded by systematic errors. These systematic errors include the reflections created by transitions or mismatches in waveguide, cable-connectors, or devices. Network Analyzers can compensate for these systematic errors by measuring their own receiver amplitude and phase sensitivities and using calibration routines to remove reflection/transmission errors. The Thru-Reflect-Line (TRL) calibration technique described by [20] removes these systematic errors and mathematically establishes reference planes at the location where the TRL calibration technique is applied. A TRL calibration process is employed in CST Microwave Studio® to remove systematic errors from both the WRWS and rectangular waveguide simulated measurements. Simulated CST data is then used in a TRL calibration code that was written in MATLAB® based on the work of [20] and Doug Rytting's technical papers [21], [22]. The TRL calibration code is used for both experimentally measured and simulated material measurements and is mathematically described below. Differences between simulated TRL calibrations and measured are in the assumption of a perfectly matched receivers in simulated data, and imperfect receivers, which are measured and accounted for in experimental data. Receiver accountability is described as:

$$s_{11} = \frac{s_{11}^{raw} - s_{12}^{raw} \frac{R2}{R1}}{1 - \frac{R2}{R1} \frac{R1}{R2}} \quad (4.69)$$

$$s_{12} = \frac{s_{12}^{raw} - s_{11}^{raw} \frac{R2}{R1}}{1 - \frac{R2}{R1} \frac{R1}{R2}} \quad (4.70)$$

$$s_{21} = \frac{s_{21}^{raw} - s_{22}^{raw} \frac{R1}{R2}}{1 - \frac{R1}{R2} \frac{R2}{R1}} \quad (4.71)$$

$$s_{22} = \frac{s_{22}^{raw} - s_{21}^{raw} \frac{R1}{R2}}{1 - \frac{R1}{R2} \frac{R2}{R1}} \quad (4.72)$$

where $\frac{R_1}{R_2}$ and $\frac{R_2}{R_1}$ are the port receiver ratios and may not be reciprocal or equivalent. S-parameter data denoted by “raw” is the data uncalibrated, un-ratioed data from the VNA. Four total measurements (Thru, Reflect, Line and Sample) are required to produce calibrated data as shown in Figure 23. Because of these four measurements, four separate CST simulations (one for each measurement: Thru, Reflect, Line and Sample) are made and 2-port S-parameter data is collected from each simulation.

Network Analysis T-parameters

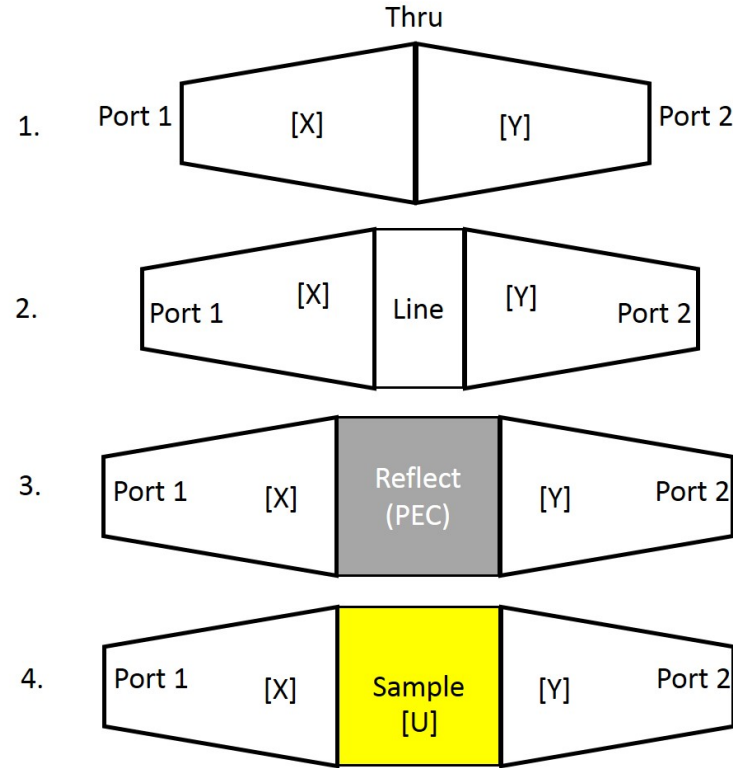


Figure 23. Graphical Depiction of TRL calibration

$$\begin{bmatrix} t_{11} & t_{12} \\ t_{21} & t_{22} \end{bmatrix} = \frac{1}{s_{21}} \begin{bmatrix} s_{21}s_{12} - s_{11}s_{22} & s_{11} \\ -s_{22} & 1 \end{bmatrix} \quad (4.73)$$

are used to describe each of the components in the waveguide measurement system and mathematically links them together. Doug Rytting in [22] demonstrates the de-

velopment and relationship between T-parameters and S-parameters. The $[X]$ matrix describes the left tapered transition; $[Y]$ matrix the right tapered transition and $[U]$ matrix the sample region or material under test (MUT) as depicted in Figure 23. The thru and line measurements are used to calculate the $[X]$ and $[Y]$ as represented by

$$[M] = [T]_{line}[T]_{thru}^{-1} \quad [N] = [T]_{thru}^{-1}[T]_{line}. \quad (4.74)$$

and

$$[M][X] = [X][T]_{line} \quad [Y][N] = [T]_{line}[Y]. \quad (4.75)$$

Solving for $[X]$ and $[Y]$ requires rearranging (4.75) and solving the system of equations. The rearranged equations are quadratic and each pose two potential solutions. The $[X]$ can be evaluated by

$$\frac{x_{11}}{x_{21}}, \frac{x_{12}}{x_{22}} = \frac{(m_{11} - m_{22}) \pm \sqrt{(m_{11} - m_{22})^2 + 4m_{21}m_{12}}}{2m_{21}} \quad (4.76)$$

and $[Y]$ by

$$\frac{y_{11}}{y_{12}}, \frac{y_{21}}{y_{22}} = \frac{(n_{11} - n_{22}) \pm \sqrt{(n_{11} - n_{22})^2 + 4n_{21}n_{12}}}{2n_{12}}. \quad (4.77)$$

The root choices are made as such, if $\left| \frac{x_{11}}{x_{21}} \right| > \left| \frac{x_{12}}{x_{22}} \right|$ then $a = \frac{x_{11}}{x_{21}}$ and $b = \frac{x_{12}}{x_{22}}$ else $b = \frac{x_{11}}{x_{21}}$ and $a = \frac{x_{12}}{x_{22}}$, $s_{11}^x = b$. Likewise, if $\left| \frac{y_{11}}{y_{12}} \right| > \left| \frac{y_{21}}{y_{22}} \right|$ then $c = \frac{y_{11}}{y_{12}}$ and $d = \frac{y_{21}}{y_{22}}$ else $d = \frac{y_{11}}{y_{12}}$ and $c = \frac{y_{21}}{y_{22}}$, $s_{22}^y = -d$. These root choices represent a decision as to which components are transmitted and reflected. The assumption is that in most passive devices the power reflected is less than the power transmitted. Isolating s_{22}^x utilizes the reflection measurement and requires a root choice be made as applied to the form

$$s_{22}^x = \pm \sqrt{\frac{(s_{11}^t - b)(s_{11}^r - b)(s_{22}^r + c)}{(s_{11}^t - a)(s_{11}^r - a)(s_{22}^r + d)}}. \quad (4.78)$$

The reflect measurement is also used to solve for the remaining terms of the equation

$$\Gamma^r = \frac{s_{11}^r - b}{s_{22}^x(s_{11}^r - a)}. \quad (4.79)$$

Because s_{22}^x has two possible roots, a root choice must be made to select the correct choice of s_{22}^x such that $\Gamma^r < 0$. Using the solutions and measurements provided above, the remaining equations are solved:

$$s_{11}^y = \frac{s_{11}^t - b}{s_{22}^x(s_{11}^r - a)} \quad (4.80)$$

$$s_{21}^x s_{21}^y = s_{21}^t (1 - s_{22}^x s_{11}^y) \quad (4.81)$$

$$s_{21}^y s_{12}^y = s_{11}^y (c - d) \quad (4.82)$$

$$s_{21}^x s_{12}^x = s_{11}^x (b - a) \quad (4.83)$$

Once all of the terms are solved then they can be applied to the $[X]$ and $[Y]$ matrices:

$$\begin{bmatrix} y_{11} & y_{12} \\ y_{21} & y_{22} \end{bmatrix} = \begin{bmatrix} s_{21}^y s_{12}^y - s_{11}^y s_{22}^y & s_{11}^y \\ -s_{22}^y & 1 \end{bmatrix} \quad (4.84)$$

$$\begin{bmatrix} x_{11} & x_{12} \\ x_{21} & x_{22} \end{bmatrix} = \begin{bmatrix} s_{21}^x s_{12}^x - s_{11}^x s_{22}^x & s_{11}^x \\ -s_{22}^x & 1 \end{bmatrix}. \quad (4.85)$$

The sample measurement data is then applied and the waveguide structure is mathematically removed by

$$[T]_u = s_{21}^x s_{21}^y [X]^{-1} [T]_{MUT} [Y]^{-1} \quad (4.86)$$

leaving the calibrated sample region data $[T]_u$. Converting $[T]_u$ back to S-parameters by

$$\begin{bmatrix} s_{11} & s_{12} \\ s_{21} & s_{22} \end{bmatrix} = \frac{1}{t_{22}} \begin{bmatrix} t_{21} & t_{11}t_{22} - t_{21}t_{12} \\ 1 & -t_{21} \end{bmatrix} \quad (4.87)$$

yields the calibrated S-parameter MUT data. If the sample is shorter than the distance between the two calibration reference planes as seen in Figure 24 a phase shift de-embed can be applied. These equations:

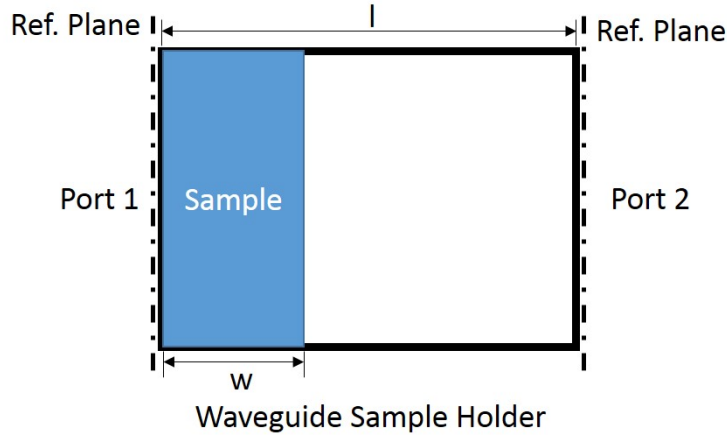


Figure 24. Sample Holder with dimensions

$$s_{11}^{samp.} = s_{11}^{ref.\,plane} e^{jk_z w} \quad (4.88)$$

$$s_{21}^{samp.} = s_{21}^{ref.\,plane} e^{jk_z (w-l)} \quad (4.89)$$

$$s_{12}^{samp.} = s_{12}^{ref.\,plane} e^{jk_z (w-l)} \quad (4.90)$$

$$s_{22}^{samp.} = s_{22}^{ref.\,plane} e^{2jk_z (w-l)} \quad (4.91)$$

moves the reference planes from the TRL calibrated reference plane to the sample-waveguide interface, where $k_z = \sqrt{k_0^2 - k_x^2}$ and the sample is placed as shown in the Figure 24. Using the TRL system calibration and the phase-shift de-embed yields

calibrated 2-port S-parameter data that is representative of the MUT. The calibrated MUT data is used to extract the sample's permittivity and permeability.

TRL Calibration Material Parameter Extraction.

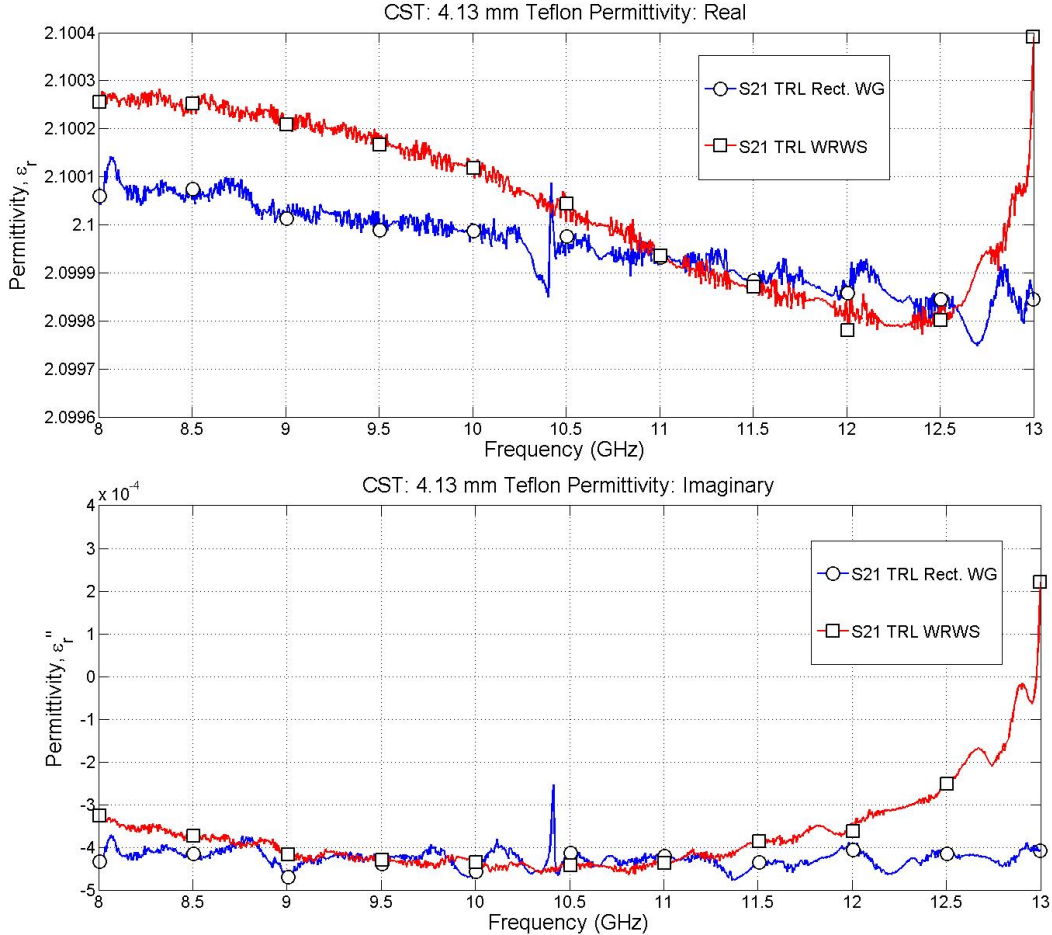


Figure 25. Rectangular Waveguide Teflon Sample TRL Calibrated Solution

The Teflon® measurement for the WRWS and rectangular waveguide are repeated employing the TRL calibration instead of the CST's "Distance to ref. plane" function. Obtaining all of the required data sets from CST to satisfy a TRL calibration, the simulated TRL calibration yields results that closely match the relative permittivity of Teflon®. Both the WRWS and rectangular waveguide yield almost the exact same results as seen in Figure 25. The calibration method removes the simulated systematic

errors and provides data that matches expected permittivity values.

4.4 Summary

Two prediction methods have been developed to support sample design and WRWS testing. The lumped element methodology provides permittivity and permeability tensor data and a sample design, while the CEM analysis in CST provides a simulated and calibrated measurement environment to evaluate the designed sample's performance. The simulated results can be compared with experimentally measured data to validate WRWS system performance and demonstrate the lumped element designed sample.

V. Results

Biaxial anisotropic material measurement test data is collected using the WRWS measurement system. The results are compared to the lumped element and CST Microwave Studio® predictions. A Monte Carlo uncertainty analysis is performed on the test data. Comparisons between prediction methods and physical experiments demonstrate WRWS measurement capability effectiveness.

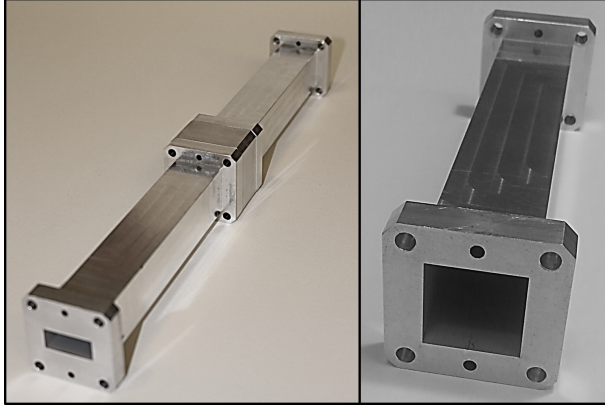


Figure 26. WRWS setup and view of square aperture

5.1 The WRWS system

The WRWS system is constructed from 6010 Aluminum stock. WRWS transitions, 0.9" cubic sample holder and 0.4" thick square aperture calibration line standard profiles, shown in Figures 26 and 27, are cut using a wire electrical discharge machine (EDM). The WRWS system uses the WR-90 precision alignment flange pattern for system assembly. WRWS transitions are 6 inches long and transition from the WR-90: 0.4" x 0.9" aperture to a square: 0.9" x 0.9" aperture, as seen in Figure 26. Each waveguide transition mounts to each side of the cubic sample holder or line standard, Figure 28.

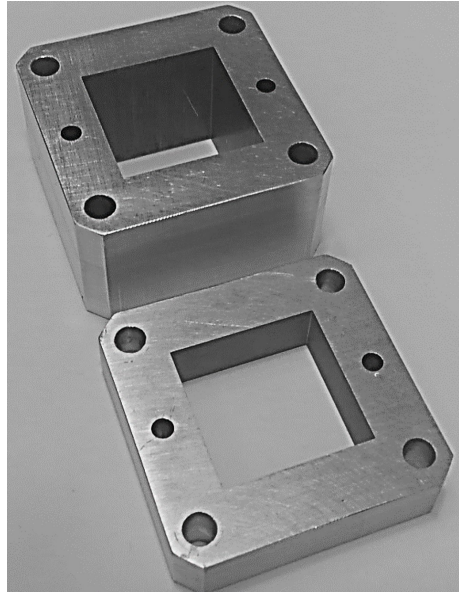


Figure 27. WRWS Cubic Sample Holder and Line Standard

5.2 Calibration and Measurement

A sample measurement begins with turning on the Vector Network Analyzer (VNA) and allowing it to warm up for approximately 1 hour prior to measurement. Network Analyzer settings are: 10 KHz intermediate frequency bandwidth (IFBW), 0 dBm power output, 1601 frequency points and frequency range from 8.2-12.4 GHz. The VNA is configured to provide two port S-parameter measurement data and receiver ratio port data. The receiver ratio data is required for TRL calibration of the physical measurement system. A visual inspection of all connectors, cables and adapters is performed to check for damage or debris. VNA test cables are attached to the VNA. X-band coax to waveguide adapters are attached to the test cables. Six inch lengths of X-band rectangular waveguide are attached to each coax to waveguide adapter. The WRWS transitions are then mounted to the rectangular waveguide, such that the rectangular waveguide flange matches the same size aperture of the WRWS transition. A table with waveguide support clamps is used to hold the rectangular waveguide in place as seen in Figure 29. All coaxial connections between the



Figure 28. WRWS showing waveguide transition on either side of the sample holder, line standard is placed left of sample holder

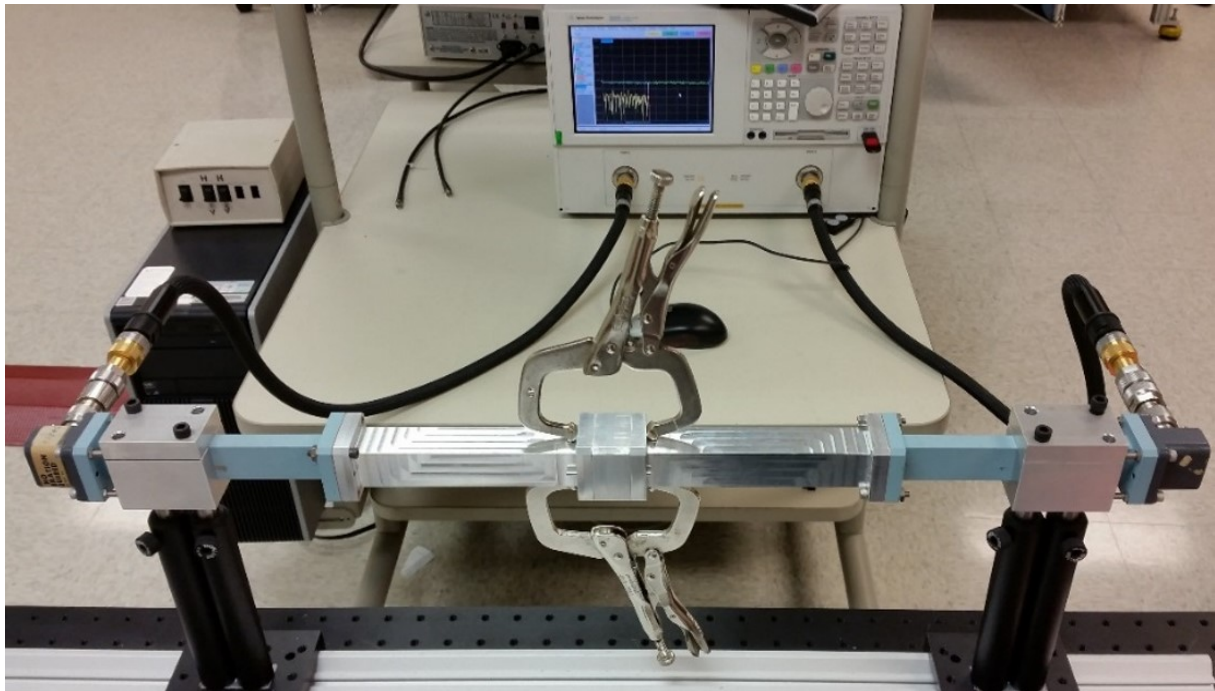


Figure 29. Measurement Setup with Test port cables and Network Analyzer

VNA and the waveguide adapters are torqued to specification with calibrated torque wrenches and waveguide flanges are aligned using precision alignment pins. A TRL calibration is performed prior to measuring the sample as seen in Figure 23. The “Thru” measurement requires that the WRWS waveguide transitions are aligned and measured together. The WRWS “Line” standard is then inserted and aligned between both WRWS transitions and measured. The “Reflect” measurement is taken by inserting a waveguide short between the two waveguide transitions. The sample is then inserted into the sample holder according to an intended measurement orientation, as shown in Figure 13. The sample holder is then inserted and aligned between the WRWS transitions. After the sample is measured in an orientation it is removed from the sample holder and indexed to the next orientation and re-installed in the sample holder. The sample indexing and measuring process is repeated until all orientations have been measured. After the calibration and sample orientation measurements are taken they

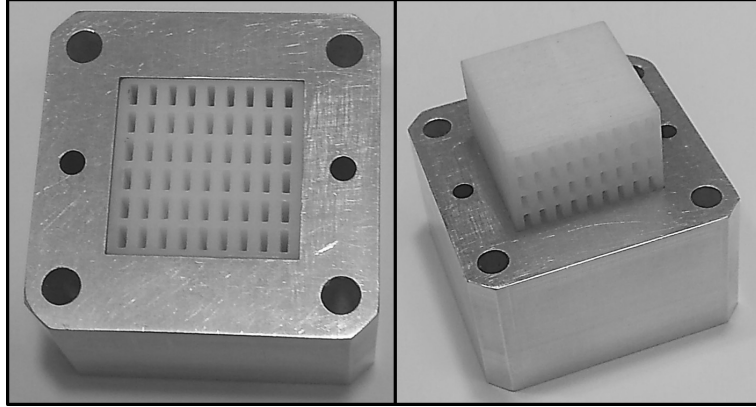


Figure 30. Sample installed in Sample Holder Orientation 1 (Left), Partially installed in Orientation 2 (Right)

are processed in MATLAB[®]. Each sample orientation measurement is calibrated using the measured TRL calibration data and then the relative permittivity is extracted using a 1-D root search.

The extracted permittivity data are plotted together on the same plot to observe how the permittivity orientations pair together in the x, y and z orientations as shown in Figure 33. It is observed that there are pairings in the six measurement orientations. The permittivities in the x, y and z directions are different, which indicate that the sample is electrically biaxial anisotropic.

5.3 CST Model WRWS Model Simulation

A CST Microwave Studio[®] General Purpose Frequency Domain solver model is developed for each sample orientation and calibration measurement, as shown in Figure 31. The Frequency Domain solver is selected because it directly provides S-parameter data. Simulation results yield 1000 data points of two port S-parameter data from 8-13 GHz, which can then be used to extract the sample's permittivity and permeability.

The CST Microwave Studio 2014[®] On-line help [19] provides guidance on which CST simulation functions yield more accurate simulation results. Because the S-

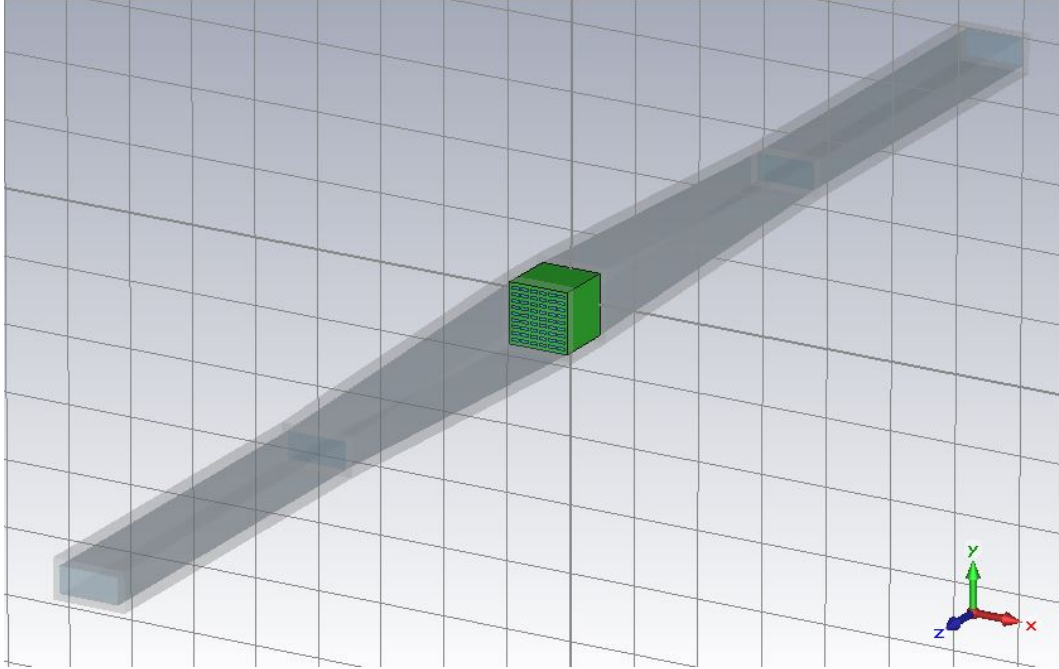


Figure 31. CST Model of WRWS with a green cube denoting sample region

parameter data is used for material parameter extraction calculations, the data needs to be representative of actual results. S-parameter simulation accuracy is attained by controlling the model's tetrahedral mesh and Frequency Domain solver settings.

Controlling the mesh density requires that the “S-Parameter Error Tolerance” (located in the “Adaptive tetrahedral mesh refinement” dialog box) be set to 0.0001. This enables the Frequency domain solver to refine the mesh until the tolerance is achieved. Tightening the error tolerance results in longer simulation times and larger meshes. Selecting the “variable” check box (located in the “Frequency Domain Solver Specials” dialog box) prevents unnecessary over meshing of the model. According to [19], the variable setting allows for non-uniform mesh refinement, which allows fine detail regions (such as the biaxial sample) to be more finely meshed than low detail regions (like the waveguide sections). The mesh size is also further reduced by employing electric and magnetic symmetry planes along the length of the WRWS model. This reduces the number of WRWS model mesh cells by approximately 25%.

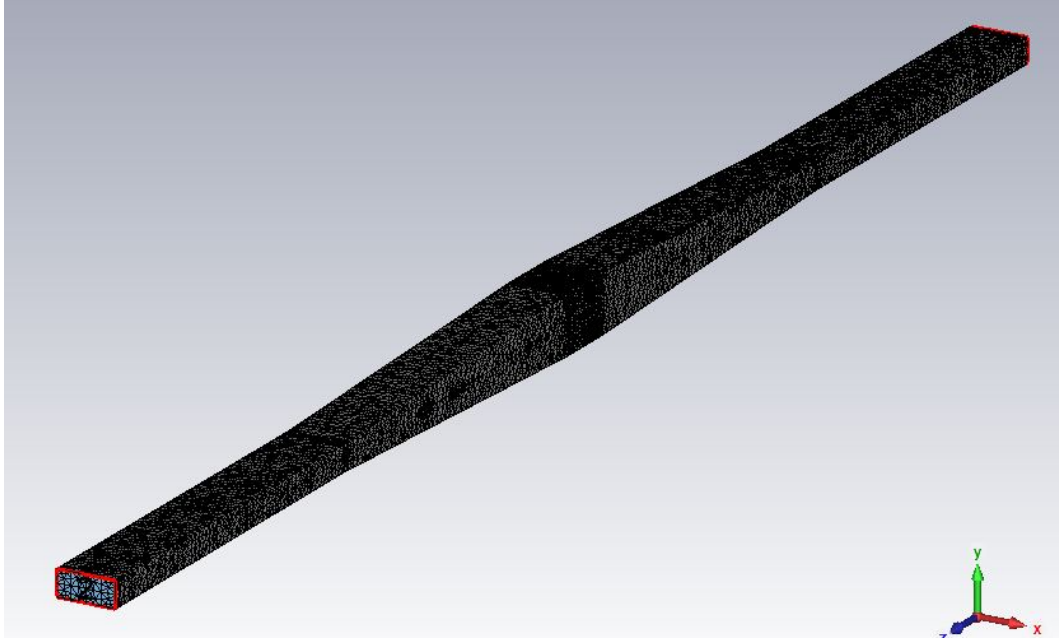


Figure 32. CST WRWS Model in mesh view

Frequency Domain solver setting also indirectly impact meshing by balancing solver accuracy with mesh density. Setting the “Solver Order” to “3rd” can increase the solver accuracy using fewer mesh cells, at the cost of more computer memory [19]. [19] also suggests that a maximum cell size be established when using the higher “Solver Order”. Four cells per wavelength at 13 GHz is selected as an initial maximum cell size and is refined as the solver evaluates the model. Other simulation accuracy improvements are specific to how the solver handles numerical precision and model material composition data. Setting the solver “Accuracy” to “1E-6” gives better solver numerical precision without incurring significantly longer simulation run times. Selecting the “Low Frequency Stabilization” also provides more accurate calculation of the waveguide port modes and better linear equation system solver accuracy [19]. Selecting the “Fit as in Time Domain” better accounts for material loss properties and interpolates model material parameter values between given material parameter data points, which provides better accuracy with lossy or dispersive media [19].

Upon executing a simulation, CST’s “Adaptive tetrahedral mesh refinement” pro-

Table 3. CST Simulation Performance Figures

Simulation	Run Time (hr:min:sec)	Tetrahedral Mesh Cells	Degrees of freedom	Freq. Pts. needed for convergence	Adaptive Mesh Refinement iterations
Thru	0:10:30	27,624	474,490	53	10
Reflect	0:00:20	1,852	10,506	42	1
Line	0:10:20	24,765	423,025	59	9
Sample O-1	1:12:50	102,373	1,543,531	60	23
Sample O-2	1:27:37	99,751	1,542,942	55	19
Sample O-3	0:49:07	60,602	938,241	56	12
Sample O-4	0:49:39	65,255	1,007,366	51	13
Sample O-5	1:13:06	75,494	1,126,896	53	16
Sample O-6	1:09:00	82,414	1,240,252	54	16

cess refines the mesh until successive 13 GHz S-parameter trials converge to the specified “S-Parameter Error Tolerance” of 0.0001. The solver then evaluates the model at different frequencies within the 8-13 GHz band, until the entire band of two port S-parameter measurements converges within the error tolerance. Figure 32 shows a typical WRWS system mesh and Table 3 shows simulation performance data. The simulated S-parameter data is transferred to MATLAB® and each simulated measurement orientation is calibrated from the simulated TRL calibration data. The permittivity of each calibrated orientation is extracted and prediction results are compared to measured data. Excellent agreement is observed between measured and simulated results, as seen in Figures 33 and 34.

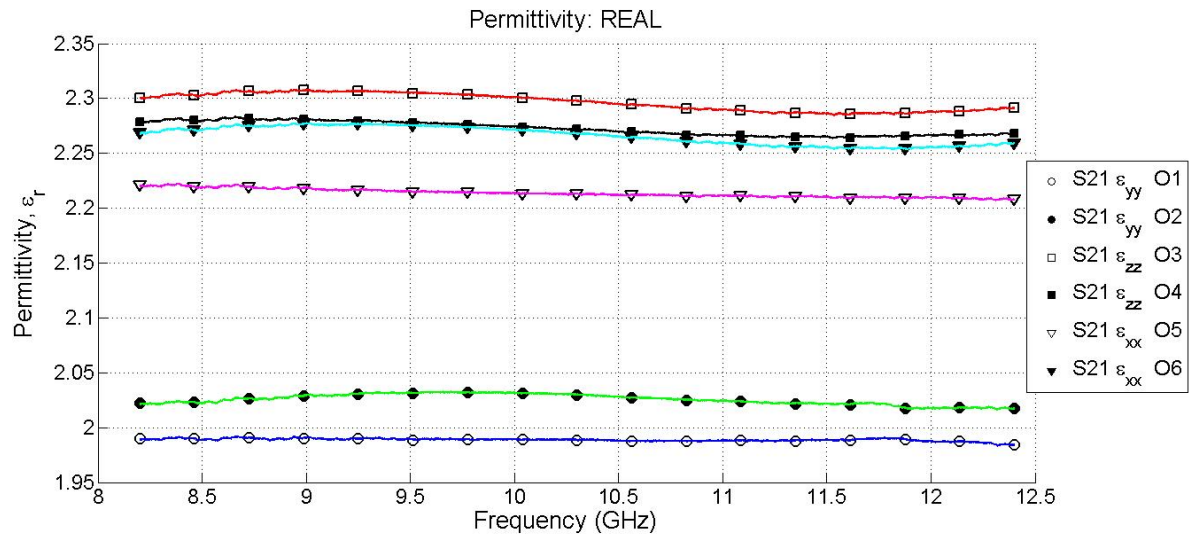


Figure 33. Measured Permittivity from Electrically Biaxial Anisotropic Cube with Air Occlusions arranged in a 9 by 6 array

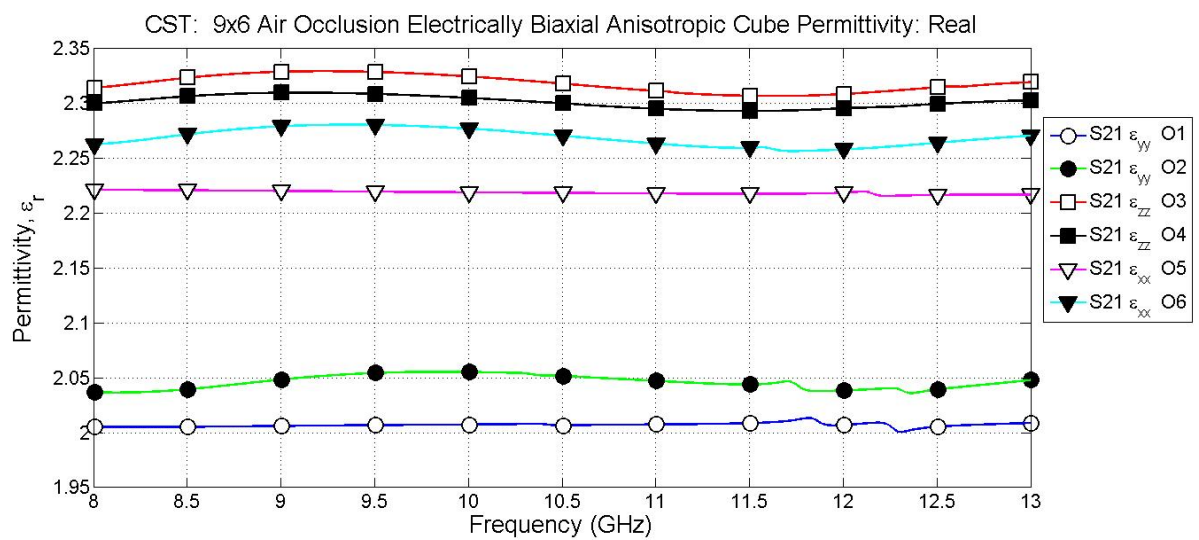


Figure 34. CST Simulated Permittivity from Electrically Biaxial Anisotropic Cube with Air Occlusions arranged in a 9 by 6 array

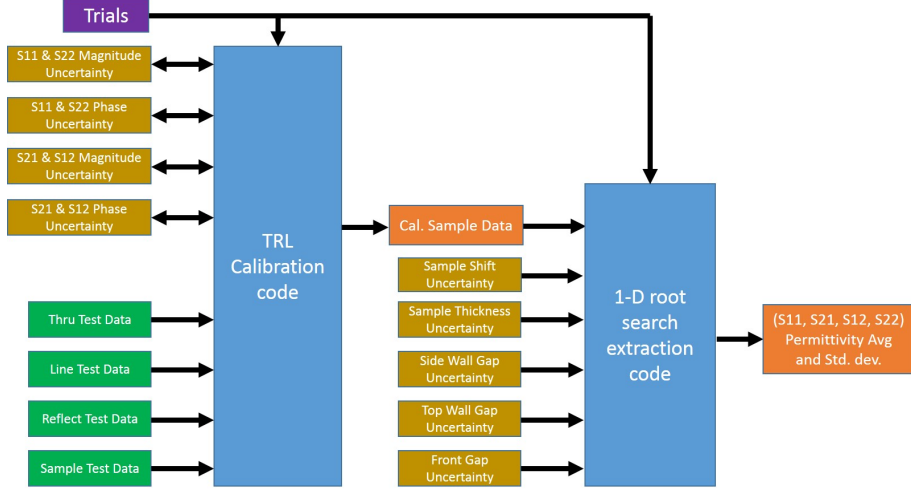


Figure 35. Monte Carlo Uncertainty Analysis Flow Chart: Gold indicates random test variables, Green- Test Data Inputs, Orange- Outputs, Blue- Code. Bi-directional arrows associated with the calibration code indicate a specific uncertainty is obtained given a particular transmission or reflection coefficient.

5.4 Measurement Uncertainty Analysis

A Monte Carlo uncertainty analysis is performed on the WRWS system to observe the effects of random errors on measurement accuracy. Contributing error sources under evaluation include: calibration, sample-waveguide gaps, sample thickness and sample position uncertainty. Gaussian random variables are declared for S-parameter data, while measurable dimension measurements are uniform random variables. Figure 35 is the Monte Carlo Uncertainty Analysis block diagram. Test data is provided to the TRL calibration code, and the magnitude appropriate VNA uncertainties are applied to the Thru, Reflect, Line and Sample data. It is observed in Figure 36 that the reflection and transmission coefficient uncertainties are not constant and change depending on the magnitude of the received signal. Keysight Technologies® maintains a VNA Uncertainty Calculator [23] which is used to determine the S-parameter uncertainties for an Agilent Technologies® E8362B VNA with 63 centimeter test port cables, operating from 8.2-12.4 GHz at 0 dBm power, with an 10 KHz intermediate frequency bandwidth and calibrated using a TRL calibration kit. After the VNA un-

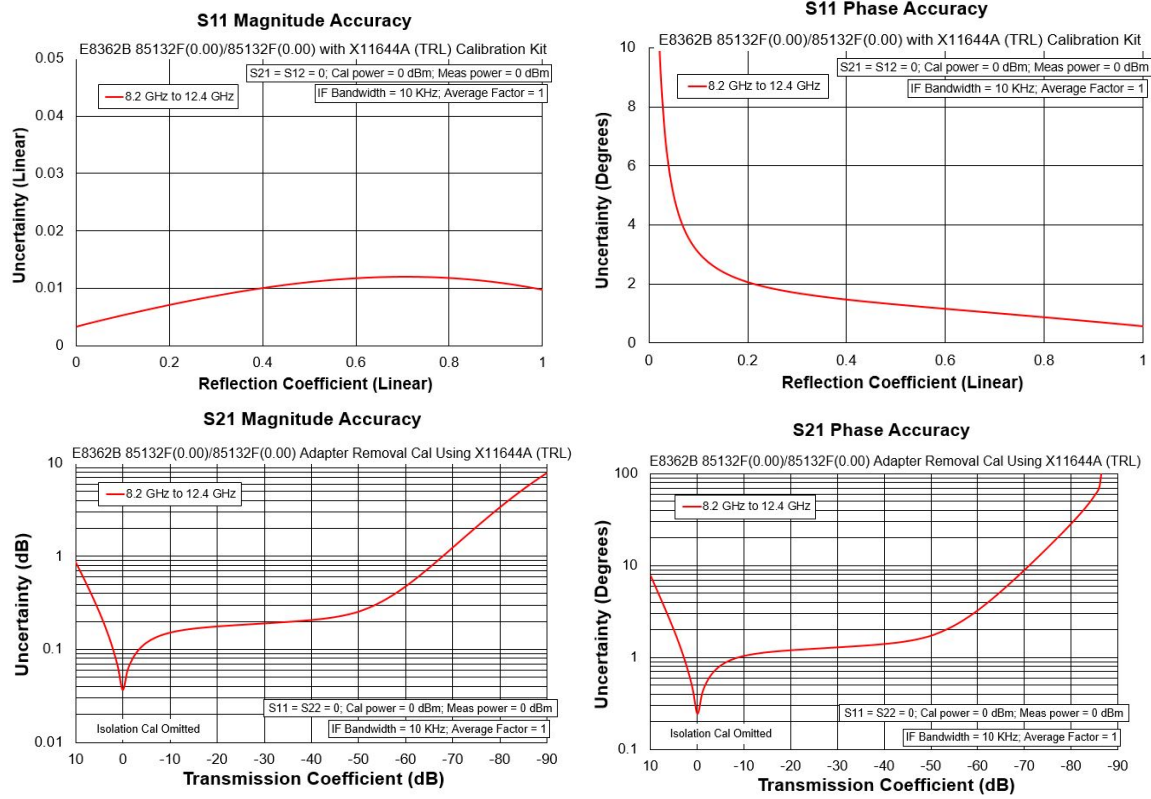


Figure 36. VNA Uncertainty vs Reflection (Top) and Transmission (Bottom) generated for the Agilent Technologies® E8362B VNA from the Keysight Technologies® VNA uncertainty calculator.

certainties are applied and the TRL calibration performed, the permittivity is then extracted from the calibrated sample data using a 1-D root search extraction Monte Carlo analysis, which applies sample thickness, position, and gap uncertainties. Gap uncertainties are accounted as gap corrections to the 1-D root search results. An equivalent capacitance lumped element model corrects the permittivity caused by potential gaps present on three sides of the sample. Gaps are assumed on top, the front and 1 side of the sample, as shown in Figure 37. Uniform random variables are: $g_{y_{RV}}$, a gap in the y direction; $g_{x_{RV}}$, a gap in the x direction; l_{RV} is the gap in sample thickness. l is the sample edge length. The sample's measured permittivity can be

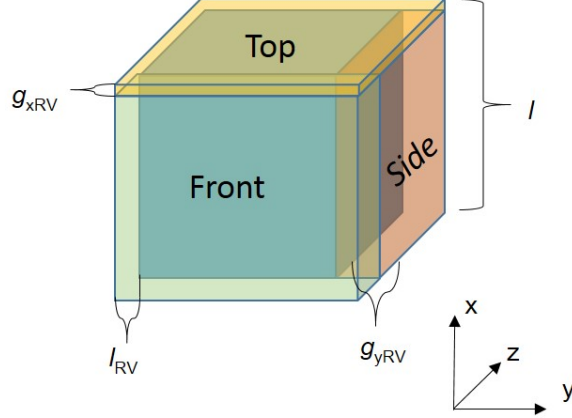


Figure 37. Cubic sample (blue) with colored gaps regions. The colored regions show how gaps are accounted in the Monte Carlo Simulation

re-written as an equivalent capacitance

$$C_{rn} = \frac{\epsilon_0 \epsilon_{rn} l^2}{l}. \quad (5.1)$$

Constructing an equivalent capacitors to model the effects of each gap on the sample yields:

$$C_{side} = \frac{\epsilon_0 g_{yRV} (l - l_{RV})}{l - g_{xRV}} \quad (5.2)$$

$$C_{front} = \frac{\epsilon_0 (l - g_{yRV}) l_{RV}}{l - g_{xRV}} \quad (5.3)$$

$$C_{top} = \frac{\epsilon_0 (l - l_{RV}) (l - g_{yRV})}{g_{xRV}} \quad (5.4)$$

Deducting the capacitance associated with each of the gaps from the total capacitance of (5.1) provides the capacitance of the sample,

$$C_{sample} = -C_{front} - C_{side} - \frac{1}{\frac{1}{C_{top}} - \frac{1}{C_{rn}}}. \quad (5.5)$$

Because the gaps change the sample dimensions they are included in the calculation of the corrected sample permittivity,

$$\epsilon_{rn[corrected]} = \frac{C_{sample} (l - g_{xRV})}{\epsilon_0 (l - l_{RV}) (l - g_{yRV})}. \quad (5.6)$$

The Monte Carlo process assumes that the sample is exactly a cube with an edge length of 22.86 mm. The maximum allowable gap, sample thickness, and sample position is 0.0762 mm, approximately the thickness of a sheet of paper and is chosen because it is the measurable worst case. Experimental observation showed that samples with gaps larger than 0.0762 mm begin to exhibit significant coupling of higher order modes, which manifest in permittivity or permeability results as random and irregularly shaped spikes or scallops. A 0.0762 mm shift in sample position would result in the sample's position being corrected and a change of 0.0762 mm to the sample's thickness results in a sample's discard. Each sample orientation is evaluated independently, requiring the analysis to be performed six times to generate error bars for all test data sets. Multiple Monte Carlo simulations of all six orientations are run with different trial sizes (100 to 100,000) to observe error bar changes. Trials greater than 1000 took significant time and exceeded computer memory, as a result a 1000 trial Monte Carlo analysis provides error bars associated with the experimental data plots. The WRWS system can make permittivity measurements with at most a 2% error as seen in Figure 38.

Overlaying error bars generated from the Monte Carlo uncertainty analysis, and comparing the experimental data and CST prediction methods as seen in Figure 39, it is observed that the CST results agree with experimental results. Comparing the experimental and simulated results with the lumped element prediction also shows agreement. Additionally, the error bars show how unique a measurement orientation is as compared to other measurement orientations of the same sample.

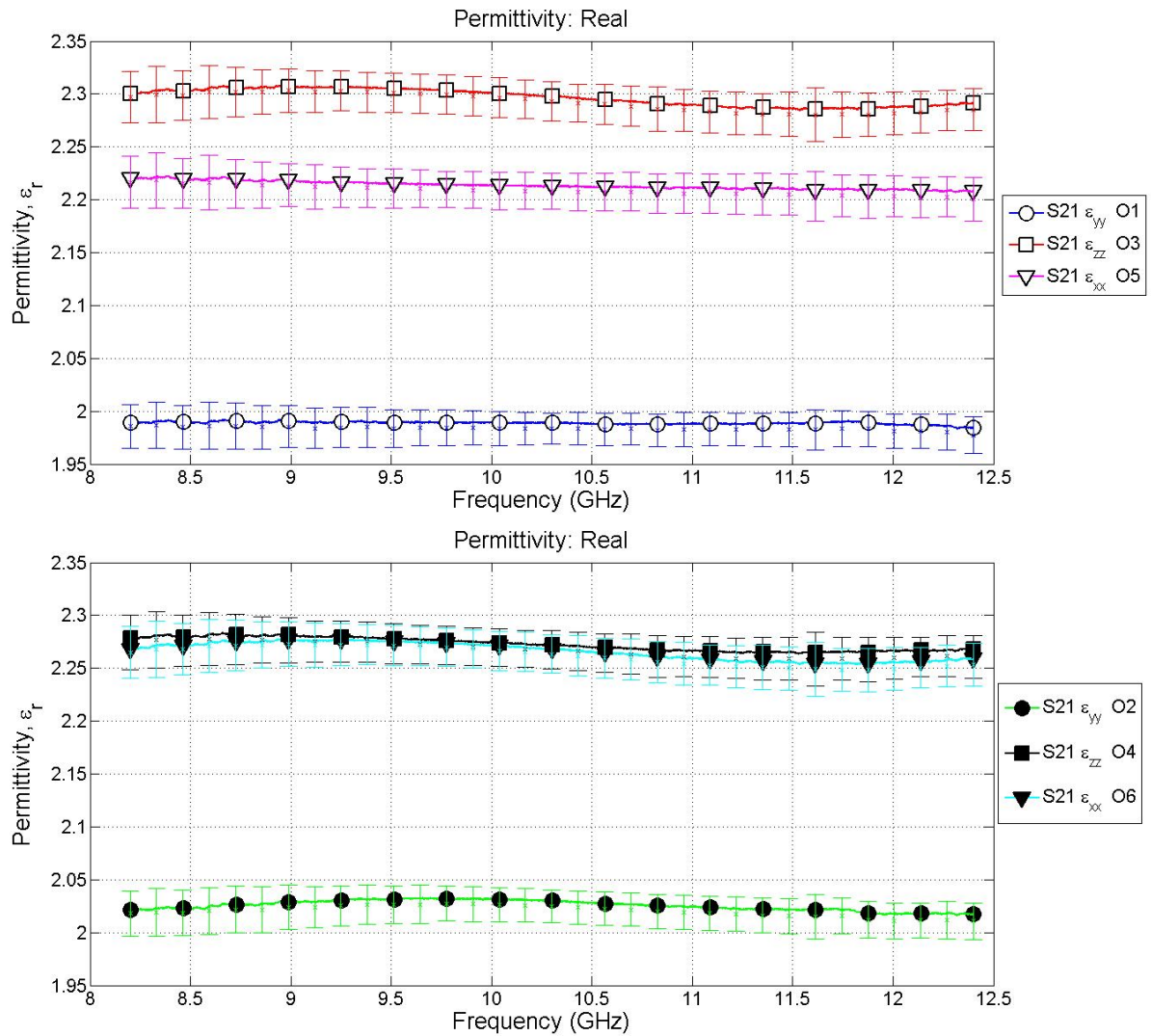


Figure 38. Error Bars Generated from 1000 trial Monte Carlo on Experimental Data, Odd orientations (Top), Even orientations (Bottom)

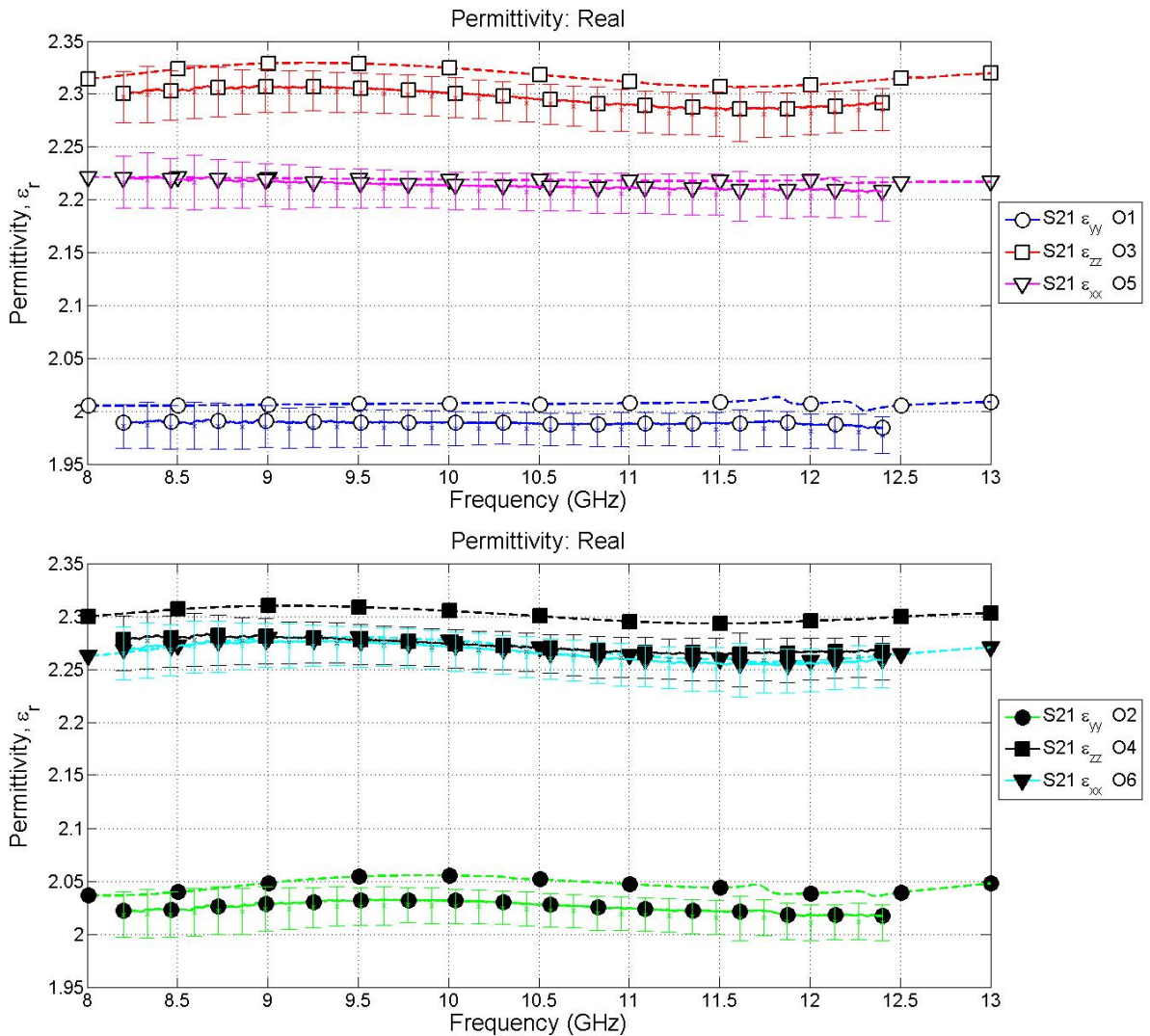


Figure 39. Comparison of Simulation Data with Experimental Uncertainty Data Odd orientations (Top), Even orientations (Bottom)

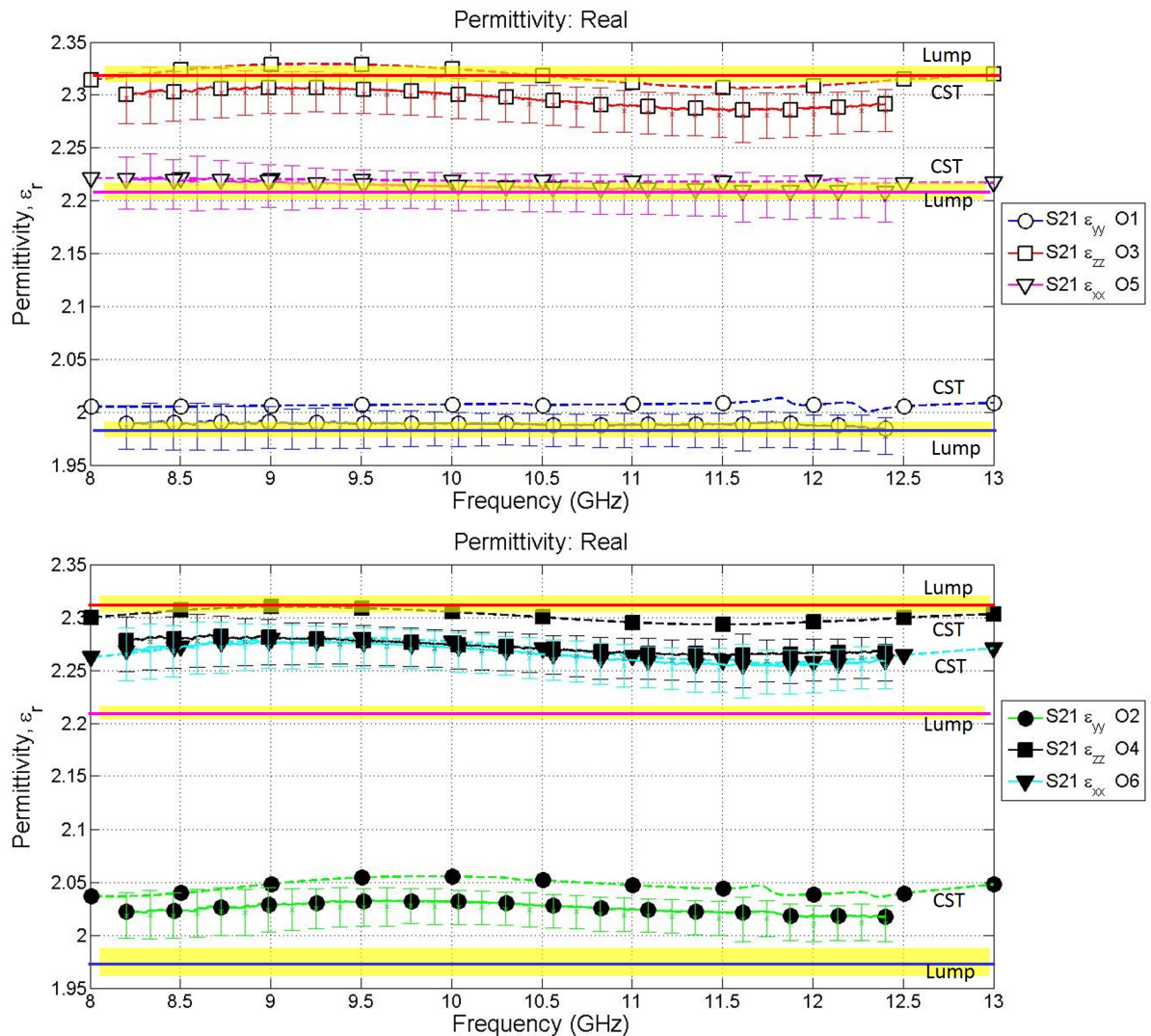


Figure 40. Comparison of Vertical arrangement Lumped Element Data and Simulation Data with Experimental Uncertainty Data Odd orientations (Top), Even orientations (Bottom)

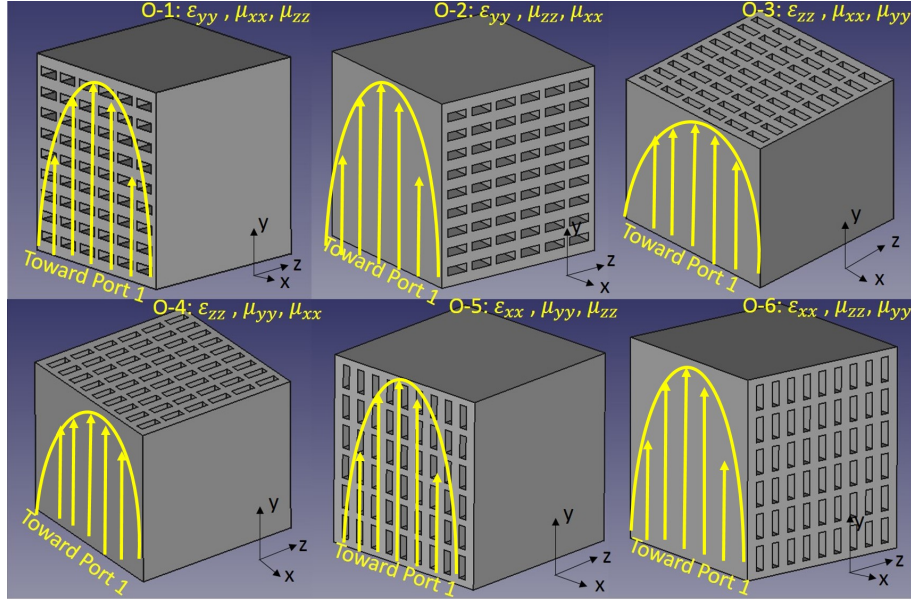


Figure 41. Overlay of sample measurement orientations with TE_{10} mode profile showing potential non-uniform interrogation of sample

5.5 Observations and Discussion

Comparing the performance between the even and odd orientations of Figure 40, the odd orientations, clearly demonstrate electrically biaxial anisotropic performance, while the even orientations show uniaxial performance. Differences in permittivity between equivalent measurement orientations could potentially be caused by the TE_{10} amplitude weighting present in the waveguide. Waveguide measurement techniques assume that a sample is truly homogeneous. The biaxial sample tested, however is not truly homogeneous. Since the sample is interrogated by a cosine weighted amplitude (TE_{10}), uniform phase electric field as seen in Figure 41, the individual cells occlusions and structure contribute differently than if interrogated by a truly uniform plane wave. Particular orientations appear to have more or less structural material contributing to the overall permittivity of the sample. A simulated free-space sample measurement is performed and a 1-D root search free-space material parameter extraction code is developed to provide permittivity results. The free-

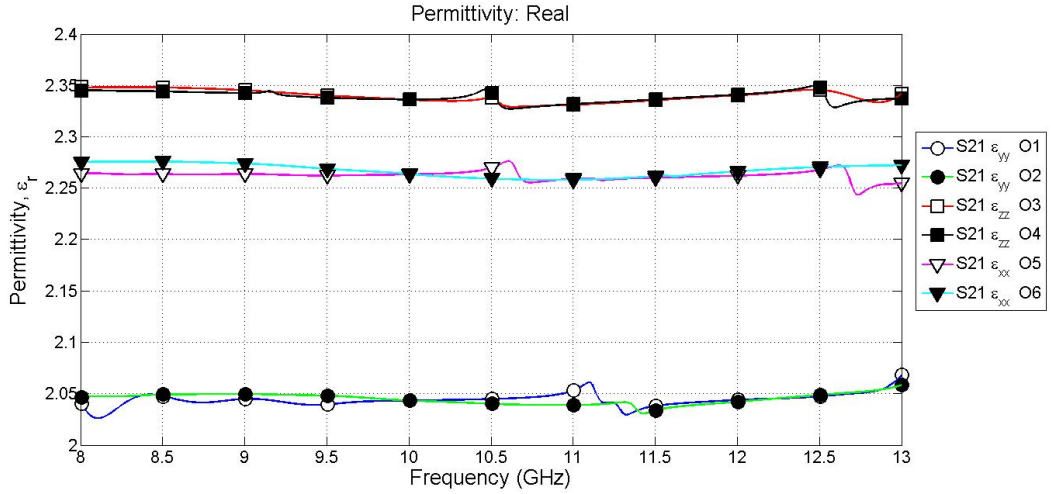


Figure 42. TEM Free Space CST Measure of an infinite array of cubes arranged in a slab

space CST material measurement modeling concept is based on [24]’s approach. TRL calibrated and extracted results from the CST model are shown in Figure 42 which assumes uniform plane wave interrogation of an infinite slab made of the sample cubes, as shown in Figure 43. Changing the interrogating field amplitude from a cosine weighting (WRWS) to a uniform weighting (free-space) causes the x, y, z paired permittivity orientation to be almost equivalent. Another contributing factor to equivalent orientations yielding slightly different values could be caused by the occlusion array not being printed perfectly symmetric and centered within the sample. The occlusion array being biased would cause more or less material to appear present depending on the sample’s orientation within the waveguide.

5.6 Electrically Biaxial Anisotropic Samples using different materials

Despite the weighting effect, biaxial anisotropic performance is more easily observed by increasing the permittivity contrast between structure and inclusion materials. A sample simulated in CST Microwave Studio® with the same UV cured polymer structure and alumina inclusions, instead of air occlusion enhances the sep-

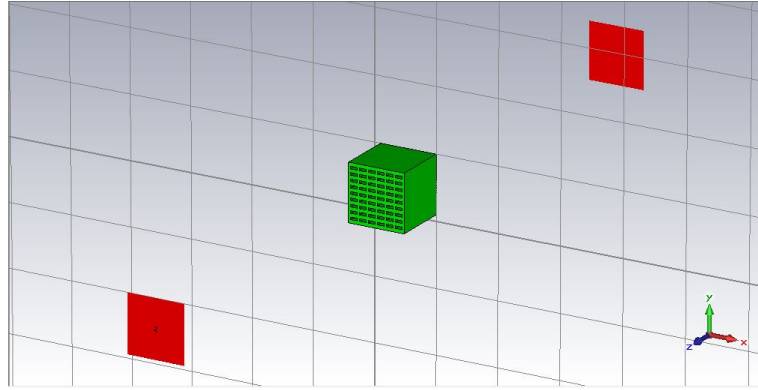


Figure 43. Plane Wave Excitation Model on an infinite array of cubes

ration between the permittivity in x, y and z directions. Comparing the air occlusion

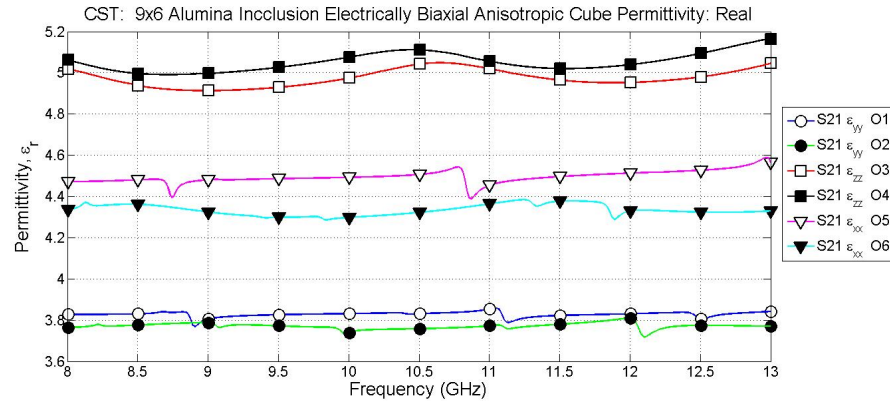


Figure 44. Electrically Biaxial Alumina Inclusion Loaded Sample simulated in CST Microwave Studio

results of Figure 34 and the alumina inclusions results of Figure 44, it is also demonstrated that the same crystallographic design can be used to make a biaxial anisotropic structure independent of the materials employed.

5.7 Summary

The results demonstrate the WRWS system's ability to successfully measure a biaxial anisotropic sample. Measured results agree with the simulation and lumped element predictions. The Monte Carlo uncertainty analysis demonstrates the system measurement error and how well each of the measurement orientations contrast.

VI. Conclusion

A new waveguide anisotropic material measurement capability has been demonstrated. The WRWS measurement system combines the best features of previous measurement systems, including utilization of closed form analytic solutions for material parameter extraction and requiring only 1 cubic sample. Theoretical developments have been provided to show how a biaxial anisotropic material effects fields and how it is measured, both in free space and in a waveguide. Performance has been verified through experimental measurement, CEM simulation and lumped element prediction. A biaxial anisotropic material structure is synthesized using crystallographic symmetry and printed on an additive UV cured 3-D polymer printer. An uncertainty analysis is provided to demonstrate the measurement error and observations are made about the sample's permittivity tensors elements given a particular field application or material selection.

6.1 Future Work

The WRWS measurement system has several areas for future work. Since WRWS samples are electrically thick, resonance issues make it impossible to evaluate low loss material samples that have both permittivity and permeability tensor elements. A potential avenue of exploration could be to employ a two sample measurement method. An extended sample holder could be made to accommodate two cubic samples, that could be indexed into the different measurement orientations. Two sets of transmission measurements would be made: the first: of just one cube sample, the second: both cube samples. A “2 samples of different lengths” material parameter extraction method [25] for biaxial anisotropic material could then be utilized, and would avoid the resonance issue. The assumption is that the 3-D printed sam-

ple production is sufficiently consistent. This technique would be equally or more advantageous as compared to previous techniques because the sample can still be indexed and only requires 2 samples, as opposed to the 3 unique samples required for rectangular waveguide techniques.

Another area of research, is to explore magnetic samples in a crystallographic design. A magnetically biaxial sample could be designed using small ferrous inclusions, such as Nickel. Provided the structural material possesses the same dielectric contrast as the magnetic material, a 1-D root search could be made for a sample's permeability, assuming the permittivity is known. If the 2 sample technique is successfully utilized then materials that exhibit both electric and magnetic biaxial performance could be studied within the same sample.

A final research area, would be to utilize free-space measurement techniques, such as a focus beam system and measure the biaxial anisotropic performance of an array of cubics samples arranged in a sheet. The cubic samples could be indexed through their measurement orientations within the sheet structure, which would allow for all six measurement orientations to be measured at normal incidence. Additionally, the free-space mathematical development of Chapter 2 could be utilized to support sample measurements at oblique incidence. The difficulty in the oblique evaluation is the additional antennas needed to measure both polarizations for both transmitted and reflected field components.

Bibliography

1. A. Nicolson and G. F. Ross, "Measurement of the intrinsic properties of materials by time-domain techniques," *IEEE Transactions on Instrumentation and Measurement*, vol. 19, no. 4, pp. 377–382, 1970.
2. W. B. Weir, "Automatic measurement of complex dielectric constant and permeability at microwave frequencies," *Proceedings of the IEEE*, vol. 62, no. 1, pp. 33–36, 1974.
3. T. Blakney and W. Weir, "Comments on "automatic measurement of complex dielectric constant and permeability at microwave frequencies"," *Proceedings of the IEEE*, vol. 63, no. 1, pp. 203–205, Jan 1975.
4. J. Baker-Jarvis, E. Vanzura, and W. Kissick, "Improved technique for determining complex permittivity with the transmission/reflection method," *IEEE Transactions on Microwave Theory and Techniques*, vol. 38, no. 8, pp. 1096–1103, 1990.
5. N. Damaskos, R. Mack, A. Maffett, W. Parmon, and P. L. E. Uslenghi, "The inverse problem for biaxial materials," *IEEE Transactions on Microwave Theory and Techniques*, vol. 32, no. 4, pp. 400–405, 1984.
6. B. Crowgey, O. Tuncer, J. Tang, E. Rothwell, B. Shanker, L. Kempel, and M. Havrilla, "Characterization of biaxial anisotropic material using a reduced aperture waveguide," *IEEE Transactions on Instrumentation and Measurement*, vol. 62, no. 10, pp. 2739–2750, Oct 2013.
7. J. Tang, B. Crowgey, O. Tuncer, L. Kempel, E. Rothwell, and B. Shanker, "Characterization of biaxial materials using a partially filled rectangular waveguide," in *34th Annual Symposium of the Antenna Measurement Techniques Association Conference Proceeding*, October 2012, pp. 437–442.
8. A. Knisely, M. Havrilla, P. Collins, M. Hyde, J. Allen, A. Bogle, and E. Rothwell, "Biaxial anisotropic material characterization using rectangular to square waveguide," in *36th Annual Symposium of the Antenna Measurement Techniques Association Conference Proceedings*, October 2014, pp. 437–442.
9. R. Collin, "A simple artificial anisotropic dielectric medium," *IRE Transactions on Microwave Theory and Techniques*, vol. 6, no. 2, pp. 206–209, 1958.
10. V. Dmitriev, "Tables of the second rank constitutive tensors for linear homogeneous media described by the point magnetic groups of symmetry," *Progress In Electromagnetics Research*, vol. 28, pp. 43–95, 2000.
11. C. Balanis, *Advanced Engineering Electromagnetics*, ser. CourseSmart Series. Wiley, 2012.

12. A. Knisely and M. J. Havrilla, "Material characterization de-embedding for rectangular to square waveguide," in *The 9th European Conference on Antennas and Propagation (EuCAP 2015) (EuCAP 2015)*, Lisbon, Portugal, Apr. 2015.
13. D. Pozar, *Microwave Engineering*. Wiley, 2004.
14. M. Havrilla, M. Hyde and A. Bogle, "Improved bandwidth in rectangular waveguide material characterization measurements," in *36th Annual Symposium of the Antenna Measurement Techniques Association Conference Proceedings*, October 2014, pp. 427–431.
15. T. Hahn, *International Tables for Crystallography-Volume A: "Space-Group Symmetry"*. Springer, 2005.
16. A. Authier, *International Tables for Crystallography-Volume D: "Physical Properties of Crystals"*. Kluwer Academic Publishers, 2003.
17. S. Patil, M. Koledintseva, R. Schwartz, and W. Huebner, "Prediction of effective permittivity of diphasic dielectrics using an equivalent capacitance model," *Journal of Applied Physics*, vol. 104, no. 7, pp. 074 108–074 108–11, Oct 2008.
18. W. Hayt and J. Buck, *Engineering Electromagnetics*, ser. Electrical engineering series. McGraw-Hill Education, 2001.
19. "Cst microwave studio suite online help," *CST Microwave Studio 2014*. [Online]. Available: <https://www.cst.com/>
20. G. F. Engen and C. A. Hoer, "Thru-reflect-line: An improved technique for calibrating the dual six-port automatic network analyzer," *IEEE Transactions on Microwave Theory and Techniques*, vol. 27, no. 12, pp. 987–993, Dec 1979.
21. D. Rytting, "An analysis of vector measurement accuracy enhancement techniques," *RF and Microwave Symposium and Exhibition, Hewlett Packard*, March 1982.
22. ——, "Appendix to an analysis of vector measurement accuracy enhancement techniques," *RF and Microwave Symposium and Exhibition, Hewlett Packard*, March 1982.
23. "Downloadable vector network analyzer uncertainty calculator," *Keysight Technologies Software*. [Online]. Available: <http://www.keysight.com/main/home.jspx?cc=US&lc=eng>
24. D. Schurig, "Assignments," *ECE 5350/6350 Fall 2013 Metamaterials and Advanced Antenna Theory*. [Online]. Available: http://www.ece.utah.edu/~dschurig/5/ECE_5350_and_6350_Fall_2013/Assignments.html

25. J. Baker-Jarvis, M. Janezic, J. Grosvenor, and R. Geyer, "Transmission/reflection and short-circuit line methods for measuring permittivity and permeability," *Natl. Inst. Stand. Technol. Tech. Note 1355-R*, p. 20, 1993.

REPORT DOCUMENTATION PAGE

Form Approved
OMB No. 0704-0188

The public reporting burden for this collection of information is estimated to average 1 hour per response, including the time for reviewing instructions, searching existing data sources, gathering and maintaining the data needed, and completing and reviewing the collection of information. Send comments regarding this burden estimate or any other aspect of this collection of information, including suggestions for reducing this burden to Department of Defense, Washington Headquarters Services, Directorate for Information Operations and Reports (0704-0188), 1215 Jefferson Davis Highway, Suite 1204, Arlington, VA 22202-4302. Respondents should be aware that notwithstanding any other provision of law, no person shall be subject to any penalty for failing to comply with a collection of information if it does not display a currently valid OMB control number. **PLEASE DO NOT RETURN YOUR FORM TO THE ABOVE ADDRESS.**

1. REPORT DATE (DD-MM-YYYY) 26-03-2015	2. REPORT TYPE Master's Thesis	3. DATES COVERED (From — To) Sept 2013 — Mar 2015		
4. TITLE AND SUBTITLE Biaxial Anisotropic Material Development and Characterization using Rectangular to Square Waveguide		5a. CONTRACT NUMBER 5b. GRANT NUMBER 5c. PROGRAM ELEMENT NUMBER		
6. AUTHOR(S) Knisely, Alexander G., Mr., Civ.		5d. PROJECT NUMBER 5e. TASK NUMBER 5f. WORK UNIT NUMBER		
7. PERFORMING ORGANIZATION NAME(S) AND ADDRESS(ES) Air Force Institute of Technology Graduate School of Engineering and Management (AFIT/EN) 2950 Hobson Way WPAFB OH 45433-7765		8. PERFORMING ORGANIZATION REPORT NUMBER AFIT-ENG-MS-15-M-055		
9. SPONSORING / MONITORING AGENCY NAME(S) AND ADDRESS(ES) Air Force Research Laboratory, Sensors Directorate Attn: Garrett J. Stenholm 2591 K Street, Bldg 254 WPAFB OH 45433-7602 DSN 785-9179, COMM 937-255-9179 Email: Garrett.Stenholm@us.af.mil		10. SPONSOR/MONITOR'S ACRONYM(S) AFRL/RYS		
		11. SPONSOR/MONITOR'S REPORT NUMBER(S)		
12. DISTRIBUTION / AVAILABILITY STATEMENT DISTRIBUTION STATEMENT A: APPROVED FOR PUBLIC RELEASE; DISTRIBUTION UNLIMITED.				
13. SUPPLEMENTARY NOTES This material is declared a work of the U.S. Government and is not subject to copyright protection in the United States.				
14. ABSTRACT The advent of 3-D printing provides a new way to develop complex electromagnetic media. Complex media poses measurement challenges and require new techniques to characterize sample constitutive parameters. A biaxial anisotropic sample is designed using crystallographic symmetry and tensor elements are predicted using equivalent capacitive and inductive lumped elements. Samples are measured using the Waveguide Rectangular to Waveguide Square (WRWS) cubic sample measurement system. The WRWS system supports the analysis of a cubic biaxial anisotropic sample by measuring the sample in different measurement orientations. The orientation S-parameter data is used to extract tensor element permittivities and permeabilities using an analytic, closed-form technique. Research performed in this document demonstrates a sample synthesis methodology, a measurement representative computational electromagnetic (CEM) prediction of WRWS sample measurements and tests results of an electrically biaxial sample. An uncertainty analysis is also conducted on the experimental data to evaluate potential error sources. The lumped element and CEM predictions agree with the test results. Supplemental discussion also provides a comparison between test data and a free-space simulated results as well as simulated example of an electrically biaxial sample loaded with alumina. These two examples demonstrate the utility of a crystallographic sample design.				
15. SUBJECT TERMS RF Material Characterization, Anisotropic, Biaxial, Electromagnetics, Tapered Waveguide, Metamaterials				
16. SECURITY CLASSIFICATION OF:		17. LIMITATION OF ABSTRACT	18. NUMBER OF PAGES	19a. NAME OF RESPONSIBLE PERSON Dr. Michael J. Havrilla, AFIT/ENG
a. REPORT U	b. ABSTRACT U	c. THIS PAGE U	UU	19b. TELEPHONE NUMBER (include area code) (937) 255-3636, x4582 michael.havrilla@afit.edu
104				